R-1399
CU- 374
NEVIS- 268

Nevis Laboratories
Columbia University
Physics Department
Irvington-on-Hudson
New York

ν_μ-ν_e Universality in Charged-Current Neutrino Interactions

Steven Laurens Manly

Reproduction in whole or in part
is permitted for any purpose of the
United States Government

Submitted in partial fulfillment of
the requirements for the degree
of Doctor of Philosophy in the
Graduate School of Arts and Sciences
Columbia University

1988

National Science Foundation

ν_μ-ν_e Universality in Charged-Current Neutrino Interactions

Steven Laurens Manly

Physics Department
Columbia University, New York, NY 10027

This research was supported in part by the National Science Foundation.

Submitted in partial fulfillment of the requirements for the degree of Doctor of Philosophy in the Graduate School of Arts and Sciences, Columbia University.

ABSTRACT

Approximately 2000 ν_e and $\bar{\nu}_e$ charged-current interactions with energies ranging up to 200 GeV were observed in a wide band neutrino beam using the Fermilab 15-ft bubble chamber filled with a heavy Ne-H_2 mix. The cross section, kinematic distributions, charged particle multiplicity, strange particle production, and dilepton production for these events are compared to those for samples of ν_μ and $\bar{\nu}_\mu$ charged-current events obtained during the same experiment.

TABLE OF CONTENTS

	Page
Chapter 1: Introduction	1
1.1 Review of Universality in the Standard Model	3
1.2 Theoretical Possibilities	12
1.3 Experimental Status of Universality	17
Chapter 2: Data Acquisition and Reduction	29
2.1 The Neutrino Beam	29
2.2 The Bubble Chamber	31
2.3 Scanning and Measuring	33
2.4 Event Reconstruction	37
2.5 Data Reduction	40
Chapter 3: Analysis and Results	44
3.1 Electron Neutrino and Antineutrino Samples	44
3.1.1 Backgrounds	45
3.1.2 Corrections	48
3.2 Muon Neutrino and Antineutrino Samples	51
3.2.1 Event Selection	52
3.2.2 Backgrounds	53
3.2.3 Corrections	57
3.3 Results	58

3.3.1 Cross Sections 58

3.3.2 Kinematic Distributions 62

3.3.3 Neutral Strange Particle Rates 67

3.3.4 Charged Particle Multiplicities 69

3.3.5 ν_e-Induced Charm (Dileptons) 69

3.4 Conclusion 72

Appendix A: Beam Monte Carlo..... 73

Appendix B: Electron Momentum Reconstruction..... 77

Appendix C: Kinematics..... 86

References 87

Acknowledgements 94

List of Tables 98

Tables 99

List of Figures 104

Figures 109

CHAPTER 1: INTRODUCTION

The standard model of particle physics brings some order and understanding to the menagerie of subnuclear particles discovered since the turn of the century. Many aspects of the standard model have been confirmed experimentally; however, there are various reasons to believe it is incomplete and not fully tested. As with all successful scientific theories, the standard model should be viewed as a stepping stone to a deeper understanding.

This thesis is a presentation of a series of measurements which, taken together, represent a significant test of the assumption of universality in the standard model. This assumption allows the extension of this model from a relatively simple theory encompassing only a few particles to one which covers the gamut of known particles.

The concept of universality is worthy of experimental scrutiny outside the context of a model. Observation of a breakdown in universality would herald the existence of new physics; and confirmations(of universality provide important constraints for the large number of theories postulating extensions of the standard model.

The data for this thesis consists of approximately 2000 ν_e and $\bar{\nu}_e$-induced charged-current events and 6000 ν_μ and $\bar{\nu}_\mu$-induced charged-current events observed in the 15-ft bubble chamber at Fermilab in Batavia, Illinois. The energy spectra for these events peak at 20-40 GeV and extend to 200 GeV. In this thesis, the cross sections, kinematic distributions, charged particle multiplicities, and rates for strange particle and dilepton production for the $\nu_e(\bar{\nu}_e)$-induced events are examined and compared to those for the $\nu_\mu(\bar{\nu}_\mu)$-induced events. These comparisons represent a test of ν_μ-ν_e universality in the charged-current weak interaction.

In the first chapter of this thesis a simple version of the standard model is presented and the concept of universality within that model is examined. Next, a number of theoretical models predicting violations of universality are discussed. Finally, the current status of experimental results concerning universality is reviewed. The second chapter is a discussion of the experiment in which the experimental apparatus and preparation of the data for the final analysis are described. In the final chapter details and conclusions of the analysis are presented.

1.1 Review of Universality in the Standard Model

The term 'standard model' is often used in reference to the $SU(3)_{color} \times SU(2)_L \times U(1)_Y$ gauge theory of the strong, weak, and electromagnetic interactions. Here the use of the term is limited to the $SU(2)_L \times U(1)_Y$ portion. This theory establishes the unity of the electromagnetic and weak interactions and has had remarkable success in explaining experimental observations. This model has evolved over the last thirty years from the contributions of many physicists.[1] Most notable are those of S.L. Glashow, S. Weinberg and A. Salam. Thus, this theory is often called the Glashow-Weinberg-Salam or just Weinberg-Salam model.

The purely leptonic standard model[2] is constructed from a left-handed weak-isospin doublet,

$$L \equiv \begin{pmatrix} \nu \\ e \end{pmatrix}_L, \quad \text{where } \nu_L = \tfrac{1}{2}(1-\gamma_5)\nu \text{ and } e_L = \tfrac{1}{2}(1-\gamma_5)e \ ,$$

and a right-handed weak-isospin singlet (assuming the neutrino is massless),

$$R \equiv e_R, \quad \text{where } e_R = \tfrac{1}{2}(1+\gamma_5)e \ .$$

Electromagnetism is incorporated into the theory by using the weak hypercharge, Y, and the weak-isospin, I, where

$$Q = I_3 + \frac{1}{2}Y \ .$$

Y generates the $U(1)_Y$ group and I generates the $SU(2)_L$ group. Now assume the product group $SU(2)_L \times U(1)_Y$ to be a symmetry group for a gauge theory. Introducing the gauge bosons $b^1{}_\mu$, $b^2{}_\mu$, and $b^3{}_\mu$ for $SU(2)_L$ and A_μ for $U(1)_Y$, take

$$F^l_{\mu\nu} = \partial_\nu b^l_\mu - \partial_\mu b^l_\nu + g\epsilon_{jkl} b^j_\mu b^k_\nu$$

and

$$f_{\mu\nu} = \partial_\nu A_\mu - \partial_\mu A_\nu$$

to be the field strength tensors. The Lagrangian density (just termed Lagrangian from this point forward) for this theory is

$$L = -\frac{1}{4}F^l_{\mu\nu}F^{l\mu\nu} - \frac{1}{4}f_{\mu\nu}f^{\mu\nu} + \bar{R}i\gamma^\mu(\partial_\mu + i\frac{g'}{2}A_\mu Y)R$$
$$+ \bar{L}i\gamma^\mu(\partial_\mu + i\frac{g'}{2}A_\mu Y + i\frac{g}{2}\mathbf{T}\cdot\mathbf{b}_\mu)L \ ,$$

where g is the coupling constant for $SU(2)_L$ and g′ is the coupling constant for $U(1)_Y$. The first two terms of the Lagrangian contain the kinetic energies and self-interaction energies for the gauge fields. The second two terms contain the lepton kinetic energies and their interactions with the gauge fields. This Lagrangian has four massless gauge bosons and global SU(2) invariance prohibits the addition of a mass term for the electron.

It is necessary to use the technique of spontaneous symmetry breaking to bring this theory into closer agreement with observation. A complex doublet of scalar fields, called the Higgs field(s), is incorporated into the theory to do this. This doublet,

$$\phi \equiv \begin{pmatrix} \phi^+ \\ \phi^o \end{pmatrix},$$

transforms with $SU(2)_L$ gauge symmetry and has a weak-hypercharge, $Y_\phi = +1$. The Lagrangian must be modified by adding kinetic and potential energy terms for ϕ as well as a Yukawa term describing the interaction between ϕ and the fermions. These terms take the following form:

$$\text{Energy Terms} \equiv \left|(i\partial_\mu - \frac{g'}{2}A_\mu Y - \frac{g}{2}\mathbf{T}\cdot\mathbf{b}_\mu)\phi\right|^2 - \frac{1}{2}\mu^2|\phi|^2 + \frac{1}{4}\lambda|\phi|^4$$

$$\text{Yukawa Term} \equiv -G_e[R(\phi\ L)+(L\phi)R] \ .$$

For $\mu^2 < 0$ and $\lambda > 0$, the minimum of the potential is at

$$\phi = \pm\sqrt{-\frac{\mu^2}{2\lambda}} \ .$$

If the vacuum expectation value of the scalar field is chosen to be

$$\langle\phi\rangle_o = \begin{pmatrix} 0 \\ \frac{v}{\sqrt{2}} \end{pmatrix} \qquad \text{where } v = \sqrt{-\frac{\mu^2}{\lambda}} \ ,$$

the $SU(2)_L \times U(1)_Y$ symmetry of the theory is broken. It is now invariant under the $U(1)_{em}$ gauge symmetry, i.e.,

$$Q\langle\phi\rangle_o = (I_3+\tfrac{1}{2}Y)\langle\phi\rangle_o = 0 \ .$$

The next step is to redefine ϕ by looking at small fluctuations about the vacuum,

$$\phi = e^{i\theta(x)\cdot\tau/2v}\begin{bmatrix} 0 \\ \frac{(v+\eta(x))}{\sqrt{2}} \end{bmatrix} \ .$$

Exploiting the local SU(2) gauge invariance of the theory by working in the Unitary gauge, the variables become

$$\phi(x) \to \phi'(x) = e^{-i\theta(x)\cdot\tau/2v}\phi(x) = \begin{bmatrix} 0 \\ \frac{(v+\eta(x))}{\sqrt{2}} \end{bmatrix}$$

$$A_\mu \to A_\mu$$

$$R \to R$$

$$L \to L' = e^{-i\theta\cdot\tau/2v}L \ .$$

Now, dropping the primes for notational convenience and examining various terms in the Lagrangian after substituting for ϕ and λ, the Yukawa term becomes

$$-G_e[\bar{R}(\phi^+L)+(\bar{L}\phi)R] = -G_e\frac{(v+\eta)}{\sqrt{2}}[\bar{R}L+\bar{L}R] = -\frac{G_e}{\sqrt{2}}(v\bar{e}e+\eta\bar{e}e) \ .$$

The first term gives the mass for the electron. G_e is an arbitrary constant that sets the electron mass. The second term gives the electron-Higgs coupling.

The first scalar term in the Lagrangian,

$$\left|(i\partial_\mu - \frac{g'}{2}A_\mu Y - \frac{g}{2}\mathbf{T}\cdot\mathbf{b}_\mu)\phi\right|^2 ,$$

becomes

$$\left| \partial_\mu \begin{pmatrix} 0 \\ \frac{(v+\eta(x))}{\sqrt{2}} \end{pmatrix} + i\frac{g'}{2}A_\mu Y \begin{pmatrix} 0 \\ \frac{(v+\eta(x))}{\sqrt{2}} \end{pmatrix} + i\frac{g}{2}\begin{pmatrix} (b_1 - ib_2)\frac{(v+\eta)}{\sqrt{2}} \\ -b_3\frac{(v+\eta)}{\sqrt{2}} \end{pmatrix} \right|^2$$

$$= \frac{1}{2}\partial^\mu\eta\partial_\mu\eta + \frac{v^2}{8}[g^2|b^1_\mu - ib^2_\mu|^2 + (g'A_\mu - gb^3_\mu)^2] + \ldots \text{ interaction terms.}$$

The other scalar terms,

$$-\frac{1}{2}\mu^2|\phi|^2 - \frac{1}{4}\lambda|\phi|^4 = -\mu^2[\eta^2 - \frac{1}{4}v^2 + \frac{\eta^4}{4v^2} + \frac{\eta^3}{v}] ,$$

become (for small oscillations about the vacuum),

$$-\eta^2\mu^2 + \text{irrelevant constants.}$$

The η field has mass $-2\mu^2$ and is interpreted as the physical Higgs boson. Defining

$$W^{\pm}_\mu = \frac{b^1_\mu \mp ib^2_\mu}{\sqrt{2}} ,$$

the term proportional to g^2v^2 becomes

$$\frac{g^2v^2}{8}(|W_\mu^+|^2+|W_\mu^-|^2) \ .$$

These are the mass terms for the charged vector bosons. The remaining scalar term,

$$\frac{v^2}{8}(g'A_\mu-gb_\mu^3)^2 = \frac{v^2}{8}\sqrt{g^2+g'^2}Z_\mu^2 \ ,$$

is the mass term for the neutral vector boson, Z_μ, where

$$Z_\mu = \frac{-g'A_\mu+gb_\mu^3}{\sqrt{g^2+g'^2}} \ .$$

The lepton terms in the Lagrangian can be expanded as

$$\begin{aligned}
&\bar{R}i\gamma^\mu(\partial_\mu+i\tfrac{g'}{2}A_\mu Y)R + \bar{L}i\gamma^\mu(\partial_\mu+i\tfrac{g'}{2}A_\mu Y+i\tfrac{g}{2}\mathbf{T}\cdot\mathbf{b}_\mu)L \\
&= \bar{e}_R i\gamma^\mu(\partial_\mu+i\tfrac{g'}{2}A_\mu Y)e_R + \bar{\nu}_L i\gamma^\mu[\partial_\mu+i\tfrac{g'}{2}A_\mu Y+i\tfrac{g}{2}b_\mu^3]\nu_L - \bar{\nu}_L\gamma^\mu\tfrac{g}{2}(b_\mu^1-ib_\mu^2)e_L \\
&\quad + \bar{e}_L i\gamma^\mu[\partial_\mu+i\tfrac{g'}{2}A_\mu Y-i\tfrac{g}{2}b_\mu^3]e_L - \bar{e}_L\gamma^\mu\tfrac{g}{2}(b_\mu^1+ib_\mu^2)\nu_L \ .
\end{aligned}$$

The third and fifth terms give the charged current interactions between leptons,

$$-\frac{g}{\sqrt{2}}(\bar{\nu}_L\gamma^\mu e_L W_\mu^+ + \bar{e}_L\gamma^\mu\nu_L W_\mu^-) \ .$$

Similarly, the other terms yield the interactions between the neutral gauge bosons and the leptons,

$$\frac{gg'}{\sqrt{g^2+g'^2}}\bar{e}\gamma^\mu e a_\mu - \frac{\sqrt{g^2+g'^2}}{2}\bar{\nu}_L\gamma^\mu\nu_L Z_\mu$$

$$+ \frac{Z_\mu}{\sqrt{g^2+g'^2}}[-g'^2\bar{e}_R\gamma^\mu e_R + (g^2-g'^2)\bar{e}_L\gamma^\mu e_L] \ .$$

Here,

$$a_\mu = \frac{gA_\mu + g'b^3_\mu}{\sqrt{g^2+g'^2}} \ ,$$

is identified as the photon field provided

$$\frac{gg'}{\sqrt{g^2+g'^2}} = e \ .$$

In order to incorporate other leptons into the theory, universality of the electromagnetic and weak interactions is assumed. This means that the electromagnetic and weak couplings of the other leptons and their neutrinos are assumed to be exactly the same as those for the electron and electron neutrino. The structure of the theory is duplicated for each generation of leptons added. The assumption of universality implies that all quantitative differences in the weak and electromagnetic observables of any two generations of leptons is due solely to the difference in mass of the two charged leptons (and/or neutral leptons, if allowed). More explicitly, other leptons are

incorporated in the purely leptonic standard model by including the left-handed weak-isospin doublets

$$L_\mu = \begin{pmatrix} \nu_\mu \\ \mu \end{pmatrix}, \quad L_\tau = \begin{pmatrix} \nu_\tau \\ \tau \end{pmatrix}, \quad \ldots ,$$

and the right-handed singlets $R_\mu = \mu_R$, $R_\tau = \tau_R$, etc. The Yukawa term then becomes

$$\sum_{i=e,\mu,\tau} G_i[\bar{R}_i(\phi^+ L_i)+(\bar{L}_i\phi)R_i] ,$$

where the G_i are constants that determine the different lepton masses. The mass terms and interactions with the gauge bosons and the Higgs are generated for each additional family of leptons in the same manner as for the electron and electron neutrino.

However, the purely leptonic standard model remains incomplete. In order to construct a renormalizable theory and one in closer agreement with observation, it is necessary to include quarks. Here the theory is complicated by the fact that the mass eigenstates and gauge eigenstates of some quarks are not the same. The model is expanded by including a color triplet of a weak-isospin doublet of quarks for each generation of leptons,

$$L_u = \begin{pmatrix} u \\ d' \end{pmatrix}_L, \quad L_c = \begin{pmatrix} c \\ s' \end{pmatrix}_L, \quad L_t = \begin{pmatrix} t \\ b' \end{pmatrix}_L, \quad \ldots,$$

where the color indices are suppressed and the weak hypercharge, $Y(q_L)=1/3$. The primes denote generalized Cabibbo mixing among the quarks of charge -1/3. Also, for each generation, two (color-triplet) right-handed weak-isospin singlets are included. For example, in the first generation these are

$$R_u = u_R = \frac{1}{2}(1+\gamma_5)u, \text{ where } Y = \frac{4}{3} ,$$
$$\text{and } R_d = d_R = \frac{1}{2}(1+\gamma_5)d, \text{ where } Y = -\frac{2}{3} .$$

In addition, it is necessary to introduce a new Higgs doublet,

$$\bar{\phi} = i\tau_2\phi^* = \begin{pmatrix} \bar{\phi}^0 \\ -\phi^- \end{pmatrix}, \text{ with } Y = -1,$$

in order to generate masses for the upper members of the quark doublets. The vacuum expectation value of this field that is chosen during spontaneous symmetry breaking is

$$\langle\bar{\phi}\rangle = \begin{pmatrix} \frac{v+\eta}{\sqrt{2}} \\ 0 \end{pmatrix}.$$

The Yukawa term for the quarks is

$$- G_u[(\bar{L}_u\bar{\phi})R_u+\bar{R}_u(\bar{\phi}^+L_u)] - G_d[(\bar{L}_u\phi)R_d+\bar{R}_d(\phi^+L_u)] + \ldots .$$

Upon spontaneous symmetry breaking this term generates masses for both the upper and lower members of the quark doublets. These masses depend on the constants G_u, G_d, etc. These constants must

be chosen so that u, d, s, c, etc., are mass eigenstates with the correct quark masses. The charged-current weak interaction for the first generation of quarks is of the form

$$-\frac{g}{2\sqrt{2}}\ [\ \bar{u}\gamma^{\mu}(1-\gamma_5)dW^{+}_{\mu} + \bar{d}\gamma^{\mu}(1-\gamma_5)uW^{-}_{\mu}\ ]\ .$$

The neutral-current interaction goes as

$$-\frac{g}{4\cos\theta_W}\left[\bar{u}\gamma^{\mu}[(1-\gamma^5)\tau_3-2\sin^2\theta_W Q]uZ_{\mu} + \bar{d}\gamma^{\mu}[(1-\gamma^5)\tau_3-2\sin^2\theta_W Q]dZ_{\mu}\right],$$

where

$$\frac{\sqrt{g^2+g'^2}}{g} = \cos\theta_W\ .$$

The gauge boson and Higgs boson sectors are unchanged from the purely leptonic standard model. Universality is also assumed for the quarks in the standard model. Thus, the complete fermionic structure of the theory (using the gauge eigenstates of the quarks) is duplicated for each generation.

1.2 Theoretical Possibilities

There are many theoretical models which lead to violations of universality. Some of these predict violations of ν_{μ}-ν_{e}

universality without a similar violation for the charged leptons. The experimental detection of a breakdown of universality might indicate the existence of one or more of these phenomena. This would be a very significant development and provides some of the motivation for this study. Confirmations of universality are also important because they provide constraints on the various models.

Perhaps the most straightforward of these models is the type that portrays the observed generation universality as accidental.[44] In this sort of model the electroweak coupling for each generation can differ. Improved experiments might detect this difference.

Another example of such a model is supersymmetry. The lower limits of superparticle masses have been extended in recent years by e^+e^- experiments;[3] thus, direct production of supersymmetric particles at the typical energy of E53 events is unlikely. However, virtual exchanges of supersymmetric particles could occur at this energy. The one-loop corrections to quark-lepton universality due to virtual supersymmetric particle exchanges have been calculated for charged-current weak interactions.[4] The deviation from universality comes from the fact that the lowest order corrections for muon neutrino

interactions are due to diagrams containing sleptons and gauginos, whereas those for electron neutrinos are due to diagrams containing squarks and gauginos. The signature is a slight difference in the measured weak charged-current couplings for electron neutrinos and muon neutrinos. The effect has been calculated to be as large as $O(10^{-3})$, too small to be detected by E53.

Another as-yet-unobserved phenomenon that might give an apparent violation of universality is neutrino oscillations.[5] This is a very clear example of a process that would give a violation of neutrino universality without a violation of charged particle universality. In E53, the number of expected ν_e-induced charged-current events is calculated assuming a knowledge of the ν_μ/ν_e flux ratio at the detector. If the ν_μ/ν_e flux ratio was calculated correctly at the target and changed as the neutrinos traveled to the detector, the expected integral and shape of the ν event distributions would differ from that observed. In fact, this technique has already been used to set a limit on the occurrence of neutrino oscillations using the data from E53A.[6]

Various theoretical models also speculate about the existence of neutral or charged heavy leptons. These leptons have been postulated as heavy right-handed neutrinos in grand

unified theories based on SO(10),[7] members of SU(3) octets in grand unified theories based on E_6 and E_7,[8] and recurrences of existing lepton flavors.[9] It is also conceivable that they might exist as members of new generations of leptons extending the standard model. Such heavy leptons could be produced in the target of a neutrino experiment and decay weakly in the detector, mimicking a charged-current neutrino interaction. They could also be produced in charged-current neutrino interactions and decay within the detector. One example of such a process is

$$\nu_\mu + N \rightarrow M^+ + \text{hadrons, with } M^+ \rightarrow \nu_M \nu_e e^+ .$$

The occurrence of processes such as these could cause an apparent violation of ν_μ-ν_e universality in E53. The signature might be a difference in the measured weak charged-current couplings for ν_μ and ν_e events, as well as kinematic distributions differing from those expected for charged-current neutrino interactions. Many searches have been performed for neutral and charged heavy leptons with negative results.[10] Limits set in these experiments imply that heavy lepton production should be negligible in E53.

Other examples of universality violations can be found in the many theories attempting to extend the standard model that

contain neutral, heavy, generation-changing gauge bosons. These "horizontal" currents could cause violations of universality by simply connecting fermions of different generations. This phenomenon is present in theories of extended technicolor[11] as well as grand unified theories based on SU(11), SO(14), SO(18) and those containing a separate grand unification algebra for each generation connected by the horizontal current.[12] Theories with extended technicolor have the additional possibility of pseudo-Goldstone boson exchange between generations. Lower limits for the masses of such particles have been set by experiments looking for such rare processes as

$$K_L^0 \to \mu e \ ,$$
$$K^+ \to \pi^+ e^- \mu^+ \ ,$$
$$\mu N \to eN \ ,$$
$$\mu^- \to e^- e^- e^+ \ ,$$
$$\text{and } \mu^- \to e^- \gamma \ .$$

These limits of 10-100 TeV imply that horizontal currents that couple to charged leptons are negligible at E53 energies. Of course, it is possible to imagine a horizontal current coupling only to neutrinos. The signature for this would be similar to that for neutrino oscillations.

Finally, some grand unified theories postulate the existence of families of heavy, conjugate fermions with V+A weak interactions, known as mirror fermions.[13] Fermion-mirror fermion mixing can occur in many of these models leading to modifications in the charged-current cross sections as well as some admixture of V+A in the weak interactions of fermions. The magnitude of these effects are model dependent. Some models claim they may be present at E53 energies.

In summary, there is no shortage of theories that might explain an observed violation of universality. The fact that most of them do not predict a violation at the energy and sensitivity of this experiment is in part due to existent experimental constraints on these theories.

1.3 Experimental Status of Universality

The concept of leptonic universality has a strong experimental foundation. Generally, these experiments are presented as tests of the universality of the electromagnetic interaction or of the universality of the weak interaction. However, this distinction becomes less clear for high precision experiments where it is necessary to include contributions from both interactions.

Electromagnetic muon-electron universality is well established at low energies by experiments measuring the g-factor of the muon and experiments on bound muonic systems.[14] The question of universality is addressed by comparing these observations with the predictions from QED (quantum electrodynamics), which assumes universality.

The theoretical prediction for the muon g-factor anomaly, calculated from QED with small strong and weak corrections, is,

$$a_\mu = (1165920.6 \pm 12.9) \times 10^{-9}. \quad (15)$$

This agrees well with the experimentally determined value,

$$a_\mu = (1165922 \pm 9) \times 10^{-9}. \quad (16)$$

Various bound muonic systems, such as muonium (μ^+e^-), muonic hydrogen ($H^+\mu^-$), neutral muonic helium ($He^{++}e^-\mu^-$), and heavier muonic atoms, have been seen in the laboratory. In the muonium system, the hyperfine interval $\Delta\nu$ has been measured. The agreement with theory, including radiative corrections, is impressive.

$$\Delta\nu^{exp} = (4463302.35 \pm 0.52) \text{ kHz}; \quad (17)$$

$$\Delta\nu^{th} = (4463307.3 \pm 6.5) \text{ kHz}. \quad (18)$$

In muonic helium the Lamb shift,

$$\Delta_3 = E(2p_{3/2}) - E(2s_{1/2}) ,$$

is also observed to be close to that which is predicted.[19]

$$\Delta_3^{exp} = (1527.5 \pm 0.3) \times 10^{-3} ;$$
$$\Delta_3^{th} = (1527.0 \pm 4.2) \times 10^{-3} .$$

Also, radiative corrections to the energy levels of heavy muonic atoms show close agreement with observation.[20]

Electromagnetic universality for leptons also seems to hold at higher energies.[21] For example, no significant differences are found in comparisons between data from elastic and inelastic scattering of muons on protons and data from comparable experiments with electrons.[22] In another example, the reactions

$$e^+ + e^- \rightarrow e^+ + e^-,$$
$$e^+ + e^- \rightarrow \mu^+ + \mu^-,$$
$$\text{and } e^+ + e^- \rightarrow \tau^+ + \tau^-,$$

have been observed simultaneously at center-of-mass energies up to 31.6 GeV. The observed cross sections agree well with the predictions of QED.[23]

The most precise test of weak interaction muon-electron universality at low energies is given by measurements of the branching ratios for the electronic and muonic decay modes of the charged pion. The theoretical value has been determined to be,[24]

$$R \equiv \frac{\Gamma(\pi \to e\nu_e + \pi \to e\nu_e\gamma)}{\Gamma(\pi \to \mu\nu_\mu + \pi \to \mu\nu_\mu\gamma)} = 1.233 \times 10^{-4}.$$

This value is in good agreement with the observed value,[25]

$$R = (1.218 \pm 0.014) \times 10^{-4}.$$

At higher energies, weak interaction universality has been tested in a variety of ways. A very direct test at high $Q^2 \simeq m_W^2$ has been done at the CERN $p\bar{p}$ collider. Measurements of the relative rates for $W \to e\nu$, $W \to \mu\nu$, $W \to \tau\nu$, $Z \to e^+e^-$, and $Z \to \mu^+\mu^-$, have been made by UA1.[26] These measurements give the following results, consistent with universality:

$$\frac{g_\tau^{cc}}{g_e^{cc}} = 1.01 \pm 0.09(\text{stat}) \pm 0.05(\text{syst}),$$

$$\frac{g_\mu^{cc}}{g_e^{cc}} = 1.05 \pm 0.07(\text{stat}) \pm 0.08(\text{syst}),$$

and

$$\frac{\sigma_\mu^{nc}}{\sigma_e^{nc}} = 1.01 \pm 0.09(\text{stat}) \pm 0.05(\text{syst}).$$

Recently, measurements of the τ lepton lifetime have been made at the Stanford Linear Accelerator Center (SLAC) using the PEP e^+e^- storage ring operating at 29 GeV center-of-mass energy.[27] The values of

$$\text{(MARK II)}\ \tau_{tau} = (2.88 \pm 0.16 \pm 0.17) \times 10^{-13}\ \text{sec} \quad ,$$

$$\text{(MAC)}\ \tau_{tau} = (3.09 \pm 0.19) \times 10^{-13}\ \text{sec} \quad ,$$

$$\text{and} \quad \text{(HRS)}\ \tau_{tau} = (2.99 \pm 0.15 \pm 0.10) \times 10^{-13}\ \text{sec}$$

are in agreement with theoretical calculations that assume universality.[28]

A number of different experiments have looked for electroweak interference at high energies. It has been reported in eD scattering at SLAC, $\mu^{\pm}C$ scattering at CERN (BCDMS) in Geneva, Switzerland, and e^+e^- experiments at SLAC and at DESY in Germany. Each of these experiments can measure some combination of the vector and axial vector parts of the neutral current coupling to fermions. In e^+e^- experiments the angular dependence of $e^+e^- \rightarrow \mu^+\mu^-$ differs in an asymmetric way from that predicted by pure QED. This difference is due to the additional process $e^+e^- \rightarrow Z \rightarrow \mu^+\mu^-$. This forward-backward asymmetry is proportional to

$$\underset{\text{axial vector}}{g_e^{nc}} \qquad \underset{\text{axial vector}}{g_\mu^{nc}} \ .$$

In the scattering experiments, electroweak interference causes differences in the cross section for different beam charges and polarizations. These asymmetries can be used to derive measurements of several different combinations of quark and lepton coupling constants. A four parameter fit to the combined νe, eD, e^+e^-, and $\mu^\pm C$ data yields[29]

$$g_{e\,\text{vector}}^{nc} = 0.02 \pm 0.06 \qquad g_{e\,\text{axial vector}}^{nc} = -0.54 \pm 0.03$$

$$g_{\mu\,\text{vector}}^{nc} = -0.05 \pm 0.16 \qquad g_{\mu\,\text{axial vector}}^{nc} = -0.51 \pm 0.05 \ .$$

Also results from e^+e^- experiments give[30]

$$g_{\tau\,\text{axial vector}}^{nc} = -0.38 \pm 0.09 \ .$$

Universality requires that both the neutral current vector and axial vector constants be the same for each generation. The standard model predicts (for $\sin^2\theta_W = 0.23$)

$$g_{1\,\text{vector}}^{nc} = -\frac{1}{2} + 2\sin^2\theta_W = -0.04 \quad \text{and} \quad g_{1\,\text{axial vector}}^{nc} = -\frac{1}{2} \ .$$

Thus, these measurements are consistent with both universality and the standard model.

Many experiments examining the question of weak interaction universality have been done using neutrino beams. Some of these experiments have used beams generated by conventional sources, i.e., π and K meson decay in flight. Others have used beams created by a beam-dump, where the target is very large and the neutrino flux from conventional sources is greatly reduced. In these beams the neutrinos from other sources, known as prompt neutrinos, are easier to see. These neutrinos are thought to be due to the production and subsequent semileptonic decays of charmed particles in the beam-dump. From 1979-1982 there were indications of an apparent violation of universality in some of these beam-dump experiments.[31] The ratio of prompt $\nu_e+\bar{\nu}_e$ to $\nu_\mu+\bar{\nu}_\mu$ was found to be significantly less than one. However, more recent measurements of this ratio are consistent with unity.[32]

The results coming from experiments using conventional sources for neutrinos have been more consistent. The CHARM collaboration at CERN has used a statistical method taking advantage of the characteristics of narrow band beams to determine

$$\frac{\sigma^{nc}_{\nu_e}}{\sigma^{cc}_{\nu_e}} = 0.27 \pm 0.19 \quad \text{and} \quad \frac{\sigma^{cc}_{\nu_e}}{\sigma^{cc}_{\nu_\mu}} = 1.2 \pm 0.11$$

at $Q^2 \simeq 16$ GeV^2.[33] The standard model predicts the neutral-current to charged-current cross section ratio to be 0.33 for neutrinos and 0.39 for antineutrinos.[34]

A number of bubble chamber experiments have also looked at ν_e-ν_μ universality in narrow and wide band neutrino beams. These experiments tend to have relatively low statistics; however, they can test universality by examining many things that counter experiments cannot, such as strange particle production and kinematic distributions. These experiments are reviewed here in some detail since they are very similar to E53.[69]

One such experiment, using the bubble chamber Gargamelle at CERN, filled with CF_3Br, reported observing 200 ν_e-induced events and 60 $\bar{\nu}_e$-induced events with $E_\nu < 10$ GeV.[35] In this experiment the electron momentum was reconstructed from the measured total track length. No difficulties in electron momentum reconstruction were reported. The cross section ratios were determined to be

$$\frac{\sigma^{CC}_{\nu_e}}{\sigma^{CC}_{\nu_\mu}} = 0.95 \pm 0.30 \quad \text{and} \quad \frac{\sigma^{CC}_{\bar{\nu}_e}}{\sigma^{CC}_{\bar{\nu}_\mu}} = 0.89 \pm 0.30 \ .$$

The y distribution for the $\nu_e(\bar{\nu}_e)$ events was found to be very similar to the comparable $\nu_\mu(\bar{\nu}_\mu)$ distribution. Perhaps the most interesting result reported by this group was the strange particle rate for ν_e interactions. They found

$$\frac{\nu_e N \to e^- V^o X}{\nu_e N \to e^- X} = (3.8 \pm 1.7)\% \ .$$

This result was compared to the corresponding ν_μ result corrected for the differences in spectra,

$$\frac{\nu_\mu N \to \mu^- V^o X}{\nu_\mu N \to \mu^- X} = (1.0 \pm 0.09)\% \ .$$

The Gargamelle collaboration regarded the statistics as too poor to claim significant disagreement between these two numbers.

A similar experiment, using the Big European Bubble Chamber (BEBC) at CERN, filled with NeH_2, was performed at higher energies.[36] In this experiment, 105 ν_e and $\bar{\nu}_e$ events were observed during an exposure of BEBC to a neutrino beam generated by 350 GeV proton collisions. They were able to obtain a ±25% momentum measurement for electrons with $P_e \lesssim 25$ GeV/c by using a method developed in another experiment where individual electrons were first measured in H_2 and then in NeH_2. Each electron was

measured up to the first visible energy loss. All observed bremsstrahlung gammas emitted from the measured part of the track were measured in the same way and the momenta summed with that of the primary electron. They found

$$\frac{\sigma^{CC}_{\nu_e}}{\sigma^{CC}_{\nu_\mu}} = 1.21 \pm 0.19 \ .$$

They also compared E_ν, x, y, P^T_{had}, P^T_e, and P_e for the ν_e-induced events to events generated by Monte Carlo assuming universality. The distributions are in close agreement with the Monte Carlo predictions.

Finally, a group at Fermilab in Batavia, Illinois, (LBL, Hawaii, Washington) reported the observation of 60 ν_e-induced events and 35 $\bar{\nu}_e$-induced events during an exposure of the 15-ft bubble chamber to a single-horn focussed $\bar{\nu}$ beam.[37] The events ranged in energy from 10-150 GeV. The electrons were reconstructed using a modified Behr-Mittner method. As discussed in Appendix B, hard bremsstrahlung can give an inaccurate reconstruction of the electron momentum. In order to compare the kinematic distributions for the $\nu_e(\bar{\nu}_e)$ events with those for $\nu_\mu(\bar{\nu}_\mu)$ events, this group used a Monte Carlo to smear the muon tracks in the $\nu_\mu(\bar{\nu}_\mu)$ sample. The momentum was varied randomly

within a gaussian centered on the measured momentum with a FWHM that varied as a function of momentum. They examined E_{vis}, x_{vis}, y_{vis}, $U_{vis} \simeq x(1-y)$, $\sin^2(\theta_{lep}/2)$, and the charged particle multiplicity for $\nu_e(\bar{\nu}_e)$ and $\nu_\mu(\bar{\nu}_\mu)$ events. The distributions for the two generations are very similar, as universality requires. The one exception is the ν_μ-ν_e x_{vis} comparison. At very low x, there is a two-standard deviation excess of ν_e events. This was not thought to be significant in view of the good agreement in all the other distributions.

The analysis presented in this thesis represents a significant improvement in both statistics and method over previous bubble chamber experiments examining universality. The sample of ν_e and $\bar{\nu}_e$-induced events examined herein is roughly ten times larger than those reported previously. A technique is developed in Chapter 3 and Appendix B that is very similar to that used by the LBL, Hawaii, Washington group for constrasting $\nu_\mu(\bar{\nu}_\mu)$ and $\nu_e(\bar{\nu}_e)$ distributions. However, the method developed here uses the fact that the ν_e and $\bar{\nu}_e$ flux spectra differ from the ν_μ and $\bar{\nu}_\mu$ spectra. It also uses a superior technique for smearing the electron momentum resolution. In addition, these comparisons are good for events with P_e from 2 to 200 GeV rather than just those with $P_e \lesssim 25$ GeV. The cross section ratios determined in this thesis have errors comparable to those in

previous measurements. The distribution, multiplicity, strange particle rate, and dilepton rate comparisons presented here represent a significant improvement over previous measurements; it is unlikely they will be improved upon in the foreseeable future.

CHAPTER 2: DATA ACQUISITION AND REDUCTION

The data for this analysis come from two experiments performed at the Fermi National Accelerator Laboratory (FNAL). Both experiments involved exposing the FNAL 15-foot bubble chamber to a wide band ν beam generated by 400 GeV protons. The two experiments are referred to in this thesis as E53A and E53B. The data for E53A is comprised of approximately 132,000 photographs taken between April of 1976 and May, 1977. That for E53B is made up of approximately 260,000 photographs taken from December, 1980 to February, 1981. Each data set contains roughly 80,000 ν_μ charged-current events inside the fiducial volume.

2.1 The Neutrino Beam

The ν beam for each of these experiments[38] was generated by the decay of secondary mesons formed by 400 GeV protons incident on a target made up of approximately one interaction length of Al_2O_3, for E53A, or BeO, for E53B. The basic layout of each experiment is shown in figure 1.

The secondaries formed in the target were mostly π and K mesons. Following their production in the target, the mesons

passed through a magnetic horn. Although the magnetic horn systems differed for the two experiments, the basic method was the same. Each horn consisted of two concentric thin-walled conductors. Current flowed away from the target through the inner conductor and back toward the target through the outer conductor. The magnetic field set up between the conductors was such that the positively charged mesons passing through the horn were focused toward the bubble chamber while the negative mesons were turned away. More details concerning the magnetic horns are given in figures 2 and 3.

Following the magnetic horn(s), those secondaries continuing toward the bubble chamber entered a 400 meter evacuated decay pipe. In this region, most of the secondaries decayed leptonically or semileptonically. The decays which are the dominant source of neutrinos are listed at the end of Appendix A. Some of the neutrinos formed in these decays continued in the same approximate direction, passing through the bubble chamber. Following the decay pipe was a one kilometer beam dump and earth shield that ranged out the muons and stopped the remaining hadrons, electrons, and photons, leaving only the neutrinos in the beam. The neutrino beam consisted of ν_μ, ν_e, $\bar{\nu}_\mu$, and $\bar{\nu}_e$. The flux ratio of these different types of neutrinos has been estimated by a Monte Carlo computer program for both E53A and

E53B. These calculations give the following relative neutrino flux and event rate ratios:

	ν_μ	$\bar{\nu}_\mu$	ν_e	$\bar{\nu}_e$
E53A flux	100.	1.24	0.59	0.09
E53A events	100.	0.83	0.95	0.07
E53B flux	100.	13.9	1.06	0.43
E53B events	100.	8.0	1.84	0.34

The flux ratios depend only on the π and K production spectra and the geometry of the beamline. The charged-current event rate ratios also have a dependence on the cross section. The event rates given here are calculated assuming universality, i.e., the cross section for the $\nu_e(\bar{\nu}_e)$ events is assumed to be the same as that for the $\nu_\mu(\bar{\nu}_\mu)$ events. More details about these calculations are given in Appendix A.

2.2 The Bubble Chamber

As seen in figure 4, the Fermilab 15-foot bubble chamber is comprised of a 12-foot diameter sphere with a 3-foot conical protrusion in the direction of the beam. There is a hydraulic piston in the bottom of the chamber used for pressure variation, and six ports for cameras in the top. A pair of superconducting Helmholtz coils lie just outside the chamber. During these experiments the coils carried 5000 amperes, providing a vertical

magnetic field of 30 kG, uniform to approximately 15% throughout the chamber. The 15-foot bubble chamber is a cryogenic chamber designed to work with liquids at temperatures of 25 to 33 K and 2-10 atmospheres of pressure.

Between pulses in a neutrino experiment, the chamber is kept at a pressure of approximately one atmosphere above the vapor pressure of the enclosed liquid to eliminate boiling. Just before a pulse of neutrinos enters the chamber, the piston drops, lowering the pressure within the chamber to 2-5 atmospheres below the vapor pressure of the liquid. Charged particles traversing the chamber (hopefully generated by a neutrino interaction) leave trails of ionization in the liquid. Bubbles form around this energy deposition in the superheated liquid, growing as the square root of time. After 6 to 10 milliseconds, these bubbles have grown to approximately 500 μm in diameter and are photographed. This process is illustrated in figure 5.

The fill used in these experiments was a Ne-H_2 64/36 atomic percent mixture. The odd percentage was dictated by the availability of neon. The boiling point of this liquid is 29.5 K and the density is 0.77 grams/cc. There were multiple reasons for choosing this mixture. First, it is a very heavy liquid and the usable volume of the bubble chamber contained about

18.8×10^3 kg of the fill. This large mass gave a reasonable event rate for ν interactions. The short radiation length of approximately 40 cm allowed for very good electron identification. Also, the interaction length of this liquid was experimentally determined to be 125 cm.[70] This was short enough to provide good hadron identification, since 75% of the charged hadrons visibly interacted before they left the chamber. Finally, 97% of all interactions in the chamber took place on a Ne nucleus. Since Ne has an isospin of zero, the π^--Ne and π^+-Ne hadronic interaction cross sections are the same. This fact was helpful in estimating the magnitude and energy dependence of the π^--μ^- ambiguity (punchthrough background) discussed in Chapter 3.

Three cameras were used in these experiments. Two views provided enough information to reconstruct events in the chamber. The third view provided some redundant information and a reduction in the positional error of reconstructed points. The three separate views were also useful in determining the presence of neutral strange particles (vees) and Dalitz pairs.

2.3 Scanning and Measuring

The data for E53A, consisting of ~132,000 frames of 70 mm film on 76 rolls, was evenly divided for analysis at Brookhaven

National Laboratory (BNL) and Columbia University's Nevis Laboratory (CU or Nevis). The data for E53B was divided for analysis among CU, BNL, and Rutgers University. Of the ~260,000 frames on 153 rolls, roughly 104,000 were sent to Nevis, 71,000 to BNL, and 85,000 to Rutgers.

The first step in the analysis was to scan the film and measure those events of interest. Measuring is the process of digitizing an event for further analysis with a computer. This work was done on scan tables with dual magnifications of 15X and 70X. The high magnification produced images on the tables that were approximately full scale. Since the film stages were moved during a measurement while the optical system and tables were stationary, the quality of the measurement was not affected by any optical distortions. The least count for these tables was 2.54μ on film and measurements of a precision grid typically gave an rms scatter of less than 4μ on film.

The film was scanned by highly skilled technicians for many types of event topologies, each representing a different physical process of interest. Those processes of interest for this analysis were the following:

ν_μ charged-current interaction $\equiv$ $\nu_\mu + Ne \rightarrow \mu^- + \text{hadrons}$,

$\bar{\nu}_\mu$ charged-current interaction $\equiv$ $\bar{\nu}_\mu + Ne \rightarrow \mu^+ + \text{hadrons}$,

ν_e charged-current interaction $\equiv$ $\nu_e + Ne \rightarrow e^- + \text{hadrons}$,

and

$\bar{\nu}_e$ charged-current interaction $\equiv$ $\bar{\nu}_e + Ne \rightarrow e^+ + \text{hadrons}$.

Feynman diagrams of these processes are shown in figures 9, 10, and 12. The scans for the ν_e and $\bar{\nu}_e$ charged-current events were called the electron and positron scans, respectively. The scan for the ν_μ and $\bar{\nu}_\mu$ charged-current events was called the normalization scan.

For the electron and positron scans, all events with an e^- or e^+ coming from the vertex were recorded. The e^- or e^+ was required to be straighter than a 300 MeV template on the table. To be identified as an e^- or an e^+, the track was required to exhibit two signatures characteristic of electrons in a heavy Ne-H_2 fill. These signatures are illustrated in figure 6. Converted gammas pointing back tangentially to the candidate track were each considered a good signature. The probability of a particle of mass M and energy E to radiate a photon with energy E′ is given by Rossi as[39]

$$\Phi(E,E')dE' = \alpha\frac{N}{A}Z^2 r_e^2 \frac{m_e^2}{M^2}\frac{dE}{E'}F(U,v) \ .$$

The $1/M^2$ dependence of this probability makes the bremsstrahlung by particles other than electrons negligible for this analysis.

The rapid loss of energy by radiation also contributed to another characteristic electron signature used in this

experiment, the curl at the end of the track. The other, more massive particles seen in this experiment did not lose energy at as high a rate as electrons; and those pions and muons that slowed down enough to begin to curl up in the magnetic field usually decayed or interacted first.

δ-rays of energy comparable to the primary track were also used as an electron signature in this experiment. The maximum energy a knock-on electron can be given by a particle of mass M and energy E is[40]

$$E'_{max} = \frac{2m_e P^2}{M^2 + 2m_e E} \quad .$$

δ-rays with an energy that is much less than that of the primary track can be generated by massive particles like muons and pions as well as electrons. However, due to the kinematical limit described above, only electrons can produce δ-rays with energies comparable to that of the primary track.

Finally, for positrons an additional signature was accepted. Occasionally they would stop and annihilate with both gammas converting in the chamber and pointing back to the position of annihilation. This signature was both striking and unambiguous.

The electron events were also subjected to an edit by physicists. Each event was carefully examined. Electrons coming from probable Dalitz pairs, δ-rays, and close-in converted gammas were eliminated at this stage. Event information from the reconstruction programs (TVGP and SQUAW) was also checked during this edit. Two actual events are shown in figures 7 and 8.

For the normalization scan, all events were recorded that appeared to come from a neutral particle traveling in the ν beam direction. A reduced sample of frames was used for this scan. To avoid roll-to-roll variations in beam intensity, thirty or forty frames were selected from each roll for this scan. This corresponds to roughly 1.5% of the total number of frames available for each run.

2.4 Event Reconstruction

After being measured, each event was reconstructed by a computer program called TVGP (Three View Geometry Program).[41] This program fit a three-dimensional track to the data given in the form of three two-dimensional sets of coordinates. Starting with a circular track in a uniform magnetic field, TVGP adjusted the track parameters to minimize the χ^2 of the fit. Each track was fit assuming proton, muon, pion, and electron mass

hypotheses. TVGP took into account the actual magnetic field distribution in the bubble chamber, optical distortion, ionization energy loss, and multiple Coulomb scattering. TVGP gave as output the coordinates of the vertex, the momentum vector of each track (for each mass hypothesis), and the errors in these quantities.

Because electrons also lose a substantial fraction of their energy through bremsstrahlung, a special method was developed to handle electron tracks in TVGP.[42] In this method, the electron bremsstrahlung is categorized as 'hard' and 'soft'. Hard bremsstrahlung leads to a visible change of curvature in the electron track whereas soft bremsstrahlung does not. The soft bremsstrahlung is compensated for by integrating the classical radiation spectrum up to a cutoff value and taking into account this energy loss. The cutoff value, taken to be half the electron energy, was such that the electron loses 39% of its energy traversing one radiation length of material. To lessen the effect of the hard bremsstrahlung an iterative cutback technique was used. An rms was calculated for a fit using all the measured points. Then the length of the track was cut back by 10% and a new fit was made. This was repeated up to ten times and each rms was saved. The fit with the longest length and no more than 1.2 times the lowest rms was used. In summary, the

length chosen gives the best fit to the model that the electron lose 39% of its energy in one radiation length. An additional correction for hard bremsstrahlung was considered at a later stage in the analysis (see Appendix B and Chapter 3).

After TGVP, the data were processed through the program SQUAW.[41] This program kinematically fit all the measured vees. A vee is a term used to describe a neutral particle decay or conversion into two charged particles. For each vee, a fit was made to the following hypotheses:

$$K_s^o \rightarrow \pi^+\pi^-,$$
$$\Lambda^o \rightarrow P\pi^-,$$
$$\bar{\Lambda}^o \rightarrow \bar{P}\pi^+,$$

and $\gamma \rightarrow e^+e^-$ (with a spectator proton).

First, SQUAW made an unconstrained fit where the direction and mass of the decaying neutral were treated as free parameters. Then the vee was reconstructed using a constrained fit. In this case, the mass was chosen to be one of the above hypotheses and the direction was constrained to be along the line defined by the event vertex and the vee vertex. SQUAW returned the parameters for each attempted fit as well as the χ^2 for each constrained fit.

2.5 Data Reduction

The data were prepared for final analysis by the program MKDST.[43] This program was responsible for the following things: making the fiducial volume cut, choosing the mass hypothesis for each track, reconstructing short interacting tracks and neutron stars, determining the visible energy for each event, making a χ^2 cut on the fitted vees, and resolving fitted vee ambiguities.

The coordinate system used to define the position of events in the bubble chamber is such that the origin is in the center of the sphere (180 cm radius) that makes up the bulk of the chamber. The beam travels in the +X-direction. The +Z-axis points up toward the cameras. The fiducial volume used in this analysis is defined as follows:

$$|Z| \leq 125 \text{ cm},$$

$$\sqrt{X^2 + Y^2 + Z^2} \leq 170 \text{ cm},$$

$$\text{and } \sqrt{(X+70)^2 + Y^2 + Z^2} \leq 180 \text{ cm}.$$

Events with the primary vertex lying outside this region were eliminated from the sample. The first cut removed events close to the cameras and those near the bottom of the chamber. The large bubble size on the film for events close to the cameras and

the loss of resolution for interactions far away prohibited accurate measurements for these events. The second cut eliminated events within 10 cm of any wall. This was to decrease the possibility that the incoming neutral particle inducing the event was from an interaction just outside of or in the bubble chamber wall. The final cut was made to exclude events within 70 cm of the back wall of the bubble chamber. This was necessary to insure good particle identification, allow room for neutral particles to decay or interact, reduce the momentum measurement error on each charged track ($\Delta p/p$ goes as $1/\text{length}^2$) and reduce the pion punchthrough background.

MKDST made use of codes set by the scanners in choosing the mass hypothesis for each track. The electron hypothesis was chosen for those tracks flagged as electrons by the scanners. Interacting charged tracks were called pions. Short, stopping tracks were called protons. In the normalization sample, the muon hypothesis was chosen for the fastest leaving track of the appropriate charge. All other leaving tracks were called pions. For the e^+ and e^- samples, the pion hypothesis was chosen for all leaving tracks.

The secondary tracks emanating from neutron interactions and short interacting charged tracks were measured and the

measurements used to reconstruct the primary tracks from the vertex in MKDST. The procedure was to sum the secondary track energies subtracting the target mass of one proton. This value was corrected for unseen neutrals using the PIK method described in Chapter 3. The end result of this was taken to be the total energy of the primary track. For neutron interactions (neutron stars) the mass was assumed to be that of the neutron. For interacting charged tracks, the pion mass was assumed. From this information, the magnitude of the momentum of the primary track was calculated. The direction was defined by the vector pointing from the primary vertex to the point of interaction.

The total visible energy of each event was determined by MKDST. This quantity was constructed by summing the total energy of each track and neutral particle, with the exception of baryon tracks. For baryons, only the kinetic energy was used in this sum. This corrects the final visible energy for the target mass in the primary neutrino interaction and for the target mass involved in reinteractions inside the Ne nucleus.

A χ^2 cut on fitted vees was made in MKDST. Only two- and three-constraint fits with a χ^2 per degree of freedom less than or equal to five were kept in the sample. Roughly one third of the vees in the various samples had an acceptable fit for more

than one hypothesis. These ambiguities were resolved in MKDST by examining the cosine of the angle between the vee line of flight and the negative decay product in the rest frame of the vee. For the spinless K_s^o this distribution should be flat. For the Λ^o and $\bar{\Lambda}^o$, this distribution should also be flat assuming they were not longitudinally polarized during production. The fit ambiguities were resolved using an algorithm that made these distributions as flat as possible. For a K_s^o/Λ^o ambiguity, the Λ^o fit was chosen if the probability for the Λ^o fit exceeded 0.5 times the probability for the K_s^o fit. For a $K_s^o/\bar{\Lambda}^o$ ambiguity, the K_s^o fit was chosen if the probability for a K_s^o fit exceeded 0.3 times the $\bar{\Lambda}^o$ probability. Finally, for a $\Lambda^o/\bar{\Lambda}^o$ ambiguity, the vee was selected to be a Λ^o if the Λ^o probability exceeded 0.5 times the $\bar{\Lambda}^o$ probability.

The output from MKDST was in a condensed data format. The events were completely reconstructed with ambiguities resolved. At this stage the data were considered ready for final analysis.

CHAPTER 3: ANALYSIS AND RESULTS

3.1 Electron neutrinos and antineutrinos

The object of this analysis was to isolate and characterize ν_e and $\bar{\nu}_e$ charged-current events. Feynman diagrams of these processes are shown in figures 9 and 10. The candidate events were identified by scanning all frames for events with an electron or positron coming from the vertex. After measuring, reconstructing, and editing each event as described in Chapter 2, there were the following numbers of candidate events inside the fiducial volume:

E53A	654	events with an e^- (ν_e candidates)
	278	events with an e^+ ($\bar{\nu}_e$ candidates)
E53B	1100	events with an e^- (ν_e candidates)
	407	events with an e^+ ($\bar{\nu}_e$ candidates).

Events with both an e^- and an e^+ were categorized during the edit stage using(the momenta of the electrons and the presence of other tracks as criteria. For example, if the e^- and e^+ tracks were separated in at least one view and the e^- was not consistent with being a δ-ray then the event would be categorized according to which lepton was the most energetic.

3.1.1 Backgrounds

Backgrounds to these events include asymmetric gamma conversions, asymmetric Dalitz pairs, deltas, Compton electrons, and K or π decays (producing an $e^{\pm}$) occurring close to the vertex in ν_μ charged-current or neutral-current events. All of these backgrounds fall with rising electron (positron) momentum. Taking advantage of this, all events with a primary e^- (e^+) momentum of less than 2 GeV/c were removed from the candidate samples. This cut removed a total of 330 e^- events and 220 e^+ events from the two runs.

The background due to deltas has been discussed extensively in previous E53 work.[45] The requirements that the angle between the primary electron and any muon or hadron be greater than 4° and that the electron have no greater than one-half of the maximum kinetically allowed energy were sufficient to remove this background. These cuts take advantage of the fact that deltas tend to be produced at small angles with the incoming particle and that for a given incoming particle of mass M and momentum P, the maximum kinetically allowed delta energy is

$$E_\delta^{max} = 2m_e \frac{P^2}{m_e^{\,2} + M^2 + 2m_e(P^2+M^2)^{1/2}} \quad .$$

This cut removed 21 events from the combined ν_e candidate sample.

The e^+ sample contains a significant background from $\mu^- e^+$ events, i.e., ν_μ-induced dilepton events. These events come from charm production in ν_μ charged-current events. A Feynman diagram of this process is shown in figure 11. Since the muon in these events leaves the bubble chamber without interacting, this background was easily removed by requiring that the $\bar{\nu}_e$ candidates not have a negative leaving track. This cut removed 286 of the remaining 465 e^+ events.

The backgrounds due to close-in asymmetric gamma conversion and close-in asymmetric Dalitz pair production have been estimated in a previous study of Dalitz pairs and gamma conversions using E53 data.[46] It was experimentally determined that there are

$$\frac{.18 \pm .04 \text{ asymmetric pairs}}{27600\ \nu_\mu \text{ cc events}} \text{ for } P_e > 2\ \frac{\text{GeV}}{c} \quad .$$

'Asymmetric pair' means either a close-in Dalitz pair or a close-in gamma conversion to an e^+e^- pair where one prong has a momentum of less than 5 MeV/c, i.e., a radius of curvature of less than .5 cm. This radius was determined to be the lower limit for a track that the scanners could reliably see.

The upper limit for the Compton background remaining after the lepton momentum and delta cuts was obtained by using the results of a calculation that yielded [47]

$$\frac{\text{Compton Electrons}}{\text{Asymmetric Gamma Conversions}} \simeq 6 \quad .$$

Assuming all asymmetric pairs to be gamma conversions gives an upper limit for the Compton background of

$$\frac{1.1 \pm 0.3 \text{ Compton electrons}}{27600\ \nu_\mu \text{ cc events}} \text{ for } P_e > 2\ \frac{\text{GeV}}{c} \quad .$$

Finally, the upper limits for the backgrounds from K_{e3} decays remaining after the $P_e > 2$ GeV/c cut have been estimated to be [48]

$$2.2 \pm 0.6\ \frac{e^-}{10^5\ \nu_\mu \text{ cc events}} \text{ and } 1.4 \pm 0.6\ \frac{e^+}{10^5\ \nu_\mu \text{ cc events}} \quad .$$

Other K and π decays leading to an electron or positron background have been calculated to be negligible compared to the charged K_{e3} decays.

The following table summarizes the effect of the lepton momentum, delta, and L^- cuts on the ν_e and $\bar{\nu}_e$ candidate samples. It also shows the size of the remaining backgrounds assuming

there are 163700 ± 8800 ν_μ charged-current events and 10700 ± 1600 $\bar{\nu}_\mu$ charged-current events in the total E53 sample (inside the fiducial volume).

	ν_e Candidates	$\bar{\nu}_e$ candidates
	1754	685
$P_e > 2 \frac{GeV}{c}$ cut	- 330	- 220
Delta cut	- 21	
L^- cut		- 286
	1403 ± 37	179 ± 13
Asymmetric pairs	- 1.5 ± .3	- 0.44 ± .1
Compton	- 9.3 ± 2.5	
K_{e3}	- 5.1 ± 1.4	- 1.0 ± 0.4
Final samples	1387 ± 37	178 ± 13

3.1.2 Corrections

The number of ν_e and $\bar{\nu}_e$ candidates remaining after the cuts and background subtraction described above were corrected for losses and efficiencies. These corrections are summarized in table I and described in greater detail below. After corrections, the final number of ν_e events inside the fiducial volume was 2089 ± 137 and the corresponding number for $\bar{\nu}_e$ events was 336 ± 34.

The number of good ν_e candidates lost due to the delta cut was (0.6 ± 0.6)%. This was calculated by observing the loss of good $\bar{\nu}_e$ events using similar criteria. The positrons in these events are not knock-on atomic electrons; their elimination by this cut represents a loss of good events.

The loss of good candidates due to the $P_e > 2$ GeV/c cut was estimated to be (6 ± 1)% for the ν_e sample and the $\bar{\nu}_e$ sample. These numbers come from a study of large samples of Monte Carlo generated ν_e and $\bar{\nu}_e$ events. The Monte Carlo package assumed universality and smeared the electron momenta with a method that utilized the EGS4 code from SLAC. This technique will be described in greater detail later in this chapter.

The loss of legitimate $\bar{\nu}_e$ charged-current events due to the L^- cut was estimated to be (25 ± 5)%. This number was calculated from the $\bar{\nu}_e$ sample. For each event in the $\bar{\nu}_e$ charged-current sample with N interacting (I^-) tracks, N weights were calculated. The ith weight represented the probability that the ith I^- track leave the chamber mimicking a muon. Each weight was corrected for those $\bar{\nu}_e$ events already lost from the sample by dividing the weight by the probability that none of the I^- tracks leave the chamber. More explicitly, w_i was calculated in the following manner:

$$P_i = e^{-\frac{d_i}{125}} ,$$

$$\bar{P}_i = \prod_{\substack{j=1 \\ j\neq i \\ E_j > E_i}}^{N} \left(1 - e^{-\frac{d_j}{125}}\right) ,$$

$$S_i = \prod_{j=1}^{N} \left(1 - e^{-\frac{d_j}{125}}\right) ,$$

$$\text{and } w_i = \frac{P_i \bar{P}_i}{S_i} ,$$

where d_i is the extrapolated distance to the bubble chamber wall (in cm) for the ith track. The sum of these weights for all the $\bar{\nu}_e$ events represented the number of $\bar{\nu}_e$ charged-current events lost due the the L^- cut.

There was an additional loss of events that were too confused to be measured or edited. This confusion came from many different sources such as high multiplicity, high energy close-in gamma conversions, bad picture quality, or overlapping events. This loss, termed the splat loss, was estimated to be (10 ± 5)% by examining scan and edit notes.

The scanning efficiency for events containing electrons or positrons coming from the vertex was determined to be (84 ± 5)% for E53A [49] and (77 ± 2)% for E53B.[50] These efficiencies were determined by double scanning significant portions of the film.

Finally, the electron (positron) identification efficiency was carefully determined by examining converted gammas in the bubble chamber.[51] This efficiency is a measure of the probability that an e^- (e^+) have the two or more signatures necessary to be identified as an electron (positron) by the scanners. This efficiency was found to be (98 ± 2)% for electrons and positrons of momenta greater than 2 GeV/c.

3.2 Muon Neutrino and Antineutrino Samples

The normalization samples of ν_μ and $\bar{\nu}_\mu$ charged-current events were created from a sample recorded during a scan of 5250 ± 70 frames scattered throughout the data. This represents 1.3% of the total film. During this normalization scan, the scanners measured any event in the bubble chamber created by a neutral particle traveling in the ν-beam direction.

3.2.1 Event Selection

Charged-current ν_μ events were defined to be events inside the fiducial volume with $E_\nu > 10$ GeV that had at least one leaving negative track. In addition (see Appendix C),

$$y_{L^-} = \frac{E_{hadrons}}{E_{total}} < 0.85$$

was required where the muon was assumed to be the highest momentum leaving negative (L^-) track. The energy cut was necessary to eliminate the background from neutrons and neutral strange particles. The y cut reduced the neutral-current and $\bar{\nu}_\mu$ charged-current contamination from hadron punchthrough. Events with high-y had a relatively low lepton momentum and there was a significant background due to hadrons that left the chamber.

Similarly, the $\bar{\nu}_\mu$ charged-current sample was defined to be those events inside the fiducial volume with a leaving positive track passing the y cut and no leaving negative track and $E_\nu > 10$ GeV. The requirement of no L^- track eliminated the background from charged-current ν_μ events and reduced the background from neutral-current events with hadron punchthrough.

Those events not satisfying the ν_μ or $\bar{\nu}_\mu$ charged-current event requirements were placed in the 'neutral-current' sample. This is a bit of a misnomer since no attempt was made to isolate true neutral-current events in this analysis.

3.2.2 Backgrounds

Having defined the various categories in the manner described above, the normalization sample yielded the following for both runs combined:

1501 ν_μ charged-current candidates,

99 $\bar{\nu}_\mu$ charged-current candidates,

499 neutral-current candidates.

This method gave a ν_μ charged-current sample that still contained a significant contamination of neutral-current and $\bar{\nu}_\mu$ charged-current events with a leaving negative hadron. Similarly the $\bar{\nu}_\mu$ charged-current sample had a significant background from neutral-current events with a leaving positive hadron. This contamination had to be taken into account when calculating the final numbers of events as well as during the creation of event distributions for each sample.

The punchthrough background discussed above was handled in a statistical manner. For example, for the ν_μ charged-current sample, a weight was created for each interacting negative track in the neutral-current and $\bar{\nu}_\mu$ charged-current samples. This weight represented the probability that this track might have left the chamber causing the event to mimic a ν_μ charged-current event. The weight was corrected for those events already lost to the ν_μ charged-current sample. Event distributions were constructed for the $\bar{\nu}_\mu$ charged-current and neutral-current samples using the weights calculated above. One entry was made for each I^- track that could cause the event to be mistaken for a ν_μ charged-current event if it were to leave the chamber. The weighted distributions were created assuming this I^- track was the muon. These weighted background distributions were then subtracted from the ν_μ charged-current event distributions. A similar thing was done to correct the $\bar{\nu}_\mu$ charged-current sample for the punchthrough background.

More specifically, the punchthrough background in the ν_μ charged-current sample was estimated by making weighted distributions of fake events. N fake events were created for each neutral-current or $\bar{\nu}_\mu$ charged-current event with $E_{event}>10$ GeV and with N I^- tracks that passed the $y<0.85$ cut (calculated assuming each I^- track to be the lepton). Only $\bar{\nu}_\mu$

charged-current events with $y_L + < 0.5$ were considered here to lessen the effect of the considerable high-y neutral-current punchthrough in this calculation. Events with high-y had a relatively low μ^+ momentum and there was a significant background from low momentum π^+ tracks that left the chamber in the neutral-current events. The ith fake event was created assuming the ith I^- track to be the lepton. The ith event weight, w_i, was calculated as follows:

$$P_i = e^{-\frac{d_i}{125}} ,$$

$$\bar{P}_i = \prod_{\substack{j=1 \\ j \neq i \\ E_j > E_i}}^{N} \left(1 - e^{-\frac{d_j}{125}}\right) ,$$

$$S_i = \prod_{j=1}^{N} \left(1 - e^{-\frac{d_j}{125}}\right) ,$$

$$\text{and } w_i = \frac{P_i \bar{P}_i}{S_i} .$$

Distributions of these weighted, fake events were subtracted from those of the initial ν_μ charged-current sample.

The punchthrough background for the $\bar{\nu}_\mu$ charged-current sample was estimated in a similar fashion. Here, N fake events

were created for each neutral-current event with $E_{event}>10$ GeV, no L^- tracks, and N I^+ tracks passing the y cut assuming each to be the lepton. W_i for the ith fake event (assuming the ith I^+ track to be the lepton) was calculated as above. For E53B the y cut was 0.85. For E53A it was necessary to use a y cut of 0.5 because of the small signal to background ratio in the $\bar{\nu}_\mu$ sample.

In addition, the $\bar{\nu}_\mu$ charged-current sample was corrected for losses due to punchthrough. The loss to the ν_μ charged-current sample was just the $\bar{\nu}_\mu$ punchthrough contamination of the ν_μ charged-current sample calculated above. The same weighted distributions were added to the original $\bar{\nu}_\mu$ distributions to take into account the loss. The loss to the neutral-current sample occurred when a negative hadron in a good $\bar{\nu}_\mu$ charged-current event left the chamber where y_{L^-} was greater than 0.85. N weighted, fake events (similar to those described above) were created for each $\bar{\nu}_\mu$ charged-current event with $y_{L^+}<0.5$ and with N I^- tracks where $y_{I^-} > 0.85$. Weighted distributions of these events were added to the original $\bar{\nu}_\mu$ charged-current event distributions to correct for this loss. Table II summarizes the punchthrough corrections for the two runs.

After punchthrough correction, the ν_μ and $\bar{\nu}_\mu$ charged-current normalization samples contained 1439 and 92 events, respectively.

Event distributions for the ν_μ charged-current sample are shown as points in figures 13-17. Those for the $\bar{\nu}_\mu$ charged-current samples are shown in figures 18-22.

3.2.3 Corrections

The numbers above were corrected for losses and efficiencies. The corrections are summarized in table III and described in greater detail below. After corrections, the final number of ν_μ charged-current events inside the fiducial volume in the normalization sample was 2252 ± 115. Similarly the number of $\bar{\nu}_\mu$ charged-current events was 135 ± 21. When these numbers were scaled up to represent the entire set of E53 data they became 163700 ± 8800 and 10735 ± 1600, respectively.

The number of events lost due to the $E_\nu > 10$ GeV cut was estimated from the beam Monte Carlo described in Appendix A. For E53A this loss was (7.8 ± 1.2)% for the ν_μ sample and (3.1 ± .5)% for the $\bar{\nu}_\mu$ sample. The comparable numbers for E53B were (5.9 ± .9)% and (3.1 ± .5)%, respectively.

The $y < 0.85$ cut removed (12.5 ± 1.2)% and (5.1 ± .5)% of the ν_μ and $\bar{\nu}_\mu$ charged-current events, respectively. These numbers were estimated from a Monte Carlo that used Buras and Gaemers'

parameterization of the ν_μ and $\bar{\nu}_\mu$ charged-current cross sections with radiative corrections included. This Monte Carlo will be discussed in greater detail later in this chapter.

Finally, the normalization samples were corrected for scanning efficiencies. These efficiencies were 0.85 ± .03 [52] and 0.84 ± .03 [53] for E53A and E53B respectively. These numbers were determined by second scans of portions of the film.

3.3 Results

Having isolated the various ν samples, the next step in the analysis was to test ν_μ-ν_e and $\bar{\nu}_\mu$-$\bar{\nu}_e$ universality. This was done by comparing the cross section, kinematic distributions, charged particle multiplicity, strange particle production rate, and dilepton rate for the $\nu_e(\bar{\nu}_e)$ sample with those for the normalization sample or previously published results for muon neutrinos(antineutrinos).

3.3.1 Cross Sections

In order to determine the cross sections for the ν_e and $\bar{\nu}_e$ charged-current interactions, it was necessary to calculate the ν_e/ν_μ and $\bar{\nu}_e/\nu_\mu$ flux ratios. This was done using the beam Monte Carlo described in Appendix A.

Figures 23a-d and 24a-d show the event energy spectra for the Monte Carlo superimposed on those for the data. The ν_μ Monte Carlo plots are area normalized to the ν_μ data plots. The Monte Carlo plots for the other neutrino types are normalized using the same scale factors that were used for the ν_μ plots for the respective runs. The data have been corrected for missing neutral energy using a simple method determined experimentally in a narrow band beam.[54] This correction, termed the PIK correction in this thesis, is summarized as follows:

$$\text{for } E_{had} < 10 \text{ GeV}, \; E_{had}^{corr} = 1.11E_{had},$$

$$\text{for } 10 \text{ GeV} < E_{had} < 100 \text{ GeV}, \; E_{had}^{corr} = (.003E_{had}+1.05)E_{had},$$

$$\text{and for } E_{had} > 100 \text{ GeV}, \; E_{had}^{corr} = 1.35E_{had}.$$

The average correction to the hadronic energy using the PIK method is 14%.

Two things are immediately striking in figures 23 and 24. The first is that the Monte Carlo ν_μ spectrum agrees very well with the data for both runs. This is an important experimental check on the beam Monte Carlo. The other is that the ν_e and $\bar{\nu}_e$ Monte Carlo spectra are much harder than the data. This is due to electron momentum mismeasurements in the data. This topic is discussed in detail in Appendix B and further on in this chapter.

Normalizing to the muon neutrinos, the beam Monte Carlo predicts the following numbers of events assuming universality:

	Monte Carlo	Data
E53A		
ν_μ normalization sample	1309 ± 196	1309 ± 92
$\bar{\nu}_\mu$ normalization sample	11 ± 2	30 ± 15
ν_e total sample	801 ± 120	789 ± 70
$\bar{\nu}_e$ total sample	59 ± 9	87 ± 15
E53B		
ν_μ normalization sample	943 ± 141	943 ± 69
$\bar{\nu}_\mu$ normalization sample	75 ± 11	105 ± 15
ν_e total sample	1427 ± 214	1300 ± 118
$\bar{\nu}_e$ total sample	270 ± 41	249 ± 30

The actual observed numbers are included for easy comparison.

For E53A, the predicted and observed numbers of $\bar{\nu}_\mu$ events agree within statistics. This is another important experimental check on the beam Monte Carlo. The observed and predicted numbers of ν_e and $\bar{\nu}_e$ events are in agreement, consistent with universality.

For E53B, the reasonable agreement between the observed and predicted $\bar{\nu}_\mu$ events was obtained only after decreasing the horn

focussing efficiency. The horn current during the experiment was 85 kamps. For the numbers shown in the table above the horn current was reduced from 85 kamps to 40 kamps in the Monte Carlo. The $\bar{\nu}_\mu$ rate in the data is significantly higher than the Monte Carlo prediction without this adjustment. Much effort was expended investigating this discrepancy. The conclusion of this study was that something was wrong with the E53B beam. This conclusion was corroborated by another experiment (E531) running in the same ν beam.[61] Both experiments observed anomalies in the relative event rates for the various neutrino types. Decreasing the focussing efficiency in the Monte Carlo effectively took into account some unknown problem with the beam, bringing the $\bar{\nu}_\mu$ rate into closer agreement with the data. When this was done, the ν_e and $\bar{\nu}_e$ rates also agreed with the data, consistent with universality. Because it is impossible to know exactly what was wrong with the beam, the data from E53B were not used for the ν_e and $\bar{\nu}_e$ cross section measurements. It should be noted that the basic shapes of the Monte Carlo ν_e and $\bar{\nu}_e$ energy spectra do not change significantly when the horn current is adjusted. Therefore the data from both runs were used for the kinematic distribution comparison. The other tests of universality presented in this thesis are not dependent on the beam Monte Carlo.

The cross sections for ν_e and $\bar{\nu}_e$ charged-current interactions were calculated using

$$\frac{\sigma_{(\bar{\nu}_e)}}{E} = \left[\frac{\sigma_{\nu_\mu}}{E} \right]_{\substack{\text{world}\\ \text{average}}} \frac{{}^{(\bar{\nu}_e)} \text{ events observed}}{\nu_\mu \text{ events observed}} \; \frac{\int (E)(\nu_\mu \text{ flux})}{\int (E)({}^{(\bar{\nu}_e)} \text{ flux})} \; .$$

Taking σ/E for muon neutrinos to be 0.67×10^{-38} cm^2/GeV [62] gave

$$\sigma_{\nu_e} = (0.66 \pm .12)E \times 10^{-38} \quad \text{cm}^2$$

and

$$\sigma_{\bar{\nu}_e} = (0.51 \pm .12)E \times 10^{-38} \quad \text{cm}^2 \quad .$$

These values are consistent with the comparable values for muon neutrinos and antineutrinos [63] ($0.67E \times 10^{-38}$ cm^2 and $0.34E \times 10^{-38}$ cm^2, respectively).

3.3.2 Kinematic Distributions

As can be seen in figures 23 and 24 for the E_ν spectra, the raw $\nu_e(\bar{\nu}_e)$ kinematic distributions are very different from those that might be expected assuming universality. These dramatic differences are primarily due to the fact that the electron momenta in the $\nu_e(\bar{\nu}_e)$ events are inaccurately reconstructed.

This subject has been studied in some detail and the results are presented in Appendix B. The relevant conclusions drawn in the appendix can be summarized as follows:

i) the effect of hard bremsstrahlung is to cause severe and frequent undermeasurements of the electron momentum;

ii) the true electron momentum can be well approximated by the sum of the reconstructed electron momentum and the momentum of the hardest gamma produced by the primary electron;

iii) gammas emitted by the primary electron tend to convert within a 2.5° cone about the reconstructed electron momentum.

Having completed the EGS study, it was determined that the most direct way to test universality was to correct the electron momentum on an event-by-event basis. The $\nu_e(\bar{\nu}_e)$ event distributions (created using the corrected momenta) could then be compared directly to the $\nu_\mu(\bar{\nu}_\mu)$ distributions. This method was found unworkable with the E53 data. The problem was that the momentum of the hardest converted gamma was also severely undermeasured because it relied on two separate electron measurements.

After this discovery, an alternate method of testing universality using the kinematic distributions was developed. In this method, the data was directly compared to distributions of Monte Carlo events constructed assuming universality and having electron momenta smeared in an appropriate fashion. The electron momenta were smeared using the EGS4/SPFLM package described in Appendix B.

More explicitly, a large number of fake, weighted Monte Carlo events were created to compare to the data. For each generated event, E_ν was picked flat between 0 and 200 GeV and weighted by the $\nu_e(\bar{\nu}_e)$ beam Monte Carlo spectrum described in Appendix A. The kinematic variables (see Appendix C)

$$x = \frac{Q^2}{2M(E_\nu - E_{lep})} \text{ and } y = \frac{E_\nu - E_{lep}}{E_\nu}$$

were picked flat between 0 and 1. Each event was then weighted again by the production cross section, $\sigma(x,y)/E_\nu$, for muon neutrinos (antineutrinos). Having chosen x, y, and E_ν, the magnitude and direction of the 'true' electron momentum was completely specified for each event. This information was then input as the initial condition for the EGS/SPFLM Monte Carlo package which generated and reconstructed an electron shower at a random point within the bubble chamber. This reconstructed or

'measured' electron momentum was then used in place of the true electron momentum as the weighted Monte Carlo distributions were created. These distributions were compared directly to the data as a test of universality.

The production cross section was obtained from the Buras and Gaemers parameterization with radiative corrections. The code to do this was acquired from the CCFR collaboration.[55] Members of that collaboration claim the parameterization fits their data within 10%.

A good check on the validity of this procedure is to use the same method to generate $\nu_\mu(\bar{\nu}_\mu)$ events and compare the Monte Carlo distributions to those obtained using the normalization data. Figures 13-22 show such a comparison for the E_ν, P_μ, E_{had}, x, and y distributions. The Monte Carlo distributions are area normalized to the data. The only difference between the Monte Carlo method used for the $\nu_\mu(\bar{\nu}_\mu)$ and that used for the $\nu_e(\bar{\nu}_e)$ events was that for the $\nu_\mu(\bar{\nu}_\mu)$ distributions the true muon momentum was used. The data is PIK corrected with errors that are statistical only. The error in the Monte Carlo distributions reflect a 15% error in the beam Monte Carlo spectrum, a 10% error in the Buras and Gaemers parameterization, and a 15% uncertainty in the hadronic energy for the data. The one sigma error boundaries are shown for the Monte Carlo distributions.

Kinematic distributions for the ν_e and $\bar{\nu}_e$ events are shown in figures 25-34. Monte Carlo distributions created using the method described above were superimposed on the data after being area normalized to the data. Only those gammas lying outside a 2.5° cone about P_e^{meas} are included in the hadronic energy. In addition to the PIK correction, the hadronic energy in the ν_e data has been increased slightly to reflect the hadronic gamma measurement inefficiency in these events. This inefficiency is demonstrated in figure 35 where linear fits to the gamma energy/event as a function of charged particle W^2 are given for several different samples. Assuming universality, these lines should all be the same as that for the ν_μ sample. Presumably, the increased activity on the film for the ν_e events led to a gamma measurement inefficiency. Maintaining the spirit that the Monte Carlo and data distributions should agree assuming universality, the gamma energy/event in the ν_e events was corrected to be the same as that for the ν_μ sample. This correction was 11% of the hadronic energy for the ν_e events on the average. There were too few $\bar{\nu}_e$ events to use this method effectively; so the error in the hadronic energy was increased to 20% in the Monte Carlo $\bar{\nu}_e$ distributions.

The errors in the Monte Carlo distributions in figures 25-34 include a 15% error in the beam Monte Carlo spectrum, a 10% error

in the Buras and Gaemers parameterization, and a total of 15% to 20% uncertainty in the hadronic energy of the data. The errors on the data points are statistical only and the one sigma error bands are shown for the Monte Carlo.

3.3.3 Neutral Strange Particle Production Rates

A search for neutral strange particle decays yielded 109 vees (56 in E53A and 53 in E53B) in the 1403 ν_e candidates that remained after cuts. A similar search of the 179 $\bar{\nu}_e$ candidates revealed 7 vees. Only those vees passing the χ^2 cut discussed in chapter 2 were considered. In addition, the vees were required to be greater than one cm from the vertex since the scanning efficiency was poor in that region. Also, the vee vertices were required to be greater than 10 cm from any wall to lessen the background from interactions in the walls of the bubble chamber. Finally, the calculated lifetime for each vee was required to be less than six proper lifetimes for that particular particle. To calculate the V° production rate it was necessary to correct the observed number of vees for losses and efficiencies. The appropriate corrections were determined in a previous E53 study of V° production by muon neutrinos. They are discussed in detail in reference (56) and summarized below.

$$N_{corr} = N_{obs}\frac{C_1C_2C_3C_4C_5}{C_6C_7}$$

	E53A	E53B
C_1 = Geometric detection efficiency	1.13 ± .01	1.13 ± .01
C_2 = Interaction before decay	1.16 ± .03	1.16 ± .03
C_3 = Low lifetime loss	1.13 ± .03	1.13 ± .03
C_4 = Slow decay prong	1.04 ± .01	1.04 ± .01
C_5 = Fake fits	0.95 ± .02	0.95 ± .02
C_6 = Random scan efficiency	0.98 ± .02	0.95 ± .02
C_7 = Reconstruction efficiency	0.98 ± .02	0.96 ± .02

The multiplicative correction factors of 1.52 ± .08 for E53A and 1.60 ± .08 for E53B give V° production rates of

$$\frac{\nu_e N \to e^- V^o X}{\nu_e N \to e^- X} = (11.7 \pm 1.2)\% \text{ and } \frac{\bar{\nu}_e N \to e^+ V^o X}{\bar{\nu}_e N \to e^+ X} = (5.2 \pm 2.2)\% .$$

These numbers represent a weighted average for both runs. The error in the number of vees is statistical only. The comparable rates for ν_μ and $\bar{\nu}$-induced events are[57,58]

$$\frac{\nu_\mu N \to \mu^- V^o X}{\nu_\mu N \to \mu^- X} = (9.8 \pm 0.7)\% \text{ and } \frac{\bar{\nu}_\mu N \to \mu^+ V^o X}{\bar{\nu}_\mu N \to \mu^+ X} = (7.3 \pm 0.7)\% .$$

The $\nu_\mu V^o$ rate becomes (10.1 ± 0.7)% after being adjusted to take into account the harder ν_e flux.

3.3.4 Charged Particle Multiplicities

The average charged particle multiplicity as a function of charged particle W^2 is shown in figure 36 for the ν_e sample and the ν_μ normalization sample. The corresponding plot for the antineutrinos is shown in figure 37. The multiplicity is shown as a function of charged particle W^2 because this quantity is independent of any lepton momentum or neutral hadron energy measurement difficulties.

3.3.4 ν_e-induced Charm (Dileptons)

In a further effort to test ν_μ-ν_e universality, a search was conducted for e^-e^+ (dilepton) events in the e^- and e^+ samples. These events are expected to arise from ν_e-induced charm production and decay. A Feynman diagram for this process is shown in figure 11b. Two events consistent with this process have been observed previously; however, no rate has been reported.[72] The background to this process due to close-in Dalitz pairs and gamma conversions is severe. Requiring the candidate events to have high lepton momenta and a large invariant mass for the lepton pair virtually eliminated these backgrounds, leaving a signal consistent with universality.

More explicitly, the electron and positron samples were searched for events with at least one e^+ and one e^- satisfying the following requirements:

inside fiducial volume,

no L^- track,

$P_{e^-} > 5$ GeV,

$P_{e^+} > 1$ GeV,

e^- must satisfy delta cut,

and (invariant mass $e^-e^+)^2 > .16$ GeV^2.

This search yielded a sample of 7 e^-e^+ events.

The remaining background due to Dalitz pairs and gamma conversions was estimated experimentally. This was done by applying the same cuts to the so-called 'Dalitz pair' sample. This sample consisted of 2510 edited and measured e^-e^+ pairs that were thought to be consistent with close-in Dalitz decays or gamma conversions, i.e., they were attached to the vertex and clearly had zero opening angle in all three views. Only one event in the Dalitz pair sample passed the cuts that were required of the e^-e^+ candidates. This places an upper limit on the background remaining in the e^-e^+ sample of $.7 \pm .7$ events.

Table IV lists the momenta of the two leptons in the e^-e^+ candidates. The high e^- momenta and low e^+ momenta are consistent with ν_e-induced charm production. In addition, there is kinematic evidence that the e^-e^+ events are from ν_e-induced charm. Figure 38a gives the angle between the transverse momenta of the hadrons and the electron. Figure 38b shows similar results for the hadrons and the positron, and figure 38c gives that for the electron and the positron. These plots give evidence that the positron is produced in the hadronic sector of the event while the electron is produced apart from the hadronic sector. This is consistent with the hypothesis that these events come from charm production by electron neutrinos.

The number of e^-e^+ events was corrected for losses and efficiencies. These corrections are similar to those discussed in section 3.1.2 and are summarized in table V. The corrected number of e^-e^+ events yields a rate of

$$\frac{\nu_e N \rightarrow e^-e^+X}{\nu_e N \rightarrow e^-X} = (.79 \pm .35)\% \ .$$

This is comparable to the μ^-e^+ rate of [59]

$$\frac{\nu_\mu N \rightarrow \mu^-e^+X}{\nu_\mu N \rightarrow \mu^-X} = (.52 \pm .09)\% \ .$$

There were two neutral strange particles in the 7 e^-e^+ events. Correcting this number for losses and efficiencies as done earlier in this chapter gives a rate of

$$\frac{\nu_e N \to e^- e^+ V^o X}{\nu_e N \to e^- e^+} = (.46 \pm .36)\% ,$$

consistent with the rate for muon neutrinos,[60]

$$\frac{\nu_\mu N \to \mu^- e^+ V^o X}{\nu_\mu N \to \mu^- X} = (.35 \pm .05)\% .$$

This high rate for strange particle production is further evidence that the e^-e^+ events come from charm production.

3.4 Conclusion

In this thesis a number of different tests of ν_μ-ν_e and $\bar{\nu}_\mu$-$\bar{\nu}_e$ universality are described. The ν_e and $\bar{\nu}_e$ samples used for these tests are an order of magnitude larger than those used in any previous high-energy experiment. The precision of tests vary, ranging from 5% to 70%. No significant evidence for a violation of universality is seen. In addition, the first significant observation of a ν_e-induced dilepton signal from charm production is reported.

APPENDIX A: THE BEAM MONTE CARLO

The neutrino beam layout and method of production is described in general terms in Chapter 2. Because the various species of neutrinos in the beam used for this experiment came from different secondary decays, the fluxes had different energy dependences. As described in Chapter 3, a good test of ν_μ-ν_e universality using the E53 data required an understanding of the neutrino fluxes. These fluxes were calculated from a knowledge of the secondary production at the target and an understanding of how the secondaries propagated through the beamline and decayed.

The Monte Carlo used for this work was based on a neutrino beam Monte Carlo written by C. Baltay. Numerous modifications were made to this code, the most significant of which was the installation of a new K/π production spectrum. The formula for the new production spectrum was taken from a Fermilab publication by Malensek (FN-341, 2941.000, (1981)). It is an empirical formula for thick target particle production based on a fit utilizing the data of Atherton et al. (CERN 80:07, (1980)). This data consists of measurements of secondaries from proton-beryllium collisions at 400 GeV/c for target lengths of 10, 30, and 50 cm. The parameterization given by Malensek is

$$\frac{d^2N}{dPd\Omega} = \frac{f(L)}{f(500)} BX \frac{(1-X)^A (1+5e^{-DX})}{(1 + \frac{P_t^2}{M^2})^4} ,$$

$$\text{where } X = \frac{\text{momentum of produced particle}}{\text{energy of primary protons}} ,$$

and A, B, M, and D are constants. The values of these constants given by Malensek follow:

	π^+	π^-	K^+	K^-
A	3.598	4.122	2.924	6.107
B	177.2	70.60	14.15	12.33
M^2	.7077	.8932	1.164	1.098
D	27.00	11.29	19.89	17.78 .

f(L) is a function that changes the parameterization for different target lengths.

$$f(L) = \frac{e^{-\frac{L}{\lambda(s)}} - e^{-\frac{L}{\lambda(p)}}}{(1 - \frac{\lambda(p)}{\lambda(s)})}$$

$\lambda(s)$ is the absorption cross section for the produced secondaries and $\lambda(p)$ is the absorption cross section for protons. The parameterization can be adjusted for different target materials by using measurements by Eichten et al. (Nucl Phys B44, 333, (1972)). For a given X and secondary type, the production

formula output is scaled by the measured secondary production for the different material divided by that for Be as given by a linear fit to the data of Eichten et al.

Atherton et al. have estimated their measurement errors to be 8%. The errors for the K measurements and the π measurements are roughly the same. There is a disagreement of less than 11% between the data of Atherton et al. and Malensek's formula after correcting for the different target materials and lengths used in E53. Eichten et al. estimate the errors in their reported production ratios to be 4%. Adding these errors in quadrature gives an overall error in the particle production of 15%. This was the dominant error in the beam Monte Carlo calculations used in this thesis.

Fourteen different decay modes of secondaries were allowed to take place during a calculation. These modes along with the relative fluxes for the E53A calculation follow:

$\pi^+ \rightarrow \nu_\mu \mu^+$	100
$\pi^- \rightarrow \bar{\nu}_\mu \mu^-$	1.06
$K^+ \rightarrow \nu_\mu \mu^+$	6.31
$K^- \rightarrow \bar{\nu}_\mu \mu^-$	8.3×10^{-2}
$K_L^\circ \rightarrow \pi^- \mu^+ \nu_\mu$	7.5×10^{-2}

$K_L^o \rightarrow \pi^+\mu^-\bar{\nu}_\mu$	7.5×10^{-2}
$K_L^o \rightarrow \pi^-e^+\nu_e$	10.1×10^{-2}
$K_L^o \rightarrow \pi^+e^-\bar{\nu}_e$	8.8×10^{-2}
$K^+ \rightarrow \pi^o\mu^+\nu_\mu$	2.8×10^{-2}
$K^- \rightarrow \pi^o\mu^-\bar{\nu}_\mu$	4.4×10^{-3}
$K^+ \rightarrow \pi^o e^+\nu_e$	4.2×10^{-1}
$K^- \rightarrow \pi^o e^-\bar{\nu}_e$	6.6×10^{-3}

$\pi^+ \rightarrow \mu^+ \rightarrow e^+\nu_e\bar{\nu}_\mu$	ν_e	1.0×10^{-1}	$\bar{\nu}_\mu$	9.5×10^{-2}
$\pi^- \rightarrow \mu^- \rightarrow e^-\bar{\nu}_e\nu_\mu$	$\bar{\nu}_e$	7×10^{-4}	$\bar{\nu}_\mu$	5×10^{-4}

The overall flux and event ratios for both the E53A and E53B calculations are given below. As stated above, there is a 15% error in each of the relative rates.

	ν_μ : $\bar{\nu}_\mu$: ν_e : $\bar{\nu}_e$
E53A flux ratios:	100 : 1.24 : 0.59 : 0.09
E53A event ratios:	100 : 0.82 : 0.95 : 0.07
E53B flux ratios:	100 : 13.9 : 1.06 : 0.43
E53B event ratios:	100 : 8.03 : 1.84 : 0.34

APPENDIX B: ELECTRON MOMENTUM RECONSTRUCTION

In a wide band neutrino beam the incident neutrino energy for each event is not well-known and must be ascertained from the energy visible in the detector. Because of this, a meaningful test of ν_μ-ν_e universality using the data from E53 requires that the electron momentum reconstruction be well understood. This is difficult in a heavy liquid because of radiative processes. The general expression for the probability of a particle undergoing bremsstrahlung goes as $1/\text{mass}^2$. So, bremsstrahlung is negligible for all the particles dealt with in this analysis except electrons. For electrons moving through a heavy liquid, this process causes frequent and significant changes in the electron momentum. Thus, reconstructing the electron momentum by curvature often gives inaccurate results.

This problem was examined in detail by studying Monte Carlo simulations of electron interactions in the 15-foot bubble chamber. The events were generated using the Electron-Gamma Shower (EGS4) package from SLAC.[64] This system of computer code is a general purpose package for modeling the coupled transport of electrons and photons in an arbitrary geometry. The EGS4 system can simulate the transport of particles with energies

from a few keV to several TeV through any element, compound, or mixture. It takes into account hard bremsstrahlung, positron annihilation, Moliere scattering, Møller scattering, Bhabha scattering, continuous energy loss (both soft bremsstrahlung and collision loss), pair production, Compton scattering, Rayleigh scattering, and the photoelectric effect.

The general procedure for this study began by initiating a Monte Carlo electron shower with an appropriate position, angle, and energy within a volume of liquid hydrogen or a mixture of neon and hydrogen. Only the primary electron and those photons produced by processes involving the primary electron were transported. The Monte Carlo propagated photons and charged particles with energies between 600 MeV and 200 GeV. The volume in which the shower was generated corresponded to that of the 15-foot bubble chamber at Fermilab. A vertical magnetic field was present within the volume. The magnitude of this field at different points corresponded to the field present in the bubble chamber during the acquisition of data for E53. Propagation was terminated for all particles passing outside the bubble chamber. Transport of the primary electron was stopped after it turned through an angle of ninety degrees. The position of the initial point and twenty-nine successive, evenly spaced points along the primary track were recorded for further study. These points were

distributed along the entire available length of the track. Prior to recording this information, the three coordinates of each point were smeared by 150 microns to simulate the scanner setting error during measurement. Each photon produced by the primary electron was followed until it converted inside or left the chamber. The positions and energies of all conversions inside the chamber were saved.

The three dimensional information about each of the thirty points along the primary electron track was given as input to a computer program called SPFLM.[65] This program took the three coordinates of each point and constructed three sets of two dimensional coordinates corresponding to the position of the point on each of the three film planes in the cameras used for this experiment. This information was formatted by SPFLM so that it could be used as input to the track reconstruction program TVGP. After processing through TVGP, the 'true' electron momentum (input to EGS), the reconstructed electron momentum (output from TVGP), and the positions and energies of all converted gammas (output from EGS) were available for analysis.

It was important to establish the degree of accuracy with which SPFLM projected three dimensional points onto the three film planes. To do this, several bubble chamber fiducial

markings were measured and processed through TVGP. The reconstructed three dimensional coordinates of these points were then run through SPFLM and TVGP. The values given by SPFLM/TVGP agreed with those coming straight out of TVGP to better than one millimeter.[66] This is large enough to cause some loss of momentum resolution for smooth well-behaved tracks like those formed by muons or pions. However, for electron tracks, the radiative processes make this error negligible.

One test that was made to be sure the EGS/SPFLM system was performing as intended involved generating showers in liquid hydrogen and comparing the reconstructed momentum with the momentum given as input to EGS. The showers were generated in hydrogen to reduce the effect of bremsstrahlung. The pion hypothesis coming out of TVGP was used for this comparison to avoid the soft bremsstrahlung corrections made by TVGP during electron reconstruction. Figure 39 shows the reconstructed momentum for the 5 GeV electrons that did not emit a gamma. The mean momentum of this distribution is 5.2 GeV. The fact that this momentum is slightly higher than 5.0 GeV is expected since TVGP corrected for dE/dX loss in NeH_2 rather than H_2. The momentum resolution (sigma/sqrt(p)) for this distribution is 4%.

Another check was to duplicate results from an electron test beam run in the 15-foot bubble chamber at Fermilab in 1981.[67] For this experiment, the bubble chamber was filled with a neon-hydrogen mixture and exposed to a 19 GeV beam of electrons. Harigel et al. measured a number of electrons in this beam along with most of the converted gammas in each event. The momentum reconstruction method used for this work was exactly the same as that used for E53. Their results showed that electron momentum measurements coming out of TVGP were consistently low due to hard bremsstrahlung. However, they found that they were able to correct these measurements by summing the reconstructed electron momentum and the momentum of all gammas lying within a 1.2° cone about the reconstructed electron momentum. The EGS/SPFLM Monte Carlo duplicated this result only after assuming the electron passed through 10 centimeters of the neon-hydrogen fill prior to the start of the measurement. These results are shown in figure 40. Inspection of the data used for the analysis by Harigel et al. revealed that in fact, the measurements did not begin until the electron was about 10 centimeters into the cone at the front of the chamber. This was due to the fact that the beam test was performed at the end of a neutrino run. The cameras were not set up to take photographs of tracks at the very front of the cone where the electrons entered the chamber.

G. Harigel et al. also examined 50 GeV electrons in the

15-ft bubble chamber. Although they did not have the statistics to say something quantitative, their results agree qualitatively with those from the EGS/SPFLM Monte Carlo.[68]

After these checks, the EGS/SPFLM package was used to explore the question of how to best correct inaccurate electron momenta. To do this, two or three hundred events were generated in a neon-hydrogen (64 atomic percent neon) mixture at each of 5 different energies. Electrons of the appropriate energy initiated showers at random points within the fiducial volume of the bubble chamber. Figures 41a-e show the reconstructed electron momenta for these events. These histograms vividly demonstrate the effect of hard bremsstrahlung on the momentum reconstruction. The momentum coming out of TVGP is consistently low, ranging from zero to the actual electron momentum.

The electron momentum distributions change dramatically as the momenta of converted gammas falling within a cone about the reconstructed electron are included. This is shown in figures 42 and 43 for cone opening angles of 0.6° and 2.4° for 40 GeV electrons. At small angles the energy of most events approximate the correct value. However there is a class of events that remain uncorrected. These electrons experience a catastrophic bremsstrahlung fairly early in the shower development. As shown

in figures 44 and 46, the energy of the largest gamma is high and the multiplicity is low for these events. The magnitude of the reconstructed momentum is very low and the reconstructed angle is inaccurate. Because the angle reconstruction is far from the true direction, only insignificant gammas are included for cones with small opening angles. As the opening angle of the cone is increased, the energetic gamma is finally added in and the electron momenta of these events become reasonable.

For cones with large angles, another problem becomes apparent; the momentum of many events is overcorrected. The scatterplots in figures 45 and 47 give some indication of what is happening in these events. These electrons tend to emit many small photons as they lose energy. The initial momentum reconstruction is fairly good and the proper energy for these events is obtained by using a cone with a small opening angle. As the angle is increased and more gamma momentum is included, the electron momentum is overcorrected.

A good, energy independent method of electron momentum correction was found by simply adding the momentum of the hardest converted gamma to the reconstructed electron momentum. The beauty of this method becomes apparent when the two extreme types of electron events described above are considered. For events

with an early energetic catastrophic bremsstrahlung, the initial reconstructed momentum is very low and the hardest converted gamma has a large momentum. The sum of these two momenta gives approximately the correct energy. For events where the electron emits many relatively low energy photons, the reconstructed electron momentum is fairly close to the correct value. The hardest converted gamma contains only a small amount of energy. Once again the sum gives a value close to that desired. Figures 48a-e give the corrected electron momentum for electrons at different energies using this method.

The EGS/SPFLM package was also used to study other aspects of electron showers in NeH_2. Figures 49a-c give the gamma multiplicity distributions at various energies. The average gamma multiplicity ranges from 4 at 10 GeV to 11 at 100 GeV. It is important to note that these distributions represent only those gammas emitted by the primary electron. There are many other converted gammas visible on the scan table such as gammas emitted by other converted gammas and gammas from π^o decays. Some of these might be mistaken for gammas from the primary electron. Figures 50a-c show the gamma multiplicity as a function of opening angle about the reconstructed electron at different energies. An angle of 2.5^o includes most of the gammas from the primary electron at all energies. This fact can

be used to separate the gammas from the primary electron from the gammas from other sources.

In summary, the EGS/SPFLM Monte Carlo demonstrates that the momentum of electrons passing through a heavy liquid can be successfully reconstructed in an energy independent manner. The procedure for doing this is to sum the reconstructed electron momentum and the momentum of the hardest gamma produced by the primary electron. Also, the average gamma multiplicity for these events ranges from 4 to 11. Finally, an angular cut of 2.5° about the reconstructed electron can help isolate those gammas emitted by the primary electron from those created by other sources.

APPENDIX C: KINEMATICS

Throughout this thesis a number of kinematic variables are used to describe the processes of interest. Figure 51 illustrates deep-inelastic lepton-nucleon scattering.[71] Referring to this figure, E is the energy of the incident lepton (a neutrino or antineutrino in this thesis). E′ is the energy of the outgoing lepton. Q is the 4-momentum transfer to the nucleon. M is the mass of the nucleon. W, E^*, and $\mathbf{P}^*$ are the mass, energy, and 3-momentum of the hadronic system, respectively. Letting ν=E-E′, the following quantities can be defined:

$$x = \frac{Q^2}{2M\nu} = \frac{2E_\nu E_{lepton}(1-\cos\theta)}{2M\nu}$$

$$\text{and} \quad y = \frac{\nu}{E} = \frac{E-E'}{E} \quad ,$$

where θ is the lab angle between the incoming neutrino and the outgoing lepton. y is the fraction of the lepton's energy lost in the lab. At high energies, it is just the fraction of the hadronic energy in the final state. x is a measure of the degree of inelasticity of the interaction. A value of one corresponds to an elastic interaction. In the parton model, x is the fraction of the target nucleon's momentum carried by the struck quark.

REFERENCES

1. See C. Quigg, **Gauge Theories of the Strong, Weak, and Electromagnetic Interactions**, Benjamin Cummings, 1983, and references therein.

2. Cheng and Li, **Gauge Theory of Elementary Particle Physics**, Oxford University Press, 1984.

   C. Quigg, **Gauge Theories of the Strong, Weak, and Electromagnetic Interactions**, Benjamin Cummings, 1983.

   F. Halzen and A. Martin, **Quarks and Leptons: An Introductory Course in Modern Particle Physics**, Wiley, 1984.

   M.A.B. Beg(and A. Sirlin, Ann. Rev. Nucl. Sci. 24 (1974) 252.

3. A. Savoy-Navarro, Phys. Rep. 105, Nos 1 and 2 (1984) 91.

4. R. Barbieri, Nucl. Phys. B269 (1986) 253.

   R. Barbieri et al., Phys. Lett. 156B, 348 (1985).

5. S.M. Bilenky and S.T. Petcov, Rev. Mod. Phys. 59 (1987) 671.

6. N.J. Baker et al., Phys. Rev. Lett. 47, 1576 (1981).

7. C.N. Leung, Phys. Rev. D28, 2205 (1983).

   M. Gronau, C.N. Leung, and J.L. Rosner, Phys. Rev. D29 2539 (1984).

8. P. Ramond, Nucl. Phys. B110 (1976) 214.

F. Gursey, P. Ramond, and P. Sikivie, Phys. Lett. 60B, 177 (1976).

T.G. Rizzo, Phys. Rev. D34, 1438 (1986).

9. J.D. Bjorken and C.H.L. Smith, Phys. Rev. D7, 887 (1973).

C. W. Kim and J. Kim, Phys. Lett. 79B, 278 (1978).

10. See S.R. Mishra et al., Phys. Rev. Lett. 59, 1397 (1987) and references therein as well as

C. Albajar et al., Phys. Lett. B185, 241 (1987).

H. Yoshida et al., Phys. Rev. Lett. 59, 2915 (1987).

11. S. Dimopoulos and J. Ellis, Nucl. Phys. B182 (1981) 505.

12. R.N. Cahn and H. Harari, Nucl. Phys. B176 (1980) 135.

13. K. Enqvist, K. Mursula, and M. Roos, Z. Phys. C21, 133 (1983).

J. Maalampi, K. Mursula, and M. Roos, Nucl. Phys. B207 (1982) 233.

K. Enqvist and J. Maalampi, Nucl. Phys. B191 (1981) 189.

14. F. Scheck, Phys. Rep. 44, No. 4 (1978) 187.

15. J. Calmet et al., Rev. Mod. Phys., 49 (1977) 21.

16. J. Bailey et al., Phys. Lett. 67B, 225 (1977).

17. D.E. Casperon et al., Phys. Rev. Lett.38, 956 (1977) and 38, 1504 (1977).

18. R.D. Ehrlich et al., Phys. Rev. A5 (1972) 2357.

S.J. Brodsky and G. W. Erickson, Phys Rev. 148 (1966) 26.

19. F. Scheck, Phys. Rep. 44, No. 4 (1978) 187.

20. J.L. Vuilleumier et al., Z. Phys. A278, 109 (1976).

21. S.J. Brodsky and S.D. Drell, Ann. Rev. Nucl. Sci. 20, 147(1970).

22. R.W. Ellsworth et al., Phys. Rev. 165 (1968) 1449.

L. Camilleri et al., Phys. Rev. Lett. 23, 153 (1969).

T.J. Braunstein et al., Phys. Rev. D6 (1972) 106.

23. D.P. Barber et al., Phys. Rev. Lett. 43 (1979) 1915.

24. T. Kinoshita, Phys. Rev. Lett. 2, 477 (1959).

W.J. Marciano and A. Sirlin, Phys. Rev. Lett. 36 (1976) 1425.

25. D.A. Bryman et al., Phys. Rev. Lett. 50 (1983) 7.

26. C. Albajar et al., Phys. Lett. 185B (1987) 233.

A.G. Clark, presented at Neutrino '86, Sendai, Japan, June 3-8 1986.

27. D. Amidei et al., Phys. Rev. D37 (1988) 1750.

S. Abachi et al., Phys. Rev. Lett. 59, (1987) 2519.

H.R. Band et al., Phys. Rev. Lett. 59, (1987) 415.

28. Y. Tsai, Phys. Rev. D4 (1971) 2821.

29. M. Klein, Fortschr. Phys. 33 (1985) 375.

30. B. Narkosa, presented at the 1983 International Lepton/Photon Symp., Cornell University.

31. M. Jonker et al., Phys. Lett. 96B (1980) 435.

H. Abramowicz et al., Z. Phys. C13 (1982) 179.

32. M.E. Duffy et al., Phys. Rev. Lett. 52 (1984) 1865.

W. Droge et al., Nucl. Phys. B273 (1986) 253.

33. J.V. Allaby et al., CERN-EP/86-125, 1986.

34. C. Quigg, **Gauge Theories of the Strong, Weak, and Electromagnetic Interactions**, Benjamin Cummings, 1983, p. 178.

35. J. Blietschau et al., Nucl. Phys. B133 (1978) 205.

36. O. Erriquez et al., Phys. Lett. 102B (1981) 73.

37. H.C. Ballagh et al., Phys. Lett. 79B (1978) 320.

38. Some of the information and figures presented here that concern the experimental setup have been taken from previous theses. See

A.C. Shaffer, III, Ph.D. Thesis, Columbia University (1985).

M.F. Bregman, Ph.D. Thesis, Columbia University (1984).

E.E. Schmidt, Jr., Ph.D. Thesis, Columbia University (1978).

M.S. Hibbs, Ph.D. Thesis, Columbia University (1981).

39. B. Rossi, **High-Energy Particles**, Prentice-Hall, 1952, p.61.

40. B. Rossi, **High-Energy Particles**, Prentice-Hall, 1952, p.14.

41. TVGP and SQUAW were originally written by the Alvarez group at Berkeley. See F.T. Solmitz et al., LRL Alvarez Group Programming Note P-117 (1966). For details on adaptation for use with the 15-ft bubble chamber see E.E. Schmidt, Jr., Ph.D. Thesis, Columbia University (1978).

42. This method was developed by C. Baltay and A.M. Cnops, 1976, internal memo.

43. MKDST was originally written by M. Kalelkar.

44. X. Li and E. Ma, Phys. Rev. Lett. 47 (1981) 1788.

E. Ma et al., Phys. Rev. Lett. 60 (1988) 495.

45. A.C. Shaffer, III, Ph.D. Thesis, Columbia University (1985).

46. C. Baltay, E53 Internal Memo.

47. C. Baltay, E53 Internal Memo.

B. Rossi, **High-Energy Particles**, Prentice-Hall, 1952.

48. A.C. Shaffer, III, Ph.D. Thesis, Columbia University (1985).

49. E.E. Schmidt, Jr., Ph.D. Thesis, Columbia University (1978).

50. A.C. Shaffer, III, Ph.D. Thesis, Columbia University (1985).

51. E.E. Schmidt, Jr., Ph.D. Thesis, Columbia University (1978).

52. M.S. Hibbs, Ph.D. Thesis, Columbia University (1981).

53. A.C. Shaffer, III, Ph.D. Thesis, Columbia University (1985).

54. J. Liu, Ph.D. Thesis, Columbia University (1985).

P. Igo-Kemenes, E53 Internal Memo.

55. C. Foudas, M. Shaevitz, and E. Oltman, (CCFR Collaboration) Private Communication.

A. Buras and K.J.F. Gaemers, Nucl. Phys. B132 (1978) 249.

A. Buras, Nucl. Phys. B125 (1977) 125.

A. De Rujula et al., Nucl. Phys. B154 (1979) 394.

56. N.J. Baker et al., Phys. Rev. D34, 1251 (1986).

57. N.J. Baker et al., Phys. Rev. D34, 1251 (1986).

58. S.J. Barish, presented at Neutrino '79, Bergen, 1979.

59. N.J. Baker et al., Phys. Rev. D32, 531 (1985).

60. N.J. Baker et al., Phys. Rev. D32, 531 (1985).

61. S. Fredrickson at Ohio State, Private Communication.

62. M. Aguilar-Benitez et al., "Review of Particle Properties," Phys. Lett. 170B, 1976.

63. M. Aguilar-Benitez et al., "Review of Particle Properties," Phys. Lett. 170B, 1976.

64. W.R. Nelson, H. Hirayama, and D.W.O. Rogers, SLAC-Report-265, 1985.

65. SPFLM was acquired from M. Kalelkar at Rutgers and Mike Jones at Hawaii.

66. M. Kalelkar, E53 Internal memo.

67. G. Harigel, C. Baltay, and M. Hibbs, NIM 211 (1983) 343.

68. G. Harigel, Private Communication, 1988.

69. In addition to the experiments reviewed in detail here there has been a recent report on ν_e-ν_μ universality by the SKAT collaboration at Serpukhov, USSR. They report on 83 ν_e events with $3 < E_\nu < 30$ GeV. No violation of universality is reported. See V.V. Ammosov et al., Proc. of the 13th International Conference on Neutrino Physics and Astrophysics, Boston, 1988.

70. William A. Orance, Ph.D. Thesis, Columbia University, 1979.

71. D.H. Perkins, **Introduction to High Energy Physics**, Addison-Wesley, 1982.

72. H.C. Ballagh et al., Phys. Rev. D24, 7 (1981).

ACKNOWLEDGEMENTS

As I finish this thesis, I feel that one stage of my life is coming to an end and another is beginning. This thesis represents the culmination of years of training for me; and there are many people to whom I owe my gratitude for their help along the way. I have chosen to broaden these acknowledgements beyond my thesis project because this thesis represents more than a single project to me.

I would like to thank the many professors and friends at Pfeiffer College whose efforts and support helped make my years there both pleasant and productive. I will always cherish the memories of my time spent there.

Throughout my career at Columbia, two people were always there to guide me through the bureaucratic maze. Without the help of Simah Kraus and Metta Smalls I would probably still be standing in front of Pupin trying to figure out how to register for my first semester of courses! I appreciate their efforts.

I spent most of my graduate career at Columbia University's Nevis Laboratory in Irvington, NY. This was truly a wonderful

place to work. I believe that much of the credit for this belongs to the Nevis staff. I could write pages and pages if I were to list all the little projects and personal crises that members of the Nevis staff helped me through. I would like to collectively thank the Nevis staff for all of their efforts on my behalf. In addition, I would like to give special thank you's to Lubo Kral, Ed Anderson, and Ralph Gardner for taking care of me in the shop, Dorothy Palmer for handling all the money details and brightening each day with her smile and disposition, Anne Therrien for a hundred little things, Bob Peters for his local know-how and advice, C.Y. Chi for his help with the computer facilities, and Don Bunch for his help with the computer facilities and well ... for being Don Bunch. I would also like to express my gratitude to Chris Nobile and Dick Barbee. Their expertise and opinions greatly facilitated my thesis project; and they were always willing to stop what they were doing in order to assist me.

A large project like this requires the dedication of many people over many years. I would like to take this opportunity to thank the Fermilab accelerator and 15-ft bubble chamber staffs as well as the scanners and technicians who worked on this project at Brookhaven National Laboratory, Rutgers University, and Columbia University. Their work made my work possible. I would

also be remiss not to thank my collaborators Steve Kahn, Michael Murtagh, Mohan Kalelkar, Eric Hyatt, and Rob Steiner. Their technical help and moral support were invaluable. Also, I appreciate the efforts of the people who helped edit my thesis, Charlie Baltay, Anne Therrien, Gert Harigel, and Sylvia Manly.

In addition to my thesis experiment, I spent some time working on projects for the SLD experiment at Stanford. I would like to thank Richard DuBois, Steve Smith, and Ed Taylor for their help on these projects.

The people I have to thank most for giving me the training for which I came to Columbia are Mike Shaevitz and Charlie Baltay. Mike was always available to help me with any physics question. In fact, even at the busiest of times he seemed to enjoy helping me. His love for physics is infectious. Charlie was my thesis advisor. He gave me the opportunity and freedom to pursue this project and worked closely with me hashing out the details at the end. His ability to immediately grasp the essence of a problem has never ceased to amaze me. I have the greatest respect for these two men. I hope in the last few years I have assimilated just some fraction of their competence, love for life, and love for physics.

Last but not least, I would like to express my gratitude to my family (including my in-laws) for their unfailing love and support through the years. And of course, my deepest thanks goes to my best friend and wife, Sylvia. Things would have been much tougher without her always being there for me.

LIST OF TABLES

I. ν_e and $\bar{\nu}_e$ acceptance corrections and efficiencies

II. ν_μ and $\bar{\nu}_\mu$ punchthrough corrections

III. ν_μ and $\bar{\nu}_\mu$ acceptance corrections and efficiencies

IV. ν_e-induced dilepton momenta

V. e^-e^+ acceptance corrections and efficiencies

TABLE I

ν_e and $\bar{\nu}_e$ Acceptance Corrections and Efficiencies

E53A:	ν_e	$\bar{\nu}_e$
C_1 = Delta	1.006 ± .006	none
$C_2 = P_e > 2 \frac{GeV}{c}$	1.06 ± .01	1.06 ± .01
$C_3 = L^-$	none	1.25 ± .05
C_4 = Splat	1.10 ± .05	1.10 ± .05
C_5 = Scan efficiency	0.84 ± .05	0.84 ± .05
$C_6 = e^+e^-$ ID efficiency	0.98 ± .02	0.98 ± .02
E53B:		
C_1 = Delta	1.006 ± .006	none
$C_2 = P_e > 2 \frac{GeV}{c}$	1.06 ± .01	1.06 ± .01
$C_3 = L^-$	none	1.25 ± .03
C_4 = Splat	1.10 ± .05	1.10 ± .05
C_5 = Scan efficiency	0.77 ± .05	0.77 ± .05
$C_6 = e^+e^-$ ID efficiency	0.98 ± .02	0.98 ± .02

$$N_{corr} = \frac{C_1C_2C_3C_4}{C_5C_6} N_{obs}$$

E53A ν_e N_{corr} = (1.42 ± .11)(556 ± 24) = 789 ± 70

$\bar{\nu}_e$ N_{corr} = (1.77 ± .16)(49 ± 7) = 87 ± 15

E53B ν_e N_{corr} = (1.55 ± .13)(839 ± 29) = 1300 ± 118

$\bar{\nu}_e$ N_{corr} = (1.93 ± .16)(129 ± 11) = 249 ± 30

TABLE II

ν_μ and $\bar{\nu}_\mu$ Punchthrough Corrections

	Uncorr	NC→ν_μ	NC→$\bar{\nu}_\mu$	$\bar{\nu}_\mu$→ν_μ	$\bar{\nu}_\mu$→NC	Corr
E53A:						
ν_μ (y<0.85)	863	-27.8		-.73		834
$\bar{\nu}_\mu$ (y<0.50)	17		-4.3		+5.5	18
NC (y>0.85)	258					
E53B:						
ν_μ (y<0.85)	638	-32.4		-.99		605
$\bar{\nu}_\mu$ (y<0.85)	82		-22.2	+.99	+13.6	74
NC (y>0.85)	241					

TABLE III

ν_μ and $\bar{\nu}_\mu$ Acceptance Corrections and Efficiencies

	ν_μ	$\bar{\nu}_\mu$
E53A:		
$C_1 = E_\nu > 10$ GeV	1.078 ± .012	1.031 ± .005
$C_2 = y < 0.85$ for ν_μ	1.125 ± .012	none
$y < 0.5$ for $\bar{\nu}_\mu$	none	1.244 ± .024
C_3 = Splat	1.10 ± .05	1.10 ± .05
C_4 = Scan efficiency	0.85 ± .03	0.85 ± .03
E53B:		
$C_1 = E_\nu > 10$ GeV	1.059 ± .009	1.031 ± .005
$C_2 = y < 0.85$	1.125 ± .012	1.051 ± .005
C_3 = Splat	1.10 ± .05	1.10 ± .05
C_4 = Scan efficiency	0.84 ± .03	0.84 ± .03

$$N_{corr} = \frac{C_1 C_2 C_3}{C_4} N_{obs}$$

E53A ν_μ $N_{corr} = (1.57 \pm .09)(834 \pm 34) = 1309 \pm 92$

$\bar{\nu}_\mu$ $N_{corr} = (1.66 \pm .10)(18 \pm 9) = 30 \pm 15$

E53B ν_μ $N_{corr} = (1.56 \pm .09)(605 \pm 27) = 943 \pm 69$

$\bar{\nu}_\mu$ $N_{corr} = (1.42 \pm .08)(74 \pm 10) = 105 \pm 15$

TABLE IV

e^-e^+ Event Listing

Roll	Frame	P_{e^-} in GeV/c	P_{e^+} in GeV/c
1044	834	15.0	1.0
1054	586	20.0	14.0
1055	282	28.6	3.7
1316	463	21.1	4.5
2094	6	22.2	7.5
2096	1329	73.4	1.3
2204	1790	6.6	1.2

TABLE V

e^-e^+ Acceptance Corrections and Efficiencies

C_1 = Delta cut	1.01 ± .005
$C_2 = P_{e^-} > 5$ GeV	1.17 ± .03
$C_3 = P_{e^+} > 1$ GeV	1.19 ± .03
$C_4 = L^-$	1.25 ± .05
C_5 = Splat	1.10 ± .05
C_6 = (Invariant Mass)$^2 < .16$ GeV^2	1.08 ± .02
C_7 = Scan efficiency	0.80 ± .05
$C_8 = e^-$ ID efficiency	0.98 ± .02
$C_9 = e^+$ ID efficiency	0.96 ± .02

$$N_{corr} = \frac{C_1C_2C_3C_4C_5C_6}{C_7C_8C_9} N_{obs}$$

$$N_{corr} = (2.77 \pm .27)(6.3 \pm 2.7) = 17.4 \pm 7.6$$

LIST OF FIGURES

1. Experimental layout of E53A and E53B.

2. E53A horns.

3. E53B horn.

4. 15-ft bubble chamber.

5. Illustration of bubble chamber pressure cycle and beam spill.

6. Electron signatures.

7. Photograph of an E53B event with an electron.

8. Photograph of an E53B event with an electron.

9. Feynman diagram of a ν_e charged-current event.

10. Feynman diagram of a $\bar{\nu}_e$ charged-current event.

11. a. Feynman diagram of a ν_μ-induced dilepton ($\mu^- e^+$) event.
    b. Feynman diagram of a ν_e-induced dilepton ($e^- e^+$) event.

12. Feynman diagram of a ν_μ charged-current event.

13. E_ν, ν_μ data (points) - Monte Carlo (outline), Monte

Carlo uses the Buras and Gaemers parameterization.

14. $|P_\mu|$, ν_μ data (points) - Monte Carlo (outline).

15. E_{had}, ν_μ data (points) - Monte Carlo (outline).

16. x, ν_μ data (points) - Monte Carlo (outline).

17. y, ν_μ data (points) - Monte Carlo (outline).

18. E_ν, $\bar{\nu}_\mu$ data (points) - Monte Carlo (outline), Monte Carlo uses the Buras and Gaemers parameterization.

19. $|P_\mu|$, $\bar{\nu}_\mu$ data (points) - Monte Carlo (outline).

20. E_{had}, $\bar{\nu}_\mu$ data (points) - Monte Carlo (outline).

21. x, $\bar{\nu}_\mu$ data (points) - Monte Carlo (outline).

22. y, $\bar{\nu}_\mu$ data (points) - Monte Carlo (outline).

23. a. E53A E_ν, ν_μ data (solid) - beam Monte Carlo (dashed).
    b. E53A E_ν, $\bar{\nu}_\mu$ data (solid) - beam Monte Carlo (dashed).
    c. E53A E_ν, ν_e data (solid) - beam Monte Carlo (dashed).
    d. E53A E_ν, $\bar{\nu}_e$ data (solid) - beam Monte Carlo (dashed).

24. a. E53B E_ν, ν_μ data (solid) - beam Monte Carlo (dashed).
    b. E53B E_ν, $\bar{\nu}_\mu$ data (solid) - beam Monte Carlo (dashed).
    c. E53B E_ν, ν_e data (solid) - beam Monte Carlo (dashed).
    d. E53B E_ν, $\bar{\nu}_e$ data (solid) - beam Monte Carlo (dashed).

25. E_ν, ν_e data (points) - Monte Carlo (outline).

26. $|P_e|$, ν_e data (points) - Monte Carlo (outline).

27. E_{had}, ν_e data (points) - Monte Carlo (outline).

28. x, ν_e data (points) - Monte Carlo (outline).

29. y, ν_e data (points) - Monte Carlo (outline).

30. E_ν, $\bar{\nu}_e$ data (points) - Monte Carlo (outline).

31. $|P_e|$, $\bar{\nu}_e$ data (points) - Monte Carlo (outline).

32. E_{had}, $\bar{\nu}_e$ data (points) - Monte Carlo (outline).

33. x, $\bar{\nu}_e$ data (points) - Monte Carlo (outline).

34. y, $\bar{\nu}_e$ data (points) - Monte Carlo (outline).

35. (Average γ + neutron star energy)/event as a function of the square of the invariant mass of the charged hadrons.

36. ν_μ and ν_e charged particle multiplicities as a function of the square of the invariant mass of the charged hadrons.

37. $\bar{\nu}_\mu$ and $\bar{\nu}_e$ charged particle multiplicities as a function of the square of the invariant mass of the charged hadrons.

38. a. Angle between the transverse momenta of the e^- and the charged hadrons in the e^-e^+ events.
    b. Angle between the transverse momenta of the e^+ and

the charged hadrons in the e^-e^+ events.

c. Angle between the transverse momenta of the e^- and the e^+ in the e^-e^+ events.

39. EGS/SPFLM Monte Carlo, $|P_{TVGP}|$ for 5 GeV electrons in H_2.

40. EGS/SPFLM Monte Carlo, $|P_{TVGP}|$+gamma energy as a function of the opening angle of the 'gamma energy' cone about the reconstructed electron momentum for 20 GeV electrons in NeH_2. The Monte Carlo measurement begins after the electron passes through 10 cm NeH_2.

41. EGS/SPFLM Monte Carlo

a. $|P_{TVGP}|$ for 10 GeV showers in NeH_2.
b. $|P_{TVGP}|$ for 20 GeV showers in NeH_2.
c. $|P_{TVGP}|$ for 40 GeV showers in NeH_2.
d. $|P_{TVGP}|$ for 70 GeV showers in NeH_2.
e. $|P_{TVGP}|$ for 100 GeV showers in NeH_2.

42. EGS/SPFLM Monte Carlo, 40 GeV showers in NeH_2, $|P_{TVGP}|$+gamma energy for cone of 0.6°.

43. EGS/SPFLM Monte Carlo, 40 GeV showers in NeH_2, $|P_{TVGP}|$+gamma energy for cone of 2.4°.

44. EGS/SPFLM Monte Carlo, 40 GeV showers in NeH_2, energy of the most energetic gamma per shower vs. $|P_{TVGP}|$+gamma energy for cone of 0.6°.

45. EGS/SPFLM Monte Carlo, 40 GeV showers in NeH_2, energy of the most energetic gamma per shower vs. $|P_{TVGP}|$+gamma energy for cone of 2.4°.

46. EGS/SPFLM Monte Carlo, 40 GeV showers in NeH_2, gamma multiplicity per shower vs. $|P_{TVGP}|$+gamma energy for cone of 0.6°.

47. EGS/SPFLM Monte Carlo, 40 GeV showers in NeH_2, gamma multiplicity per shower vs. $|P_{TVGP}|$+gamma energy for cone of 2.4°.

48. EGS/SPFLM Monte Carlo, $|P_{TVGP}|$ + energy for the hardest gamma for electron showers in NeH_2.
    a. 10 Gev.
    b. 20 GeV.
    c. 40 GeV.
    d. 70 GeV.
    e. 100 GeV.

49. EGS/SPFLM Monte Carlo, gamma multiplicity per shower.
    a. 10 GeV.
    b. 40 GeV.
    c. 100 GeV.

50. EGS/SPFLM Monte Carlo, gamma multiplicity as a funtion of opening angle of cone about the reconstructed electron momentum.
    a. 10 GeV.
    b. 40 GeV.
    c. 100 GeV.

51. Deep-inelastic neutrino-nucleon scattering.

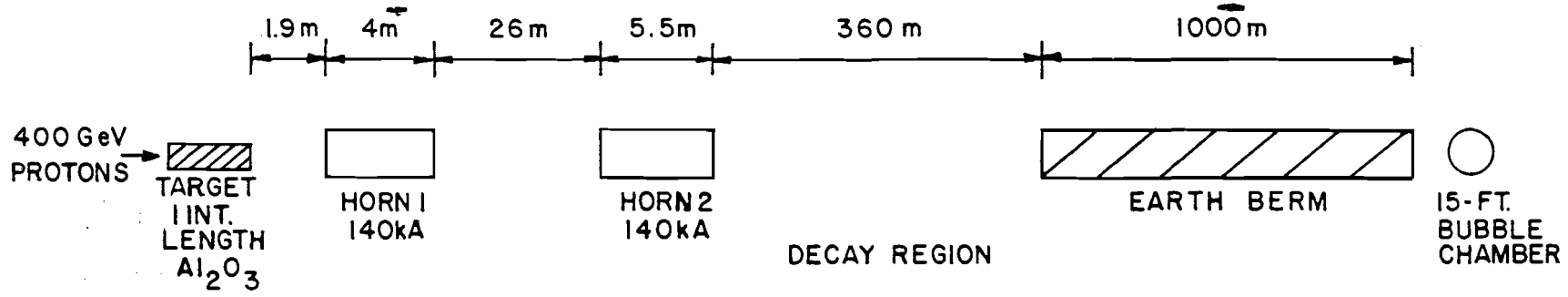

E53A BEAMLINE

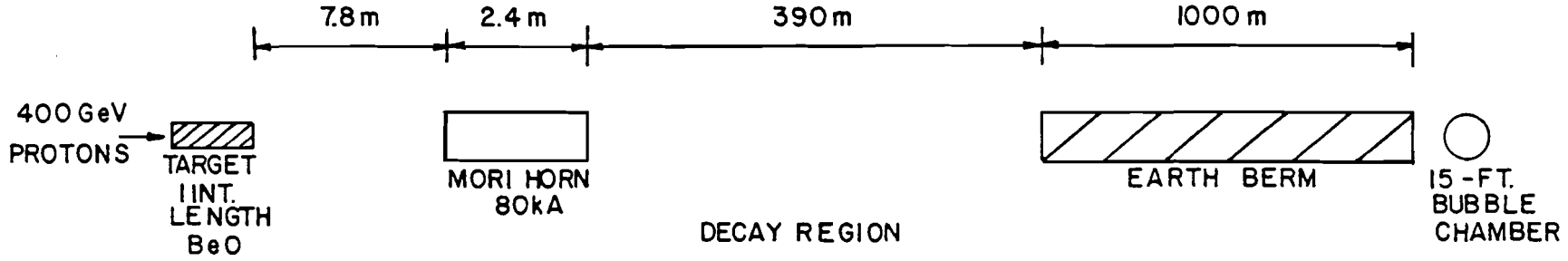

E53B BEAMLINE

Figure 1.

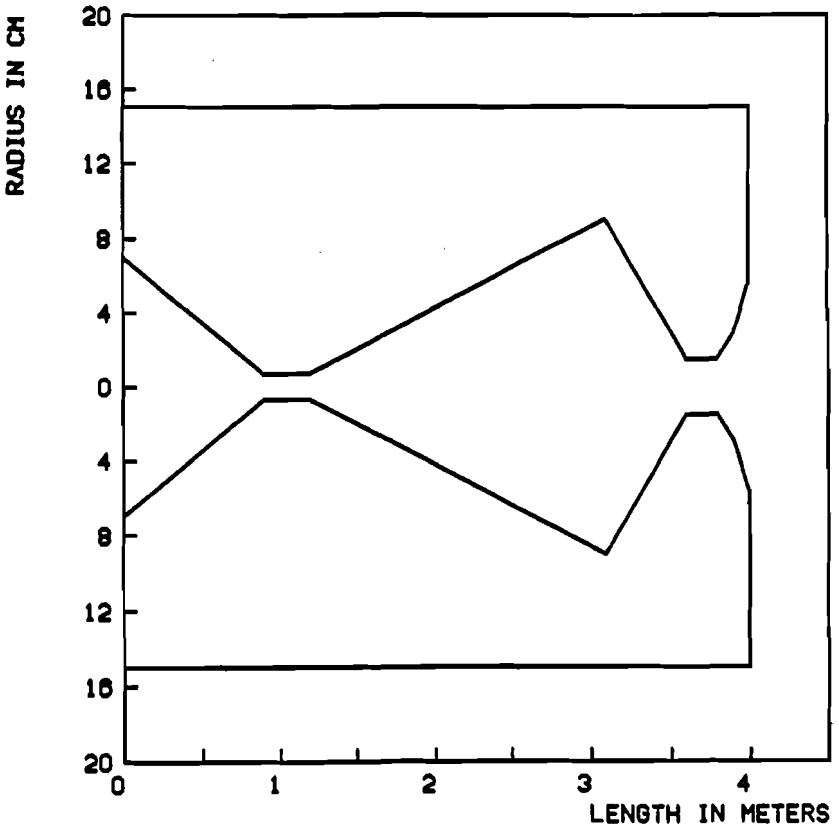

E53A, HØRN 1

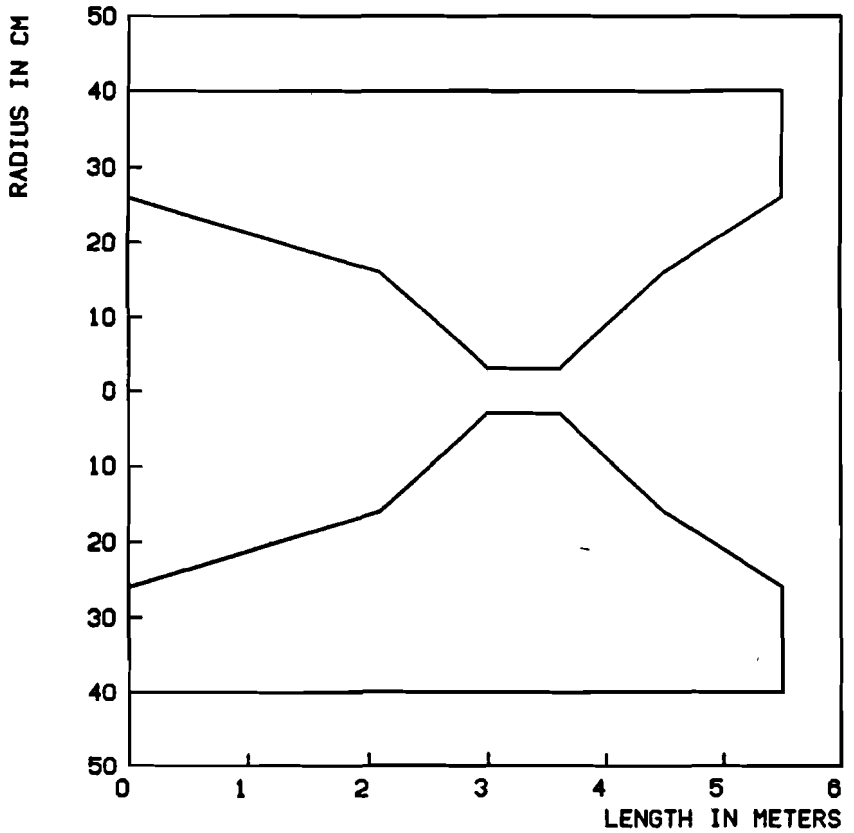

E53A, HØRN 2

Figure 2.

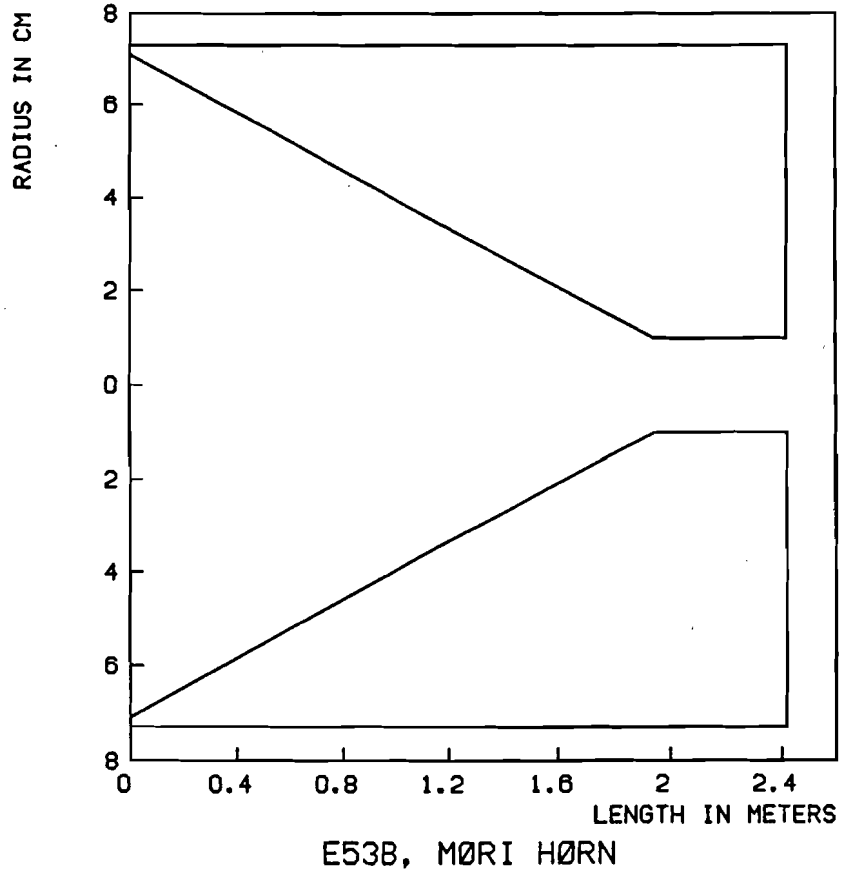

Figure 3.

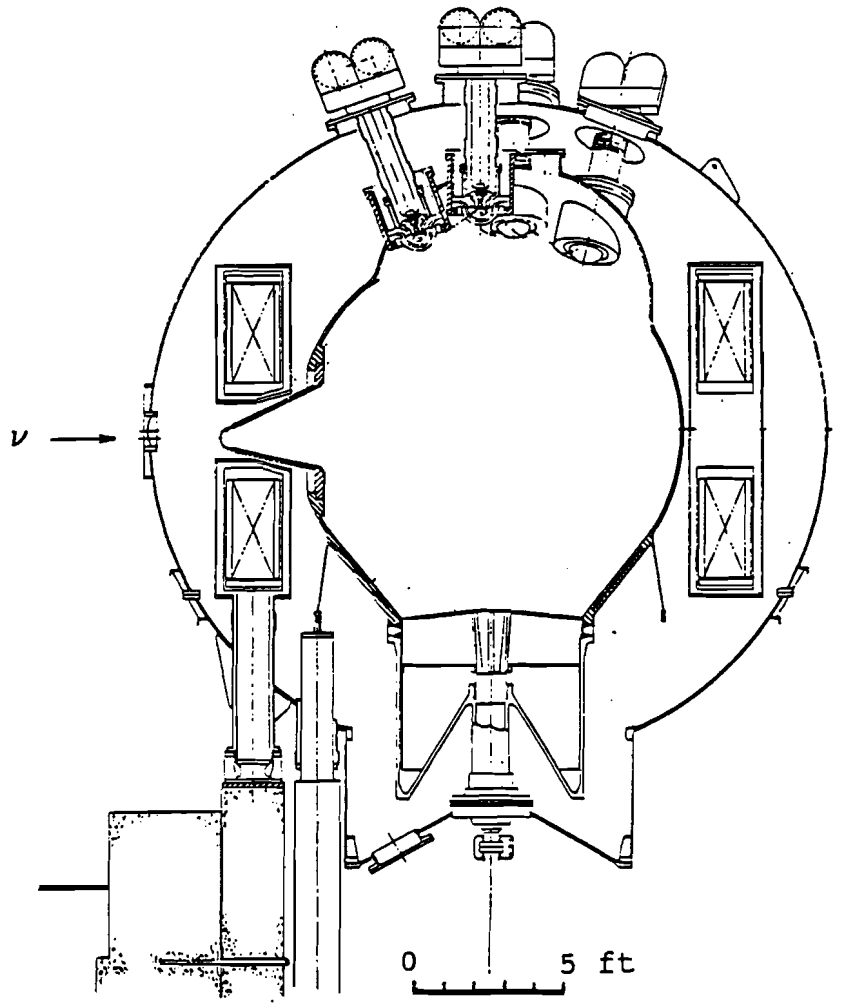

Figure 4.

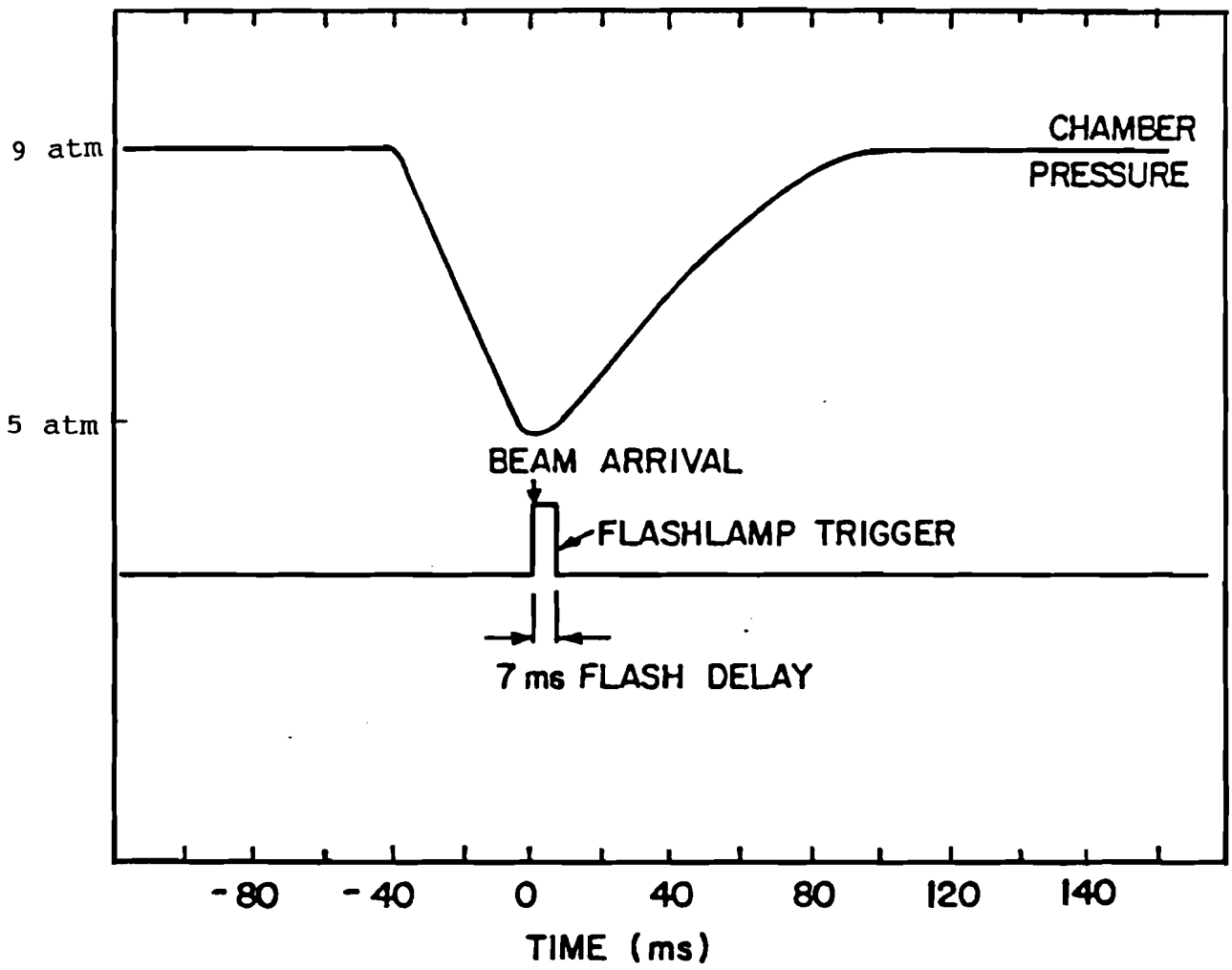
9 atm
5 atm
CHAMBER
PRESSURE
BEAM ARRIVAL
FLASHLAMP TRIGGER
7 ms FLASH DELAY
-80
-40
0
40
80
120
140
TIME (ms)

Figure 5.

ELECTRON SIGNATURES

a) Spiralization

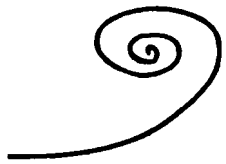

b) Sudden change in curvature (possibly with converted gamma)

c) Delta ray comparable in energy to electron

d) Annihilation (positron only)

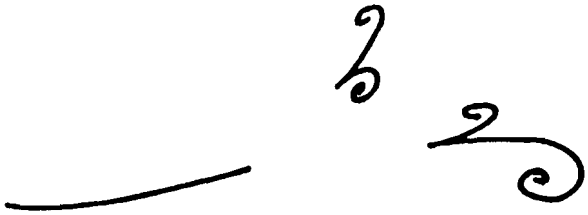

e) Combination

Figure 6.

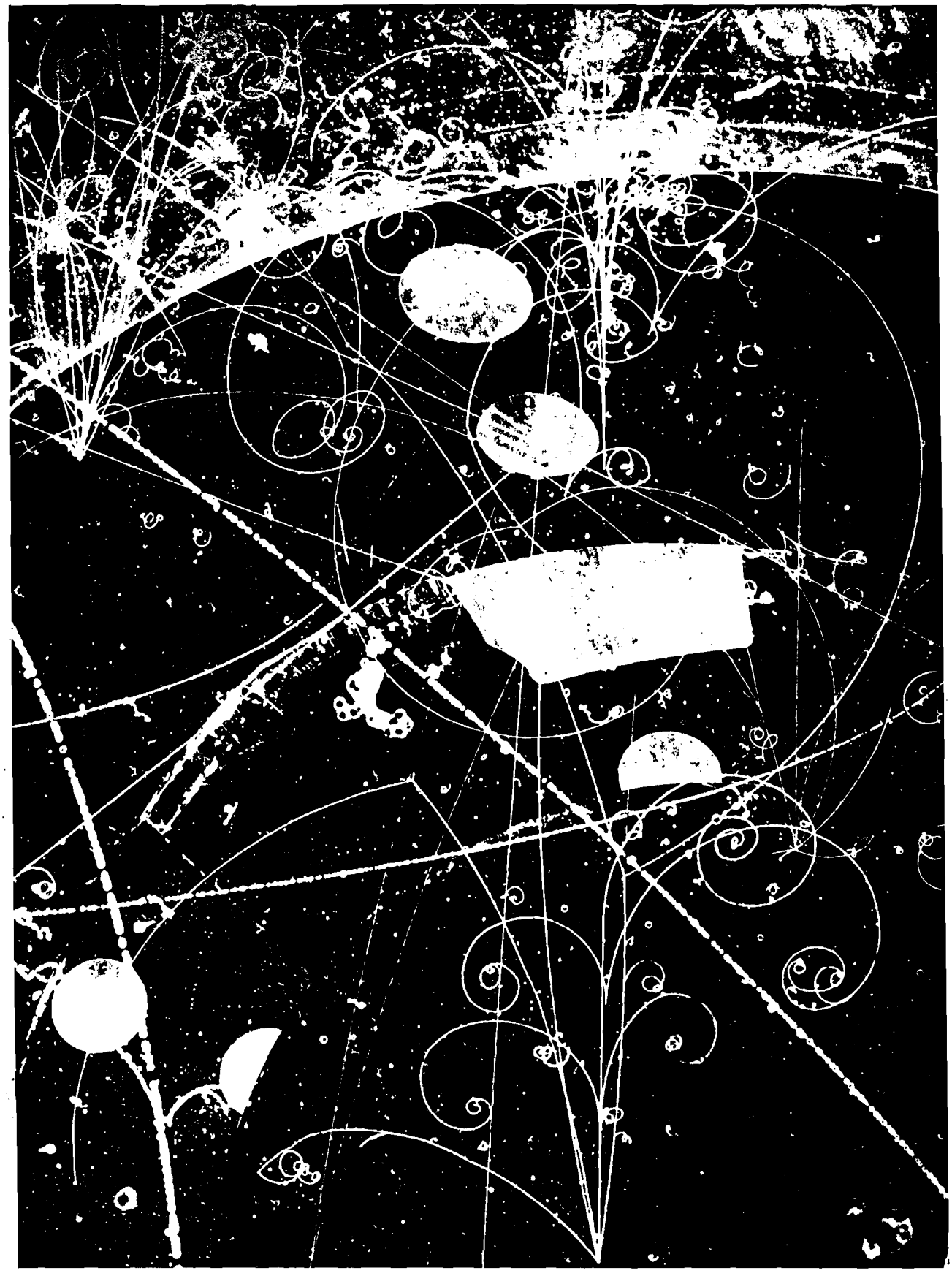

Figure 7.

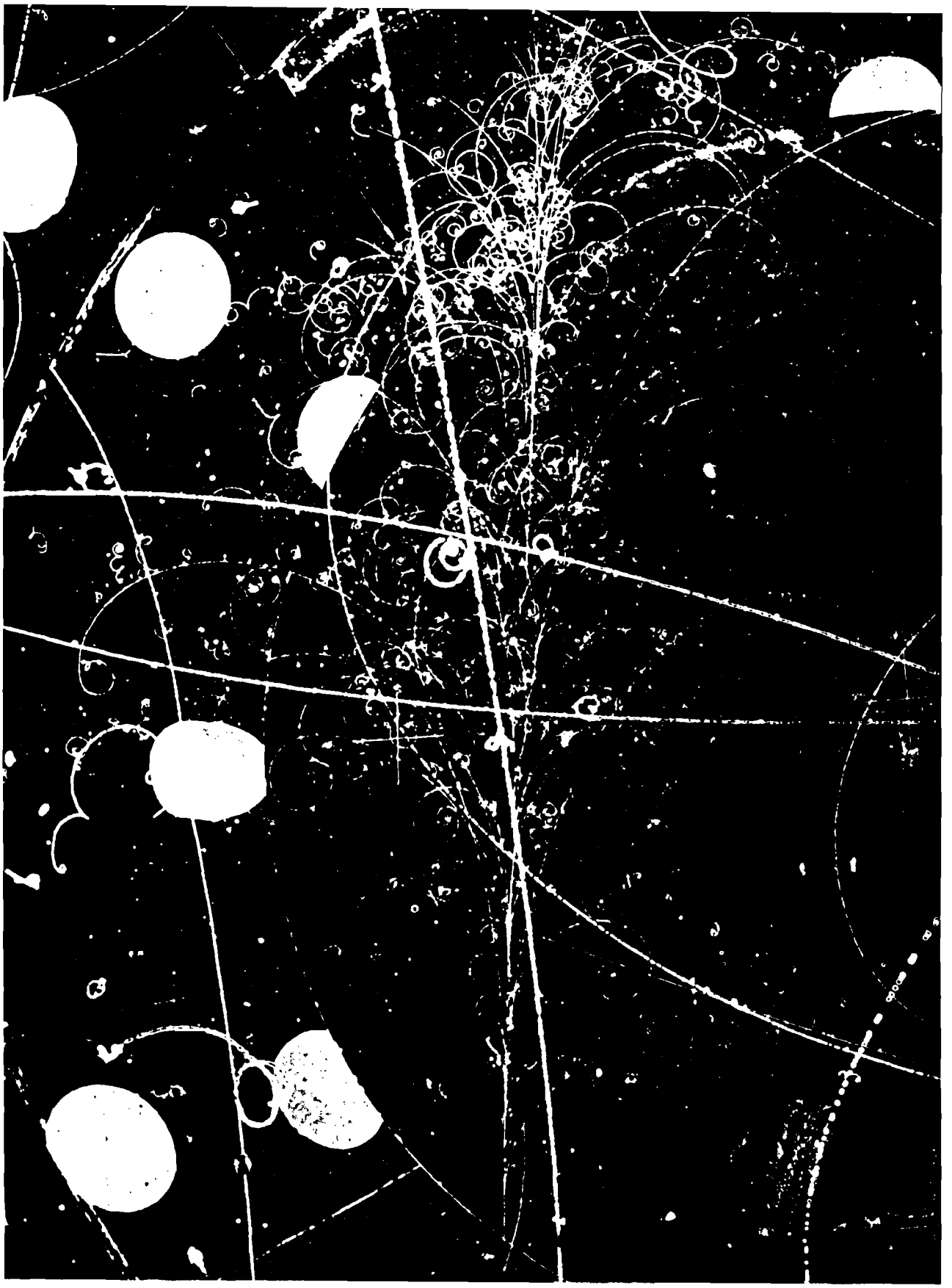

Figure 8.

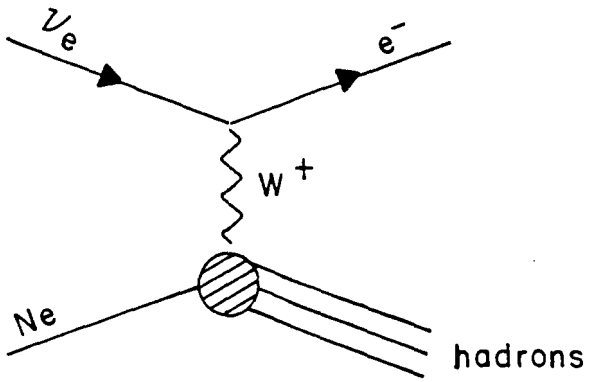

Figure 9.

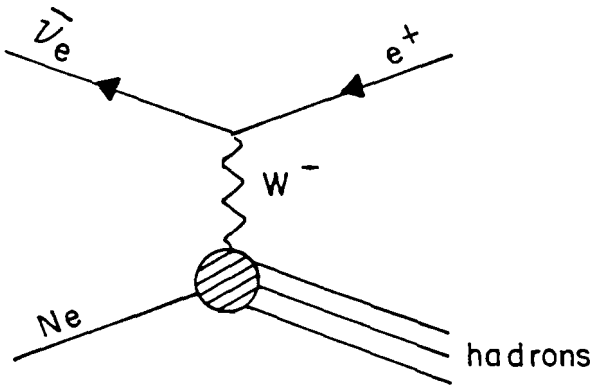

Figure 10.

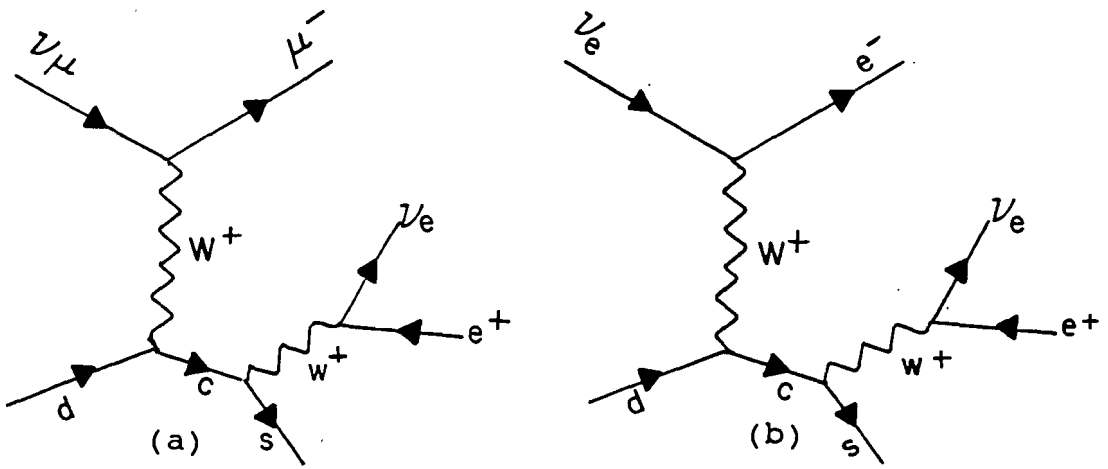

Figure 11.

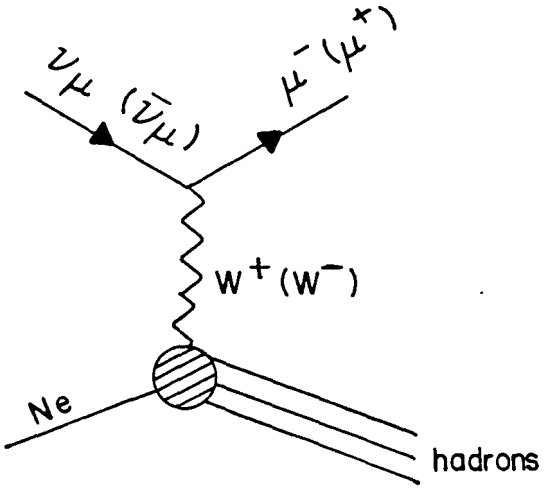

Figure 12.

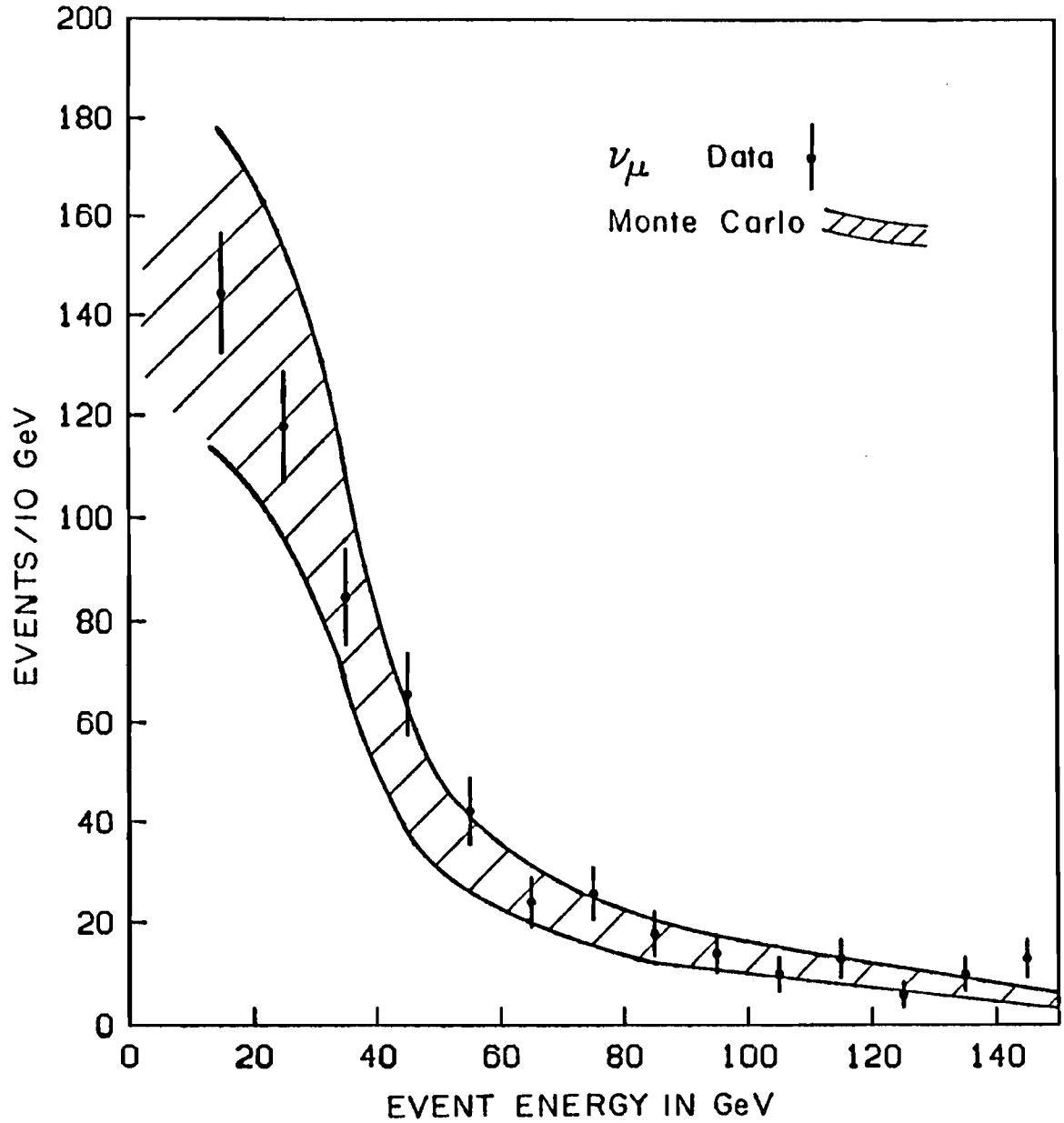
200
180
160
140
120
100
80
60
40
20
0
EVENTS/10 GeV
0
20
40
60
80
100
120
140
EVENT ENERGY IN GeV
ν_μ Data
Monte Carlo

Figure 13.

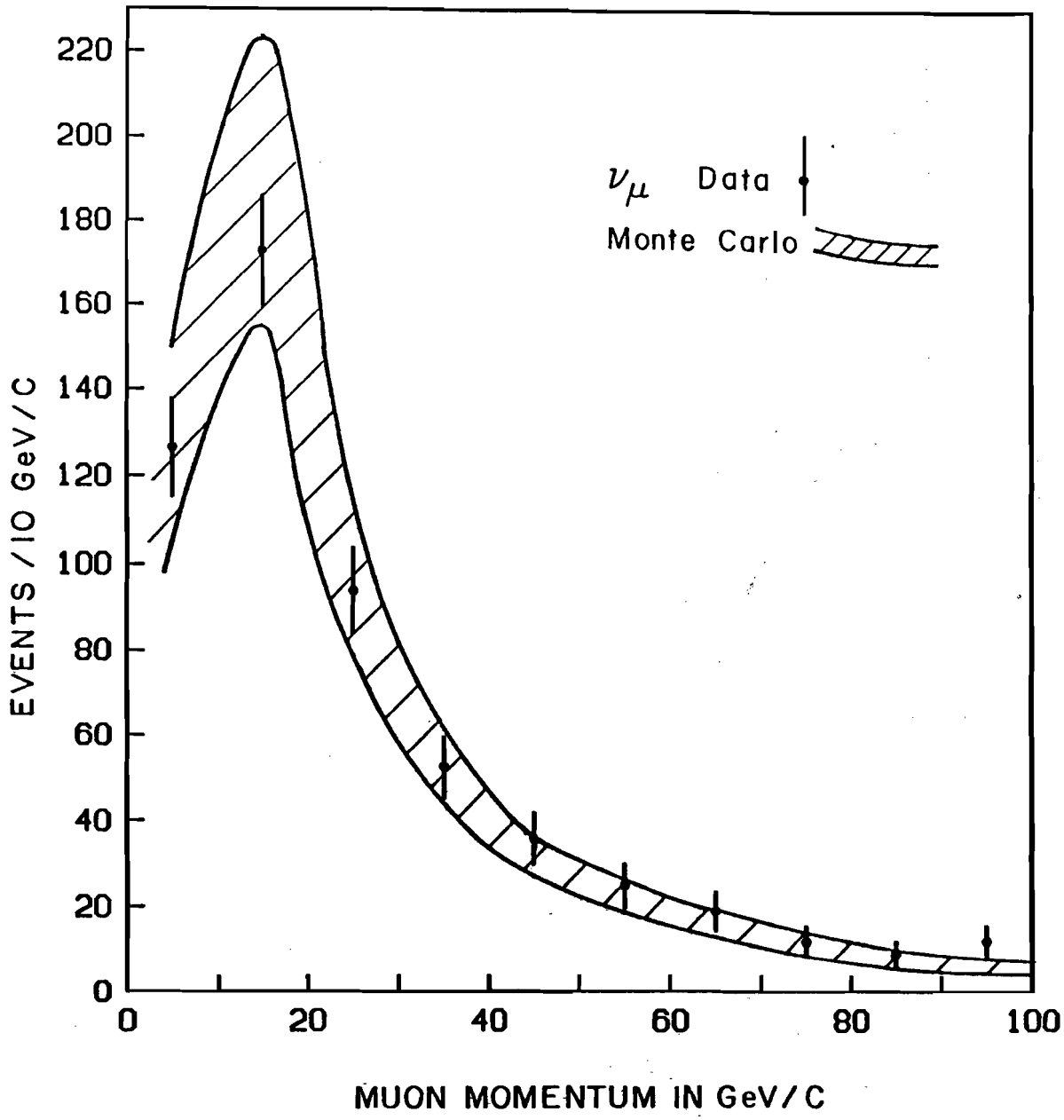
220
200
180
160
140
120
100
80
60
40
20
0
EVENTS / 10 GeV / C
0
20
40
60
80
100
MUON MOMENTUM IN GeV / C
ν_μ Data
Monte Carlo

Figure 14.

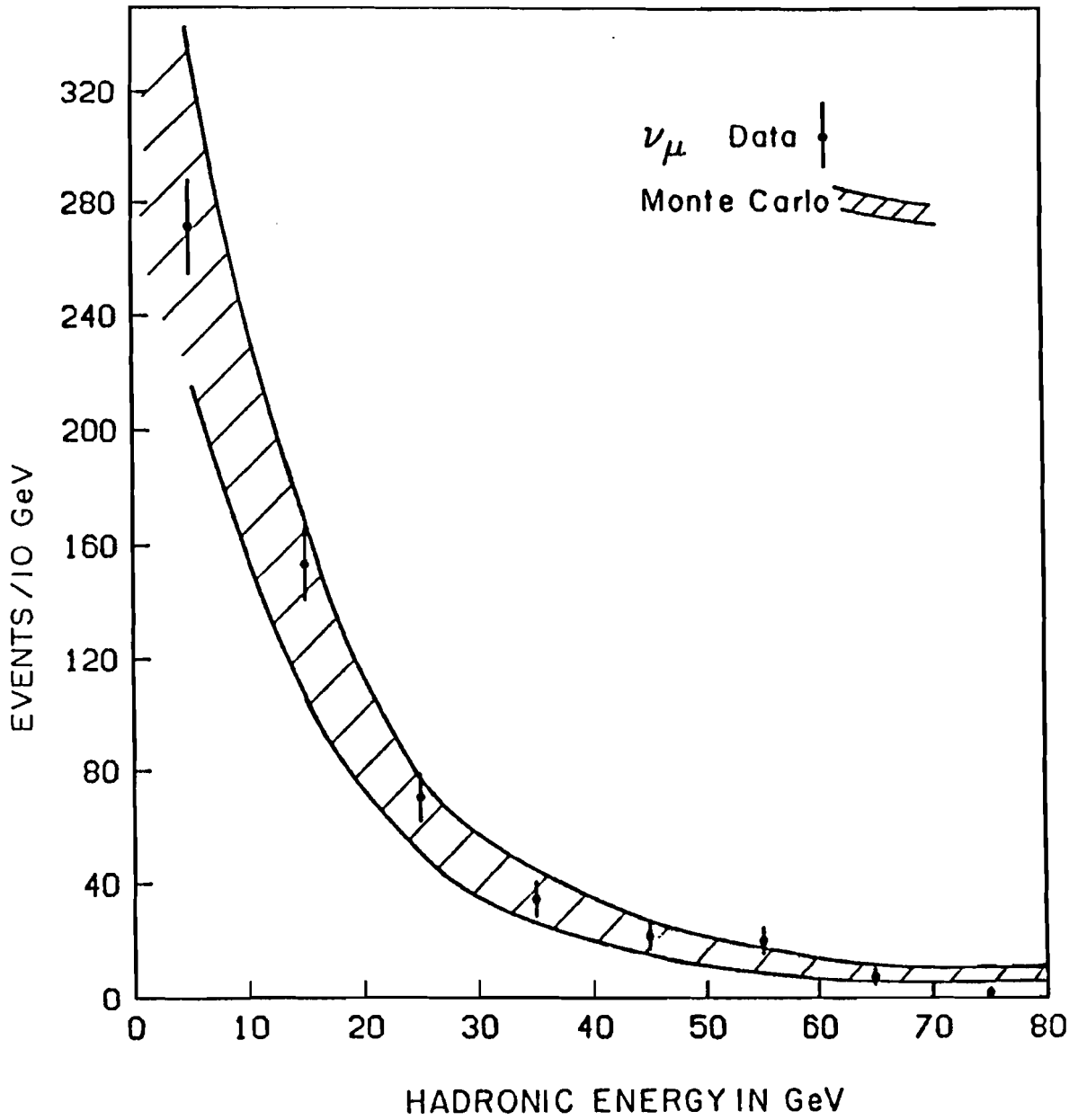
ν_μ Data
Monte Carlo
EVENTS /10 GeV
0
40
80
120
160
200
240
280
320
0
10
20
30
40
50
60
70
80
HADRONIC ENERGY IN GeV

Figure 15.

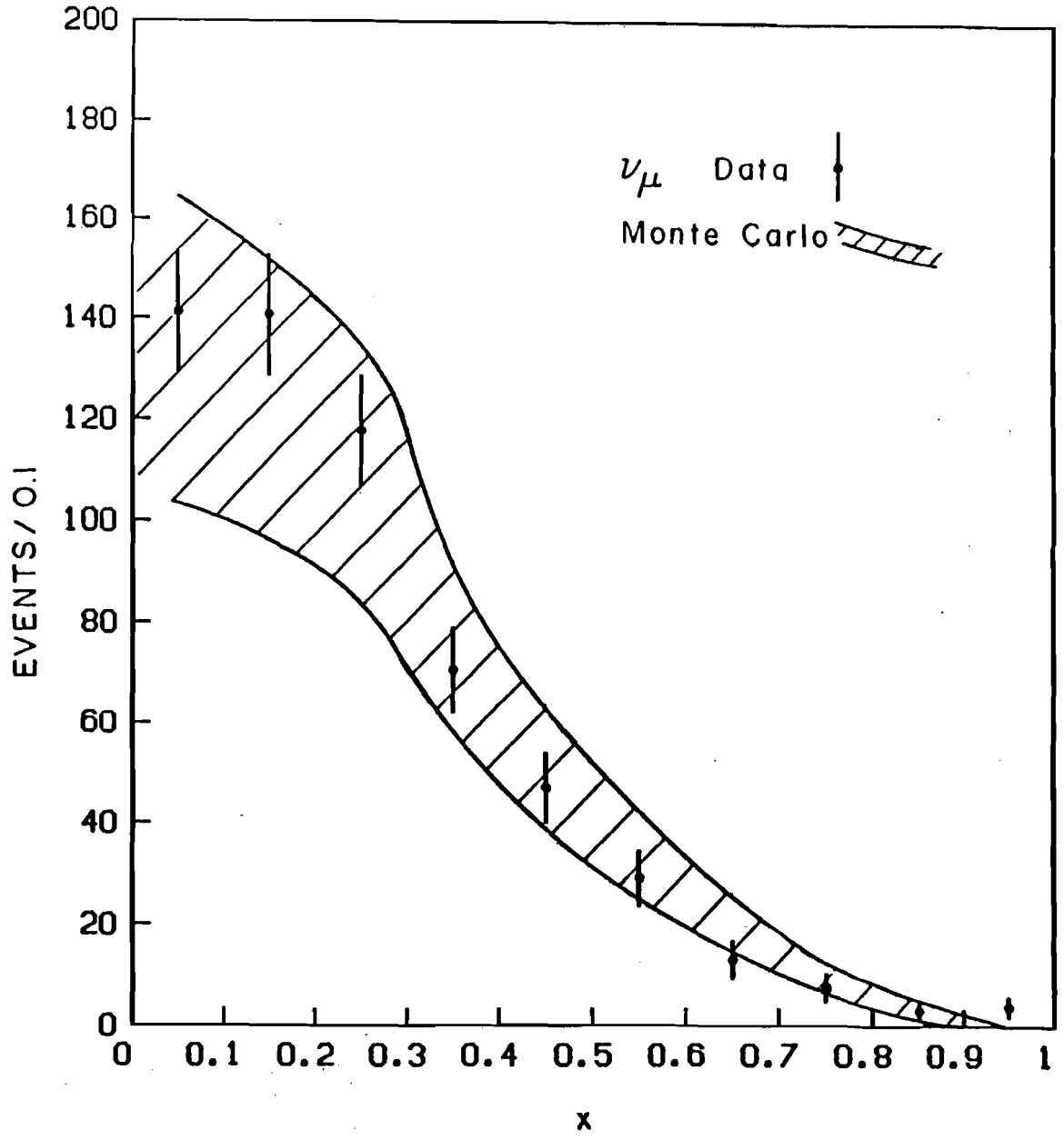
200
180
160
140
120
100
80
60
40
20
0
EVENTS / 0.1
ν_μ Data
Monte Carlo
0
0.1
0.2
0.3
0.4
0.5
0.6
0.7
0.8
0.9
1
x

Figure 16.

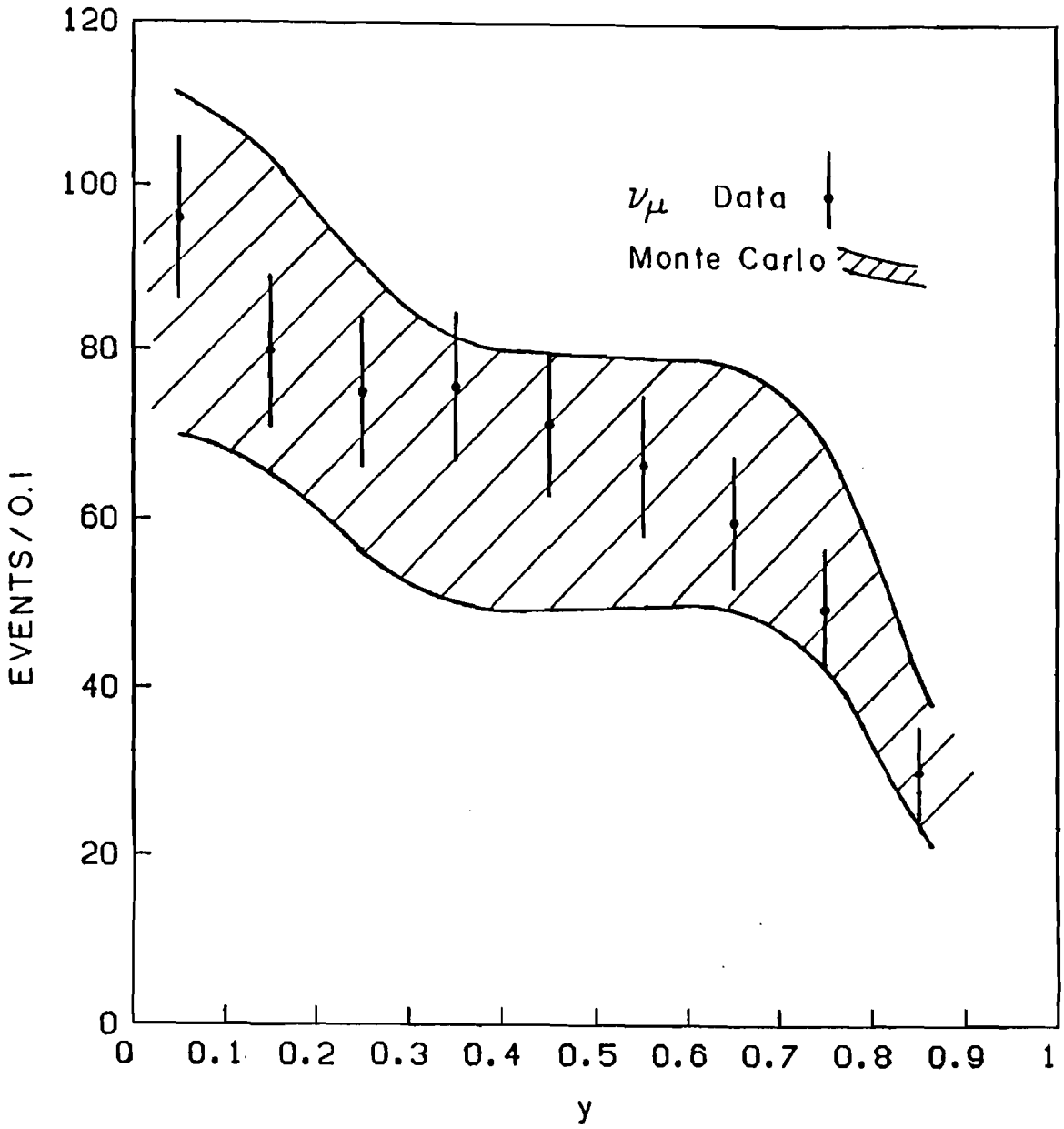
120
100
80
60
40
20
0
EVENTS / 0.1
0
0.1
0.2
0.3
0.4
0.5
0.6
0.7
0.8
0.9
1
y
ν_μ Data
Monte Carlo

Figure 17.

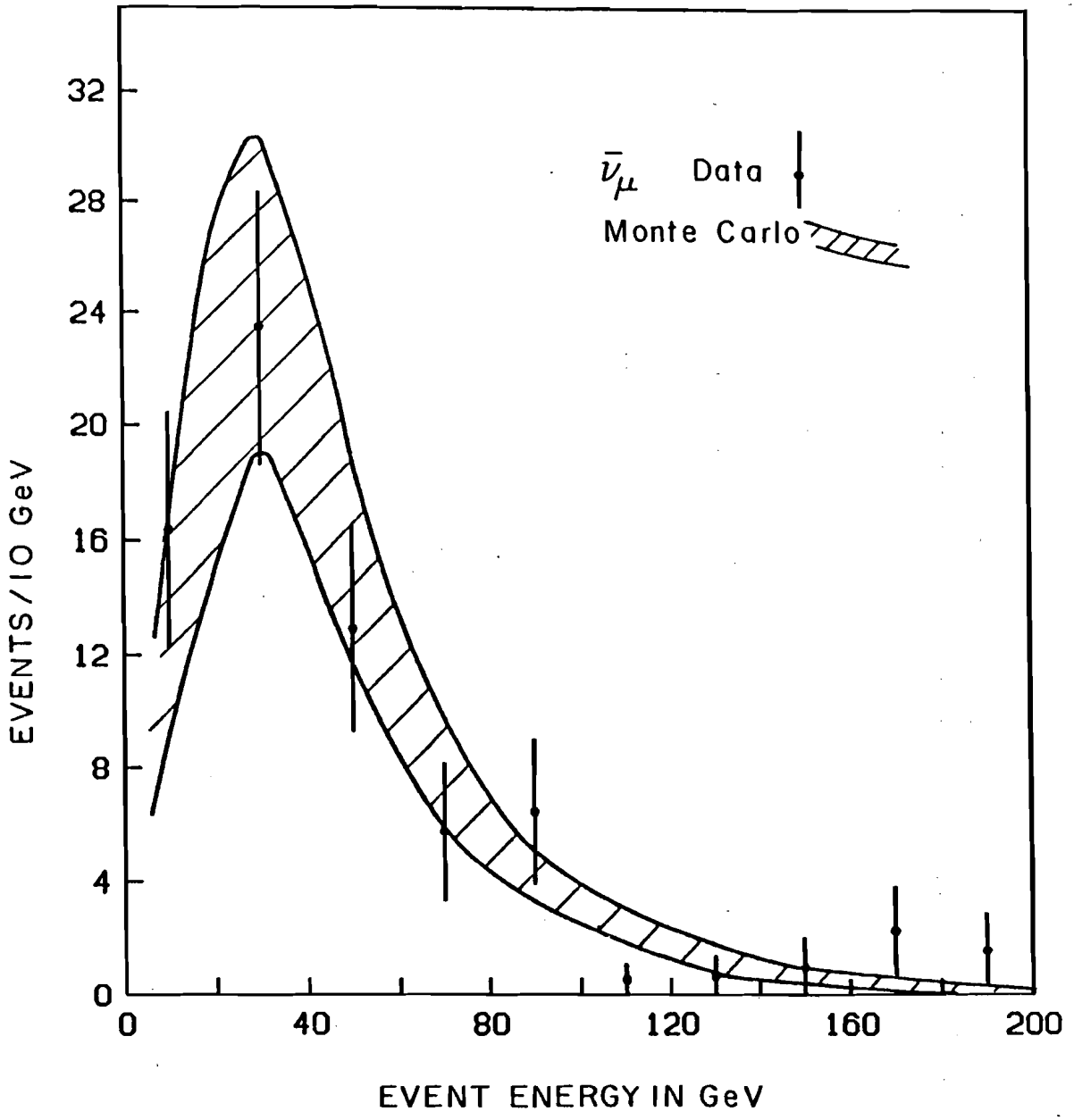
32
28
24
20
16
12
8
4
0
EVENTS / 10 GeV
0
40
80
120
160
200
EVENT ENERGY IN GeV
$\bar{\nu}_\mu$ Data
Monte Carlo

Figure 18.

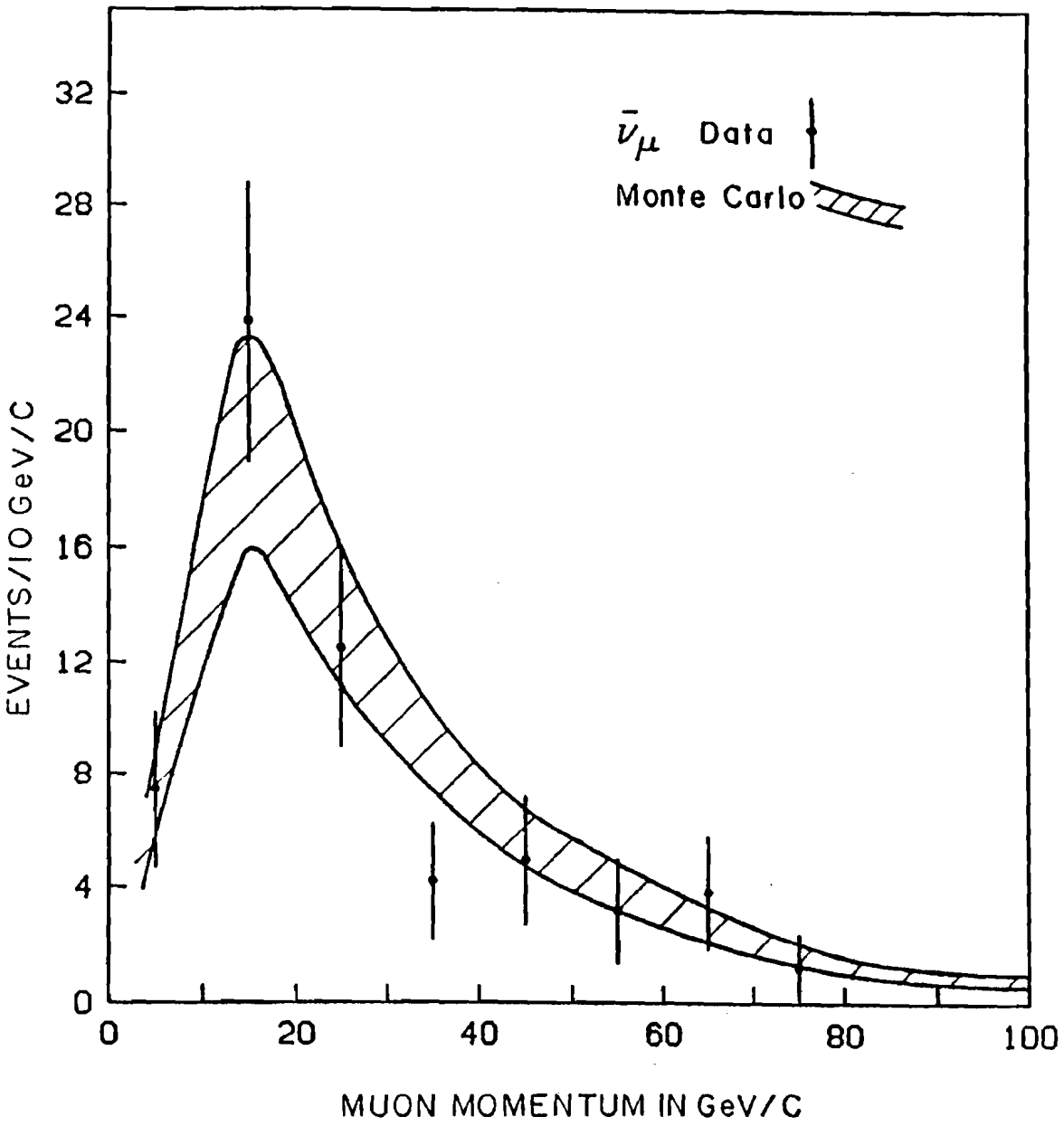
$\bar{\nu}_\mu$ Data
Monte Carlo
EVENTS/10 GeV/C
MUON MOMENTUM IN GeV/C
0
4
8
12
16
20
24
28
32
0
20
40
60
80
100

Figure 19.

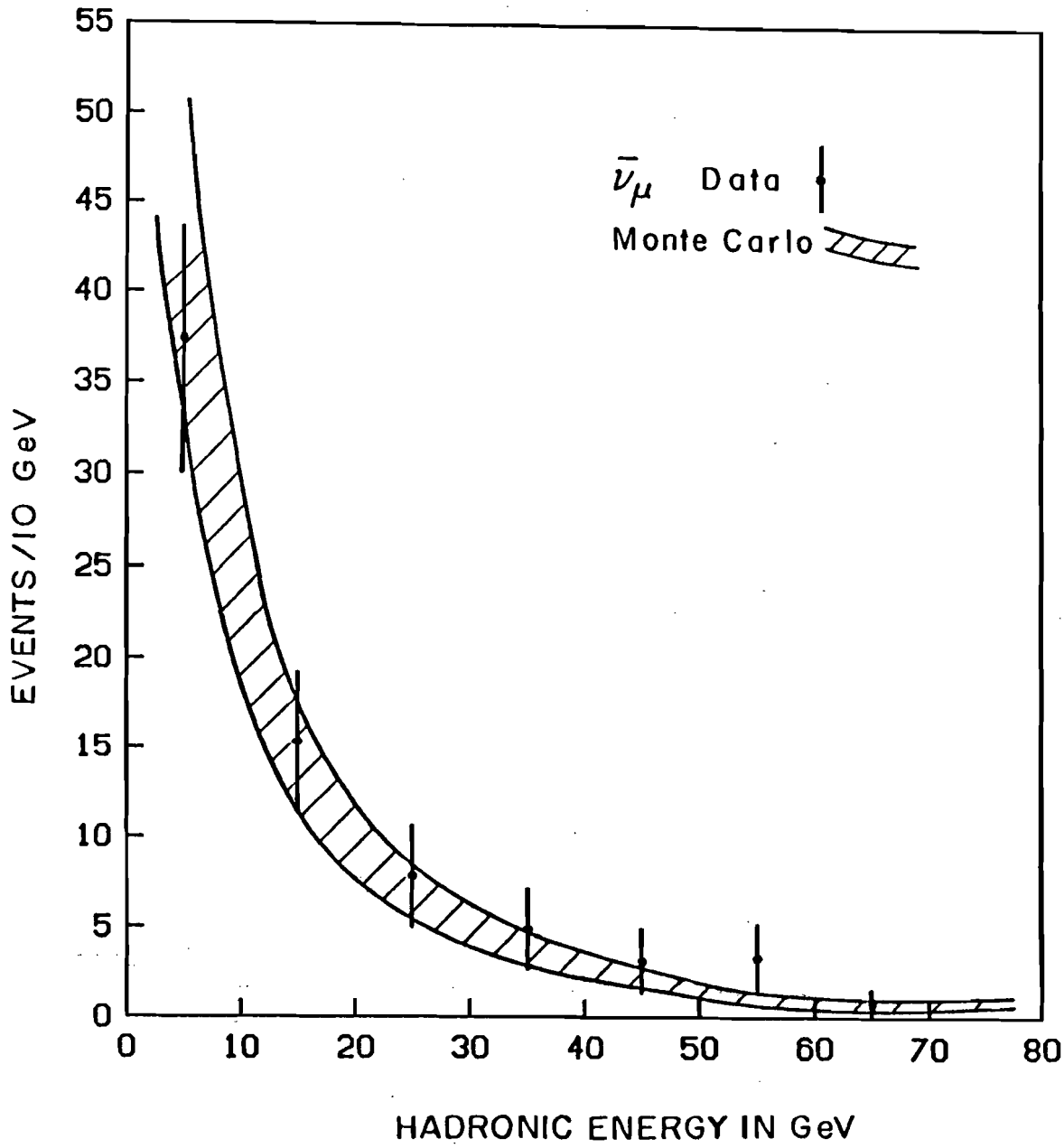
55
50
45
40
35
30
25
20
15
10
5
0
EVENTS/10 GeV
$\bar{\nu}_\mu$ Data
Monte Carlo
0
10
20
30
40
50
60
70
80
HADRONIC ENERGY IN GeV

Figure 20.

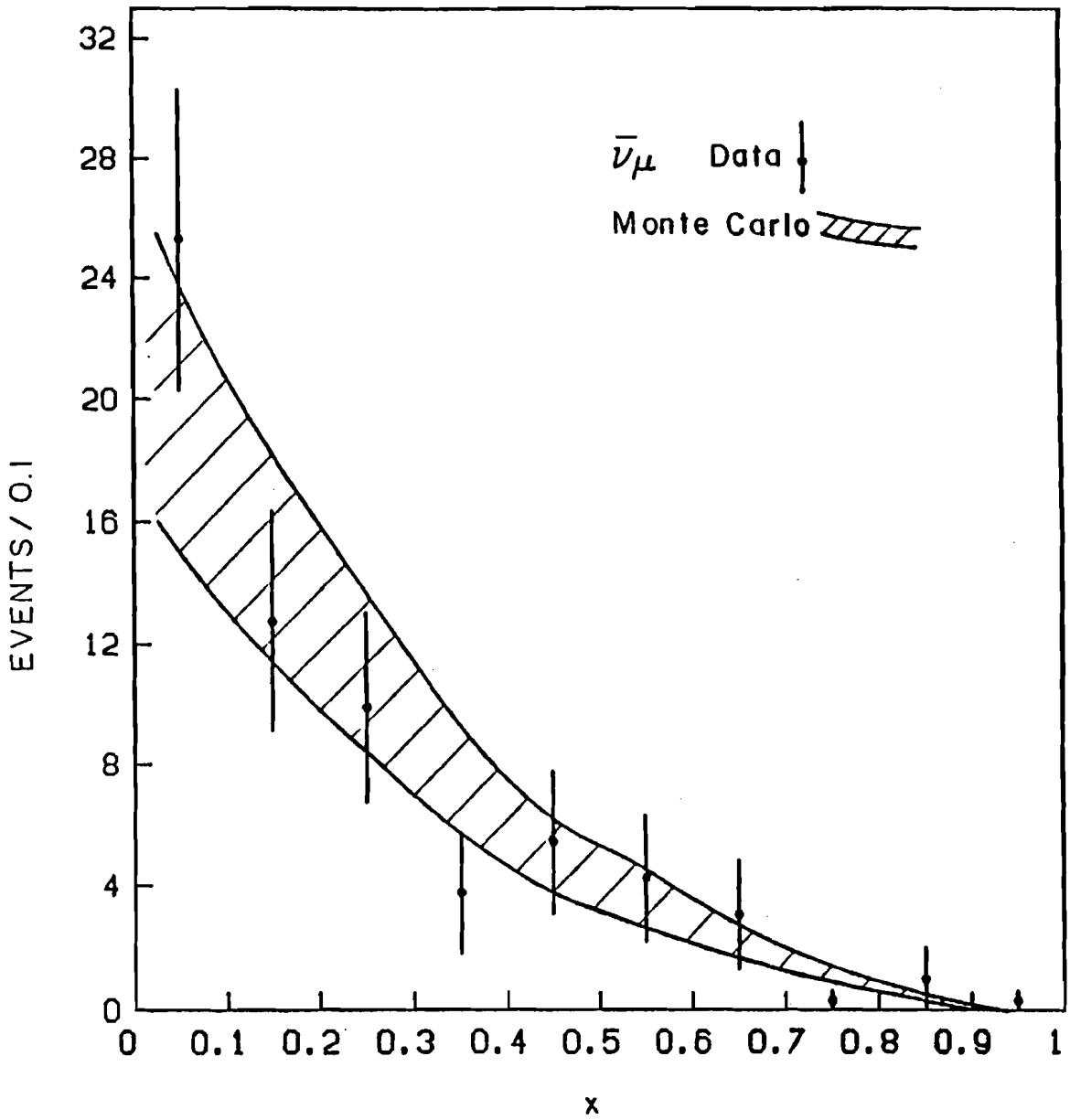
32
28
24
20
16
12
8
4
0
EVENTS / 0.1
$\bar{\nu}_\mu$ Data
Monte Carlo
0
0.1
0.2
0.3
0.4
0.5
0.6
0.7
0.8
0.9
1
x

Figure 21.

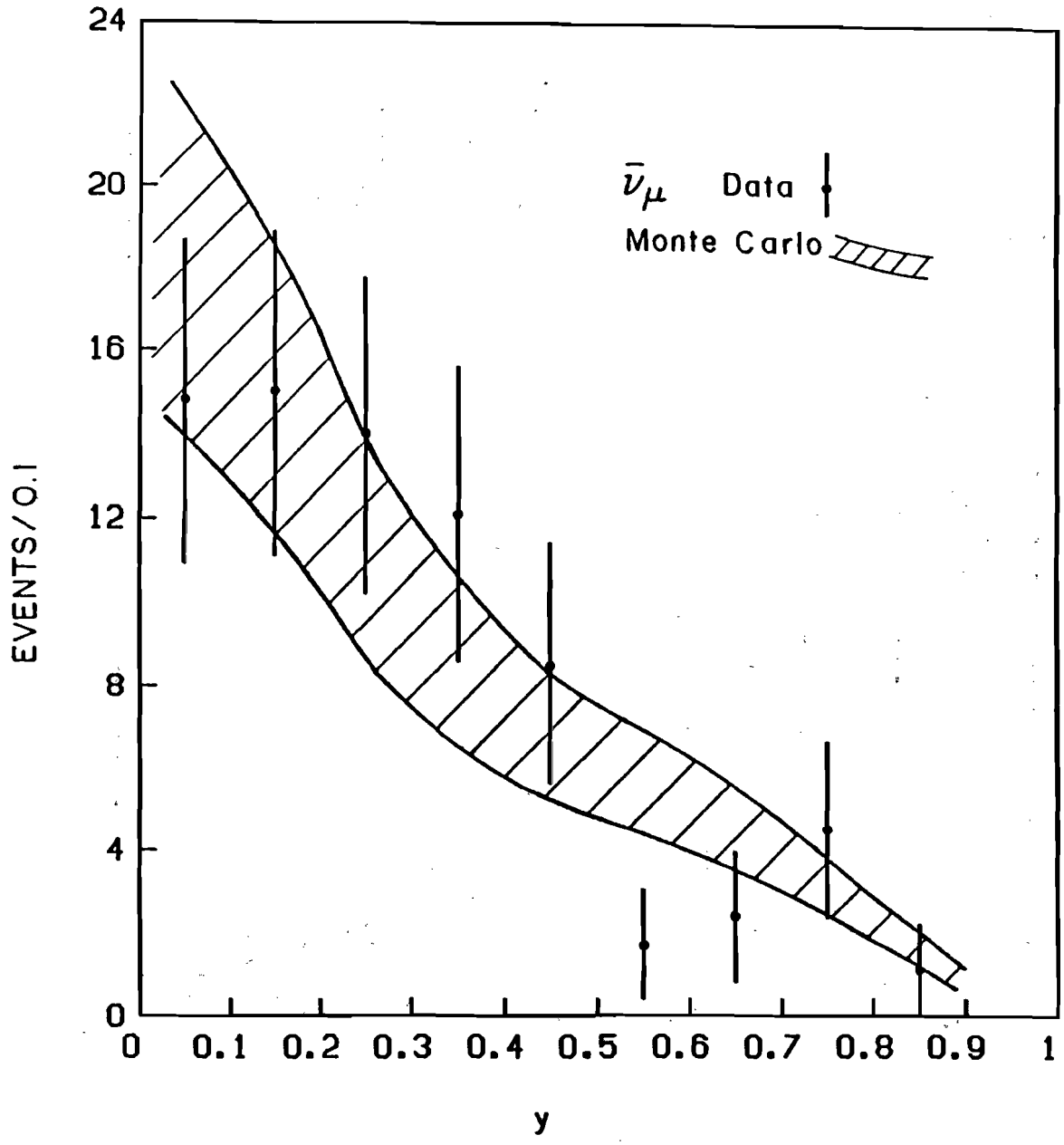
24
20
16
12
8
4
0
EVENTS/0.1
$\bar{\nu}_\mu$ Data
Monte Carlo
0
0.1
0.2
0.3
0.4
0.5
0.6
0.7
0.8
0.9
1
y

Figure 22.

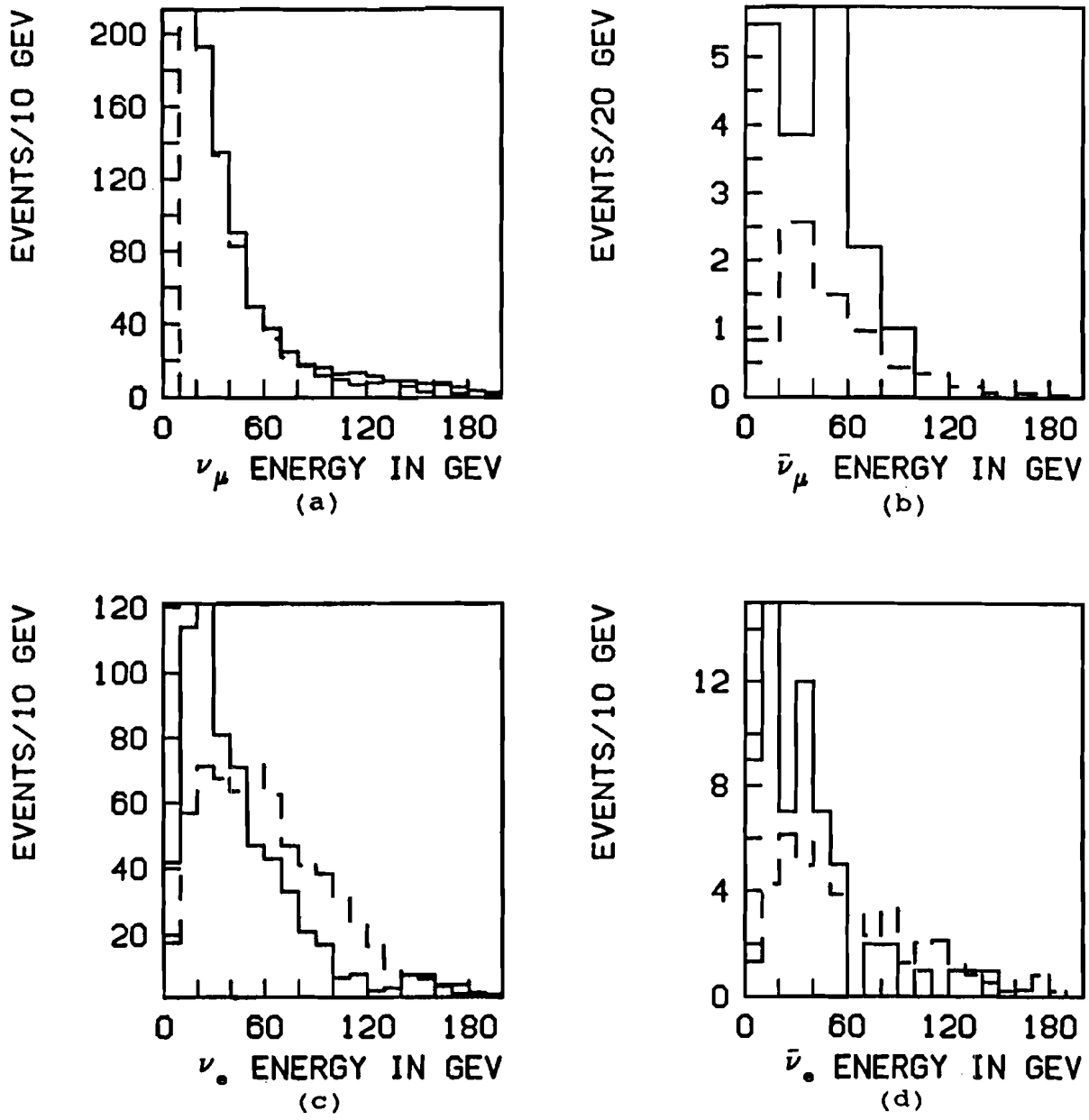
EVENTS/10 GEV
200
160
120
80
40
0
0
60
120
180
ν_μ ENERGY IN GEV
(a)
EVENTS/20 GEV
5
4
3
2
1
0
0
60
120
180
$\bar{\nu}_\mu$ ENERGY IN GEV
(b)
EVENTS/10 GEV
120
100
80
60
40
20
0
60
120
180
ν_e ENERGY IN GEV
(c)
EVENTS/10 GEV
12
8
4
0
0
60
120
180
$\bar{\nu}_e$ ENERGY IN GEV
(d)

Figure 23.

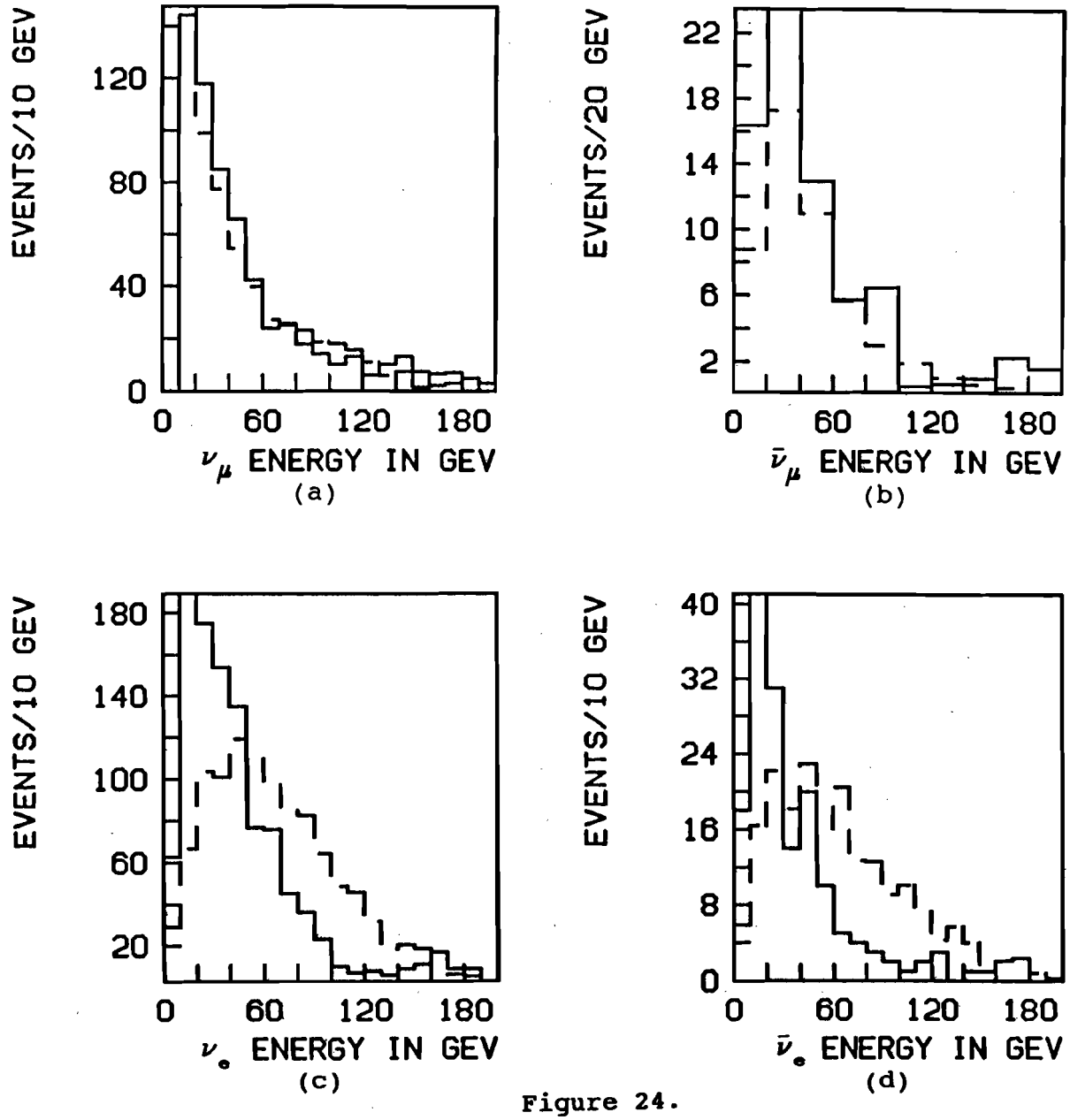
EVENTS/10 GEV
120
80
40
0
0
60
120
180
ν_μ ENERGY IN GEV
(a)
EVENTS/20 GEV
22
18
14
10
6
2
0
60
120
180
$\bar{\nu}_\mu$ ENERGY IN GEV
(b)
EVENTS/10 GEV
180
140
100
60
20
0
60
120
180
ν_e ENERGY IN GEV
(c)
EVENTS/10 GEV
40
32
24
16
8
0
0
60
120
180
$\bar{\nu}_e$ ENERGY IN GEV
(d)

Figure 24.

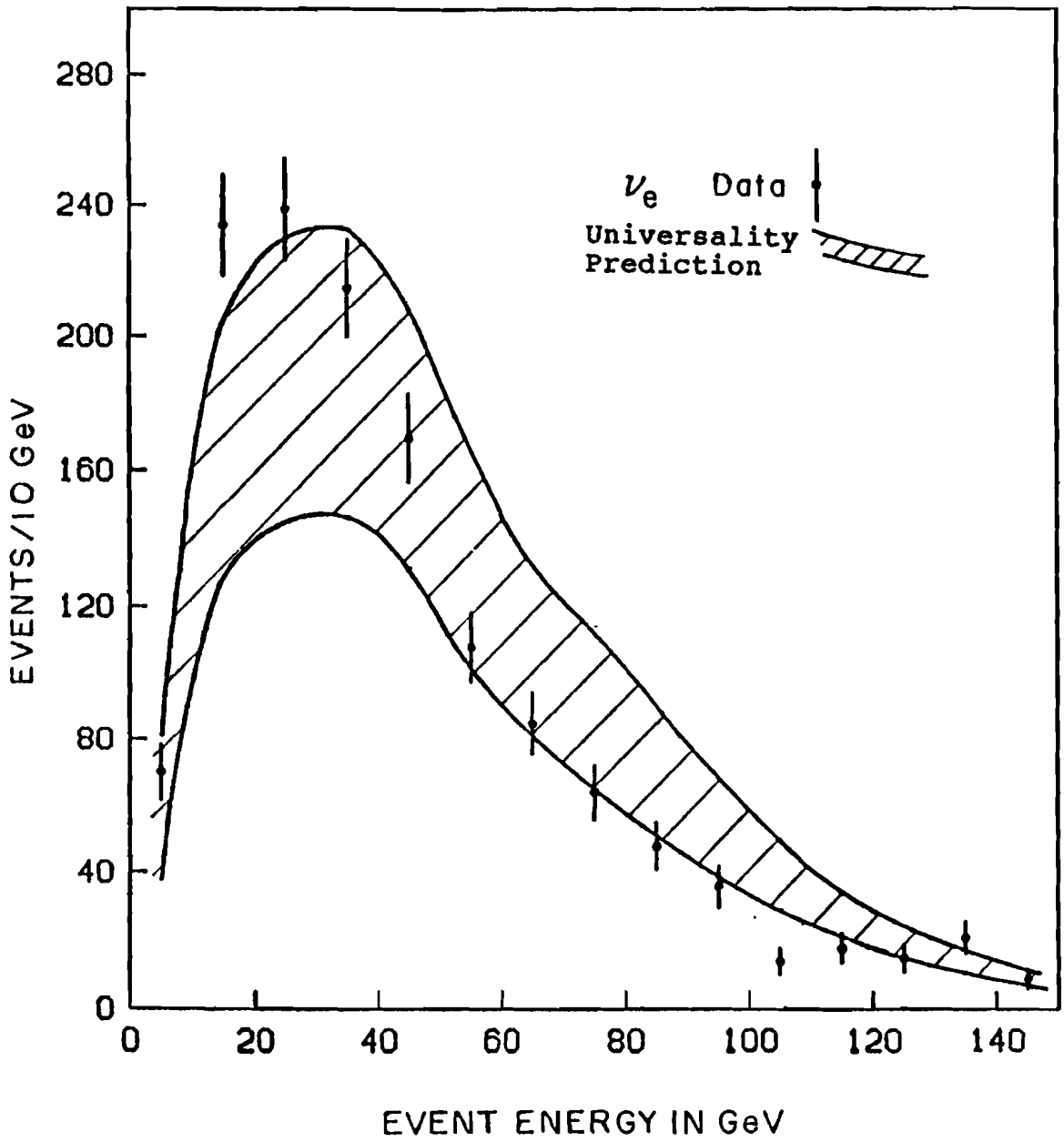
280
240
200
160
120
80
40
0
EVENTS/10 GeV
0
20
40
60
80
100
120
140
EVENT ENERGY IN GeV
ν_e Data
Universality
Prediction

Figure 25.

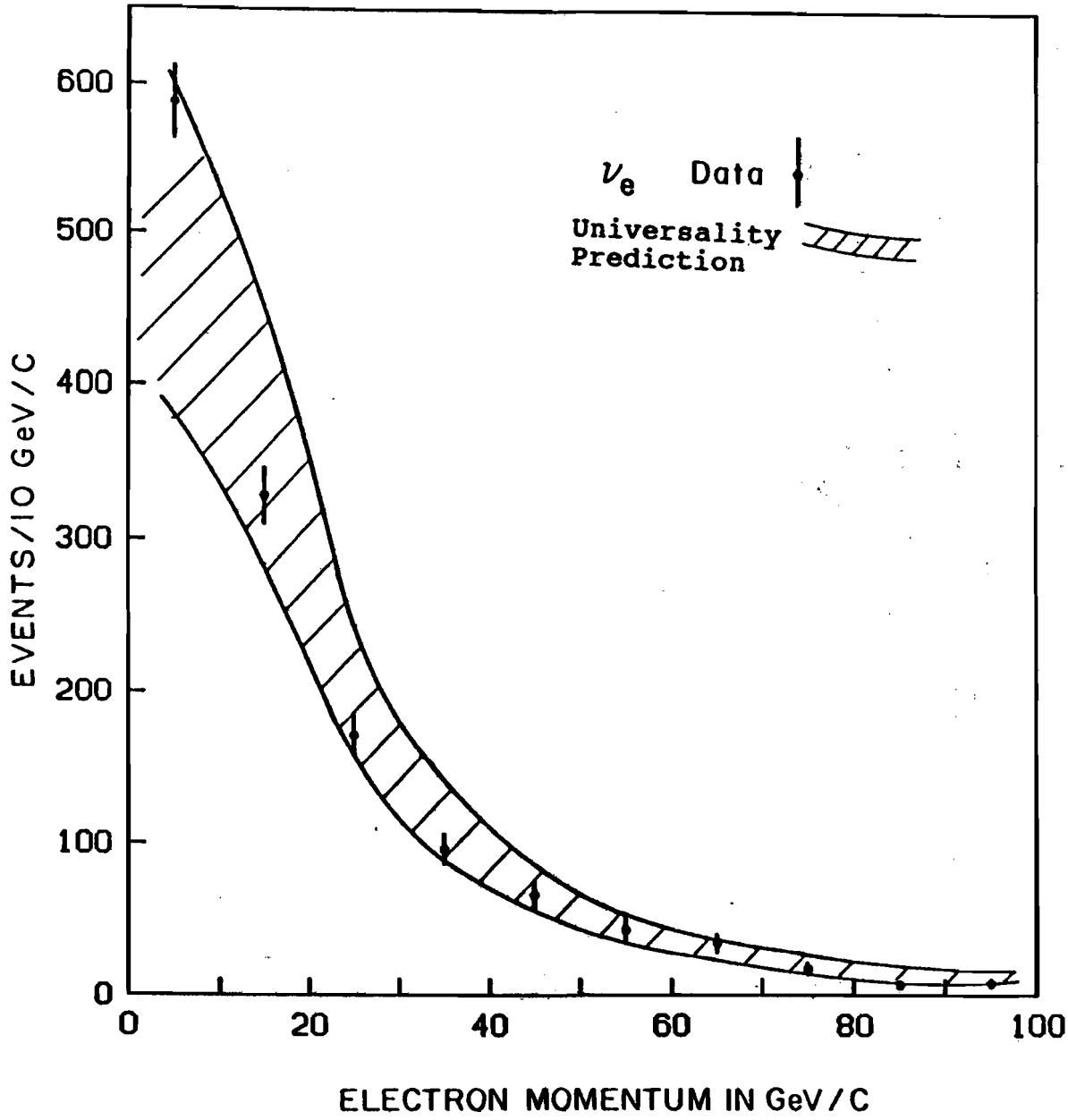
600
500
400
300
200
100
0
EVENTS/10 GeV/C
ν_e Data
Universality Prediction
0
20
40
60
80
100
ELECTRON MOMENTUM IN GeV/C

Figure 26.

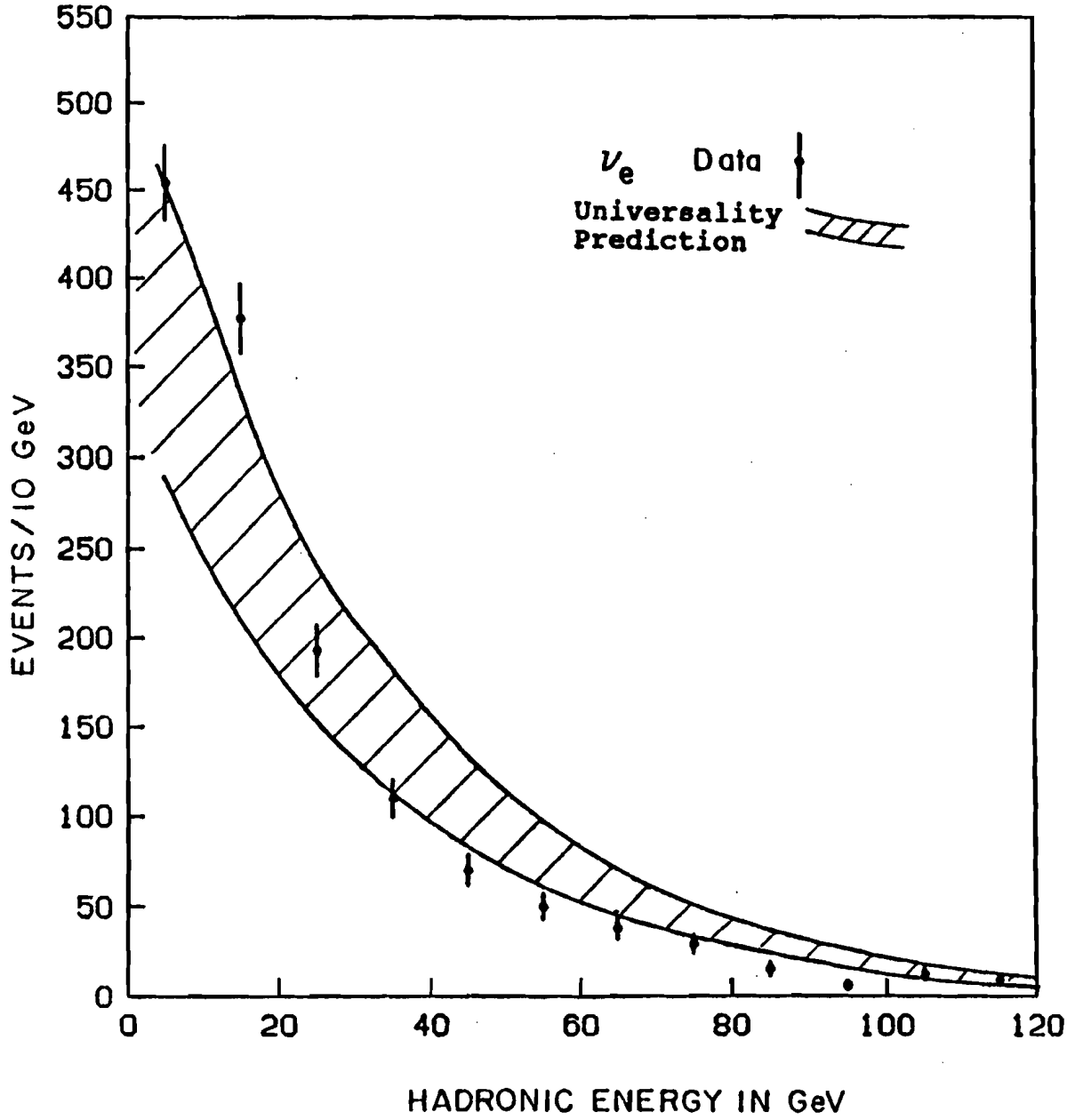
550
500
450
400
350
300
250
200
150
100
50
0
EVENTS/10 GeV
0
20
40
60
80
100
120
HADRONIC ENERGY IN GeV
ν_e Data
Universality
Prediction

Figure 27.

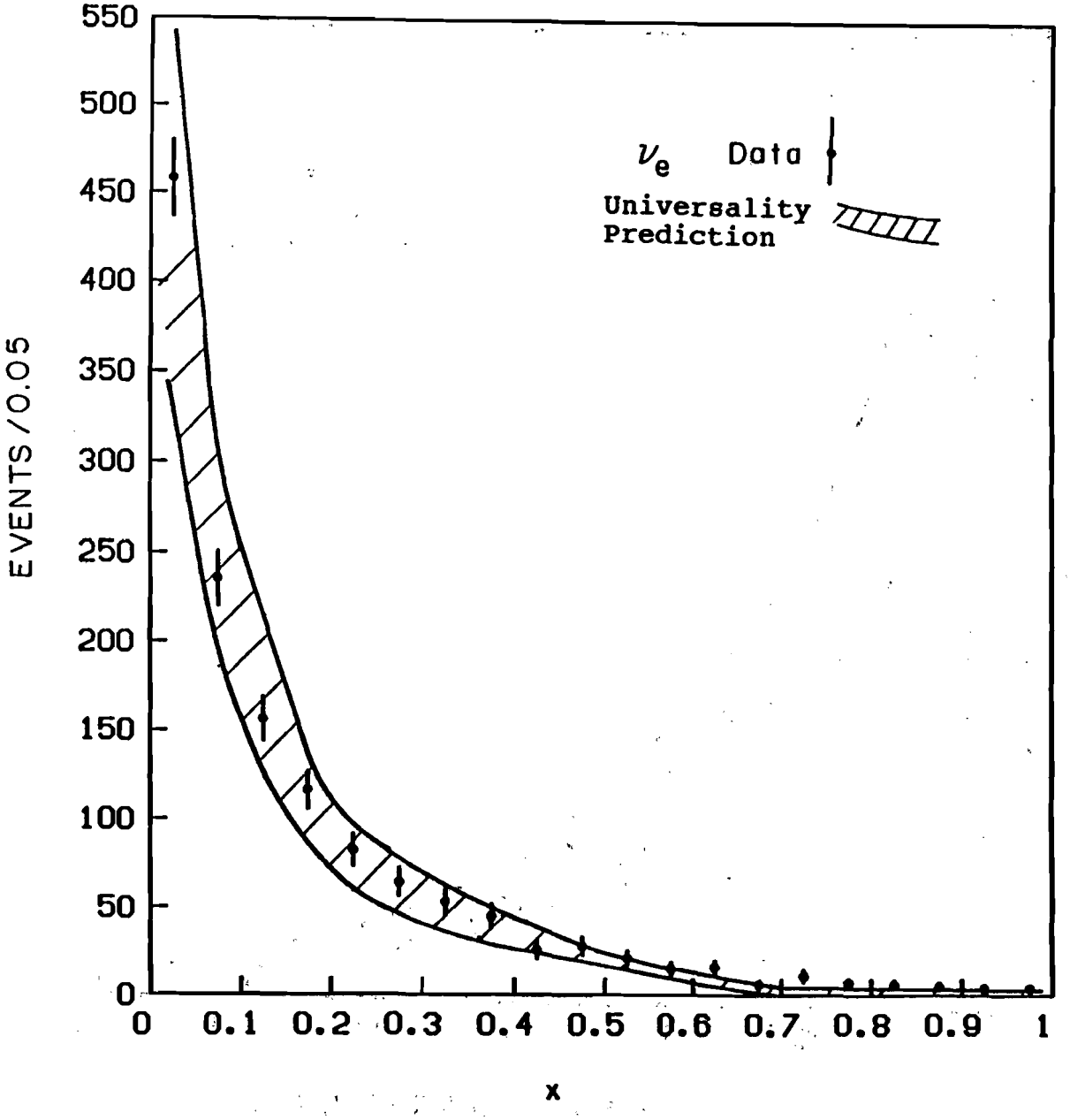
550
500
450
400
350
300
250
200
150
100
50
0
EVENTS / 0.05
ν_e Data
Universality Prediction
0
0.1
0.2
0.3
0.4
0.5
0.6
0.7
0.8
0.9
1
x

Figure 28.

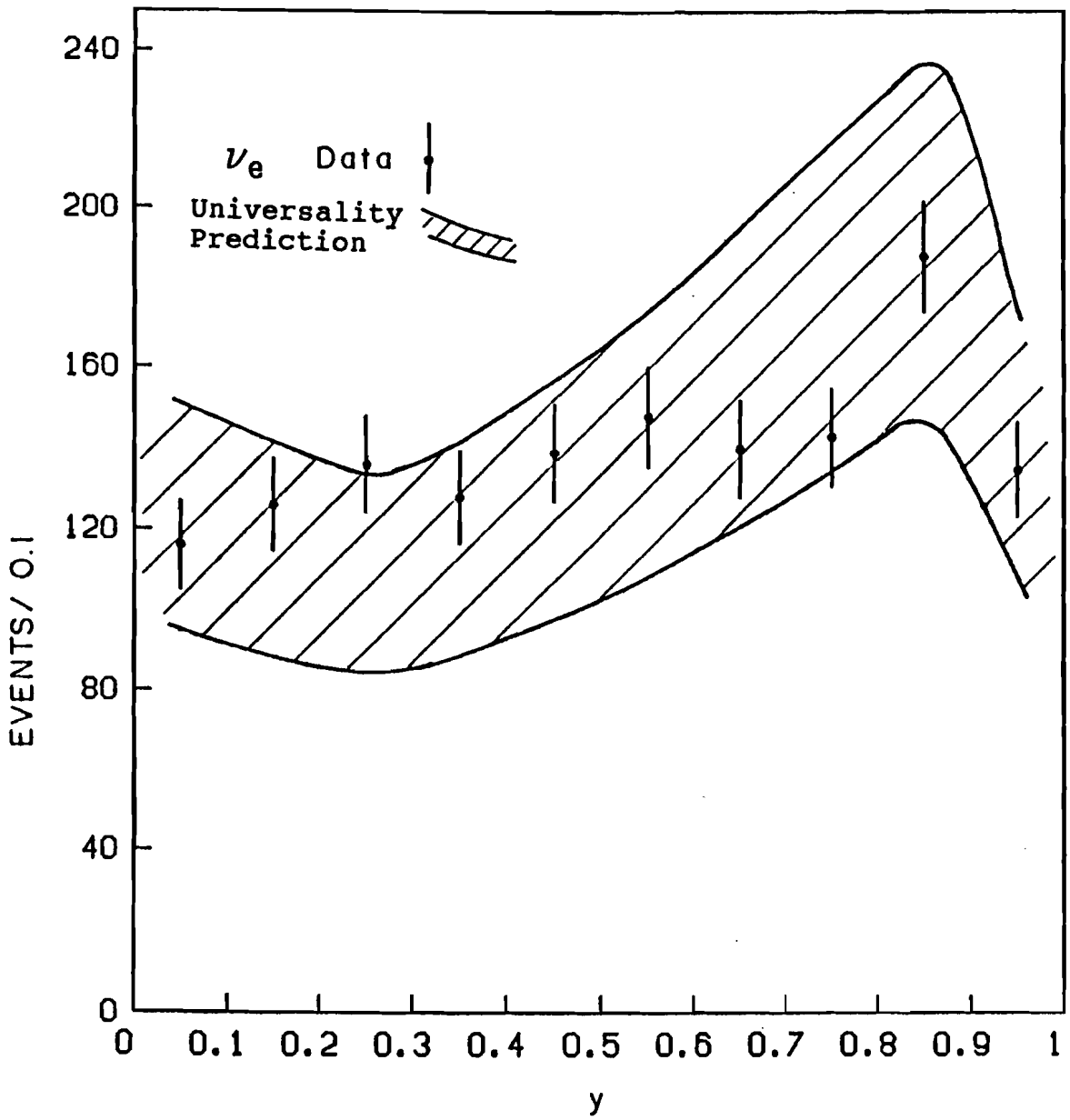
240
200
160
120
80
40
0
EVENTS/ 0.1
ν_e Data
Universality
Prediction
0
0.1
0.2
0.3
0.4
0.5
0.6
0.7
0.8
0.9
1
y

Figure 29.

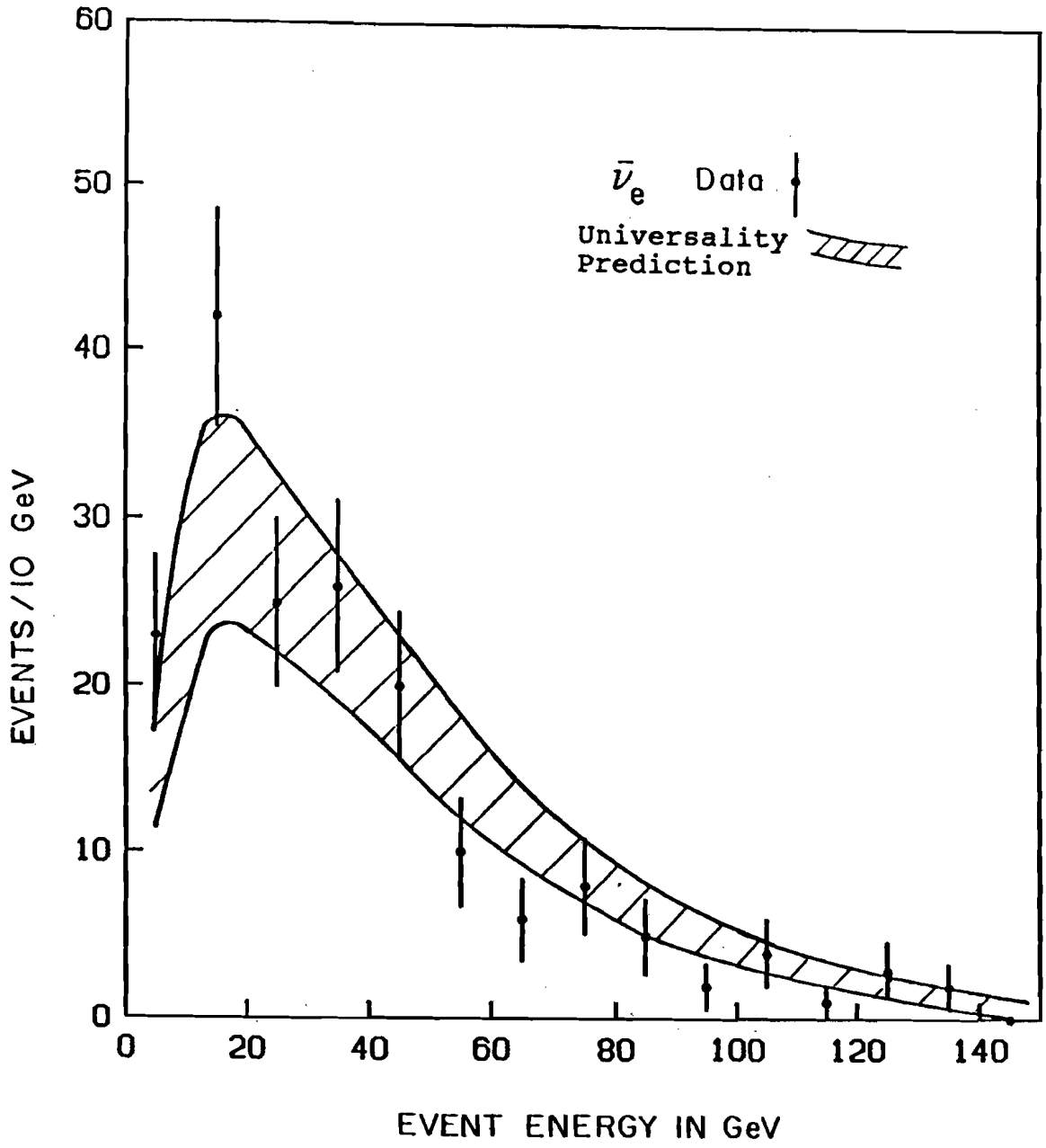
60
50
40
30
20
10
0
EVENTS/10 GeV
$\bar{\nu}_e$ Data
Universality Prediction
0
20
40
60
80
100
120
140
EVENT ENERGY IN GeV

Figure 30.

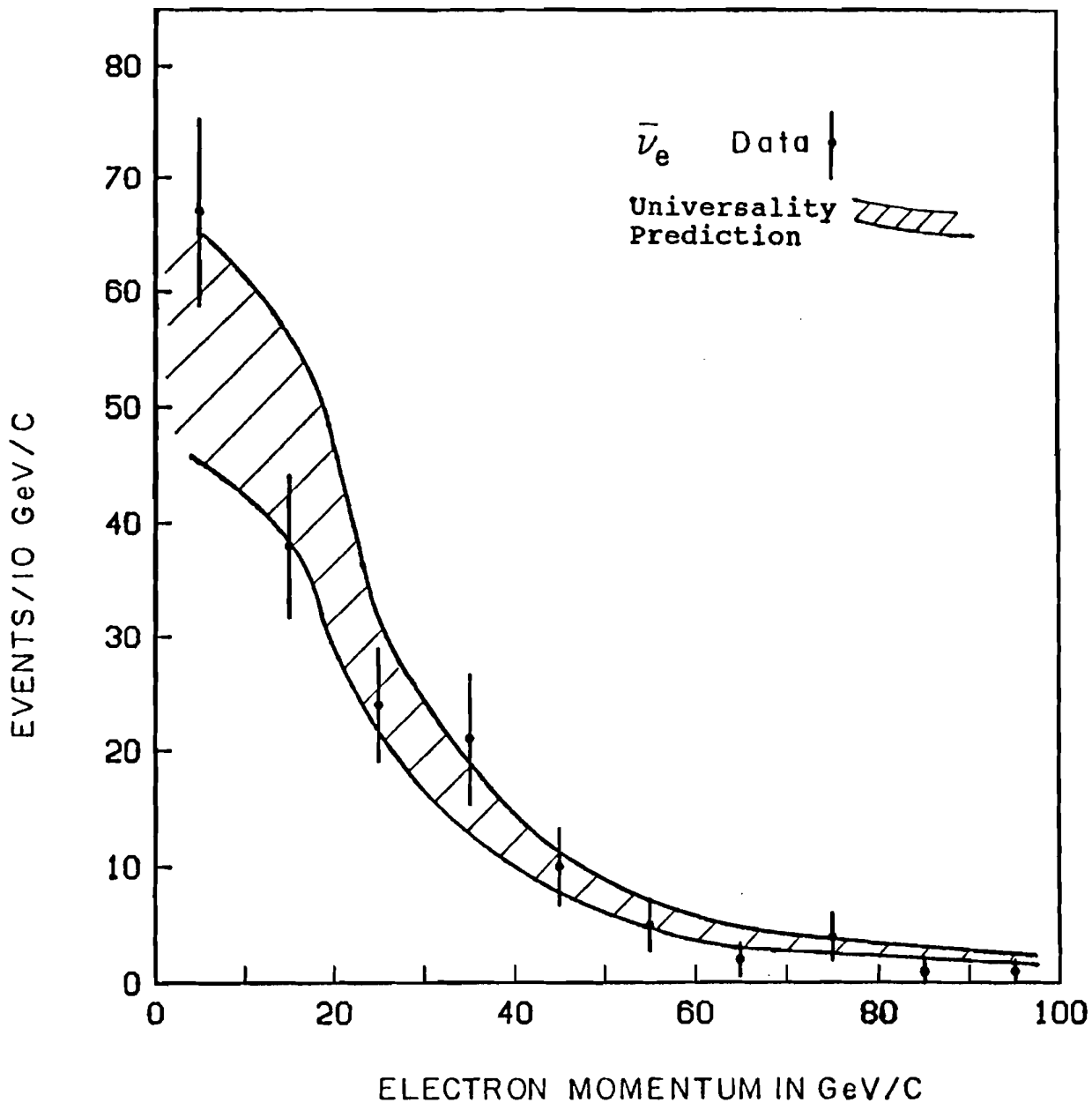
80
70
60
50
40
30
20
10
0
EVENTS/10 GeV/C
$\bar{\nu}_e$ Data
Universality Prediction
0
20
40
60
80
100
ELECTRON MOMENTUM IN GeV/C

Figure 31.

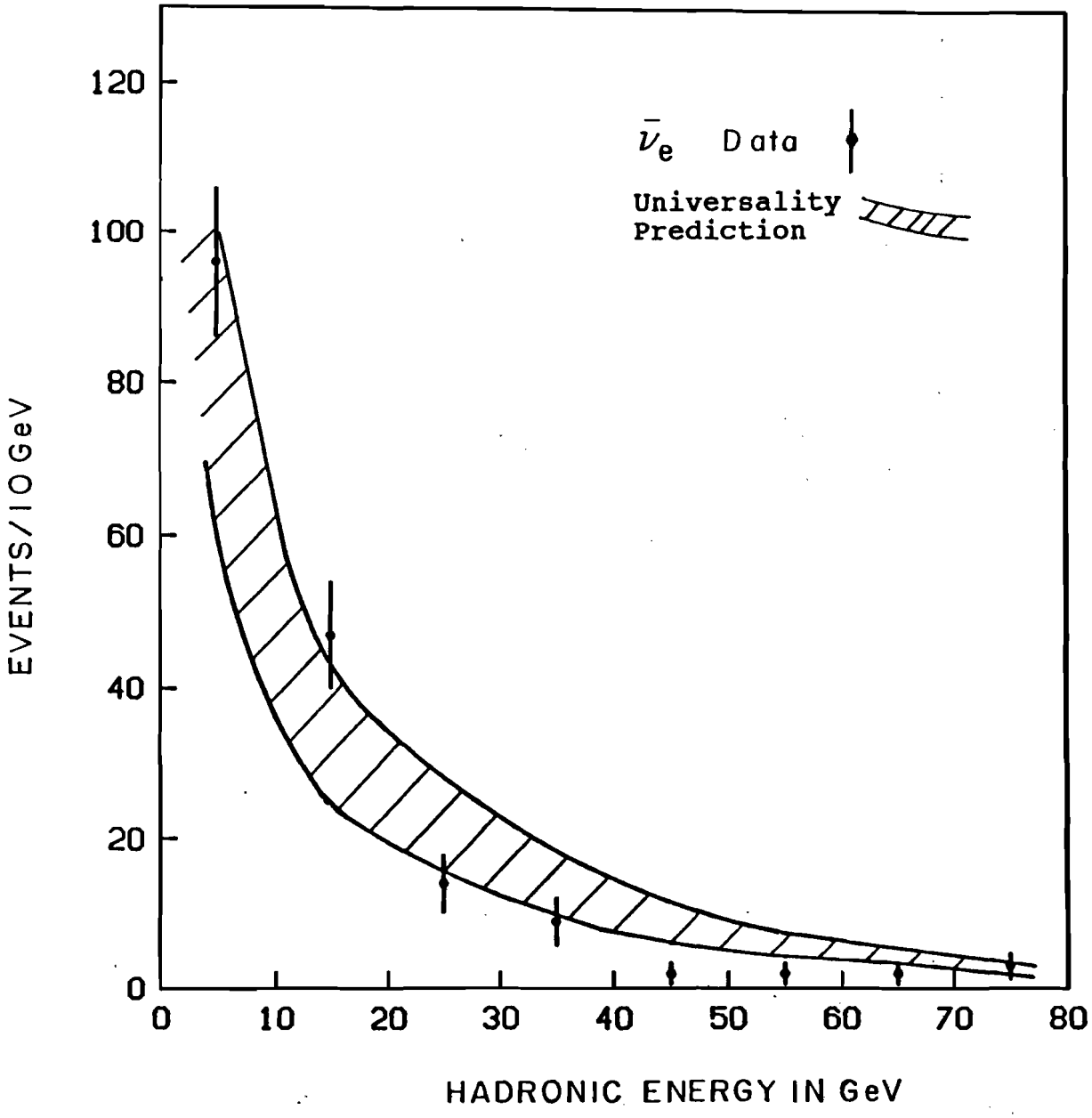
$\bar{\nu}_e$ Data
Universality Prediction
EVENTS/10 GeV
HADRONIC ENERGY IN GeV
0
20
40
60
80
100
120
0
10
20
30
40
50
60
70
80

Figure 32.

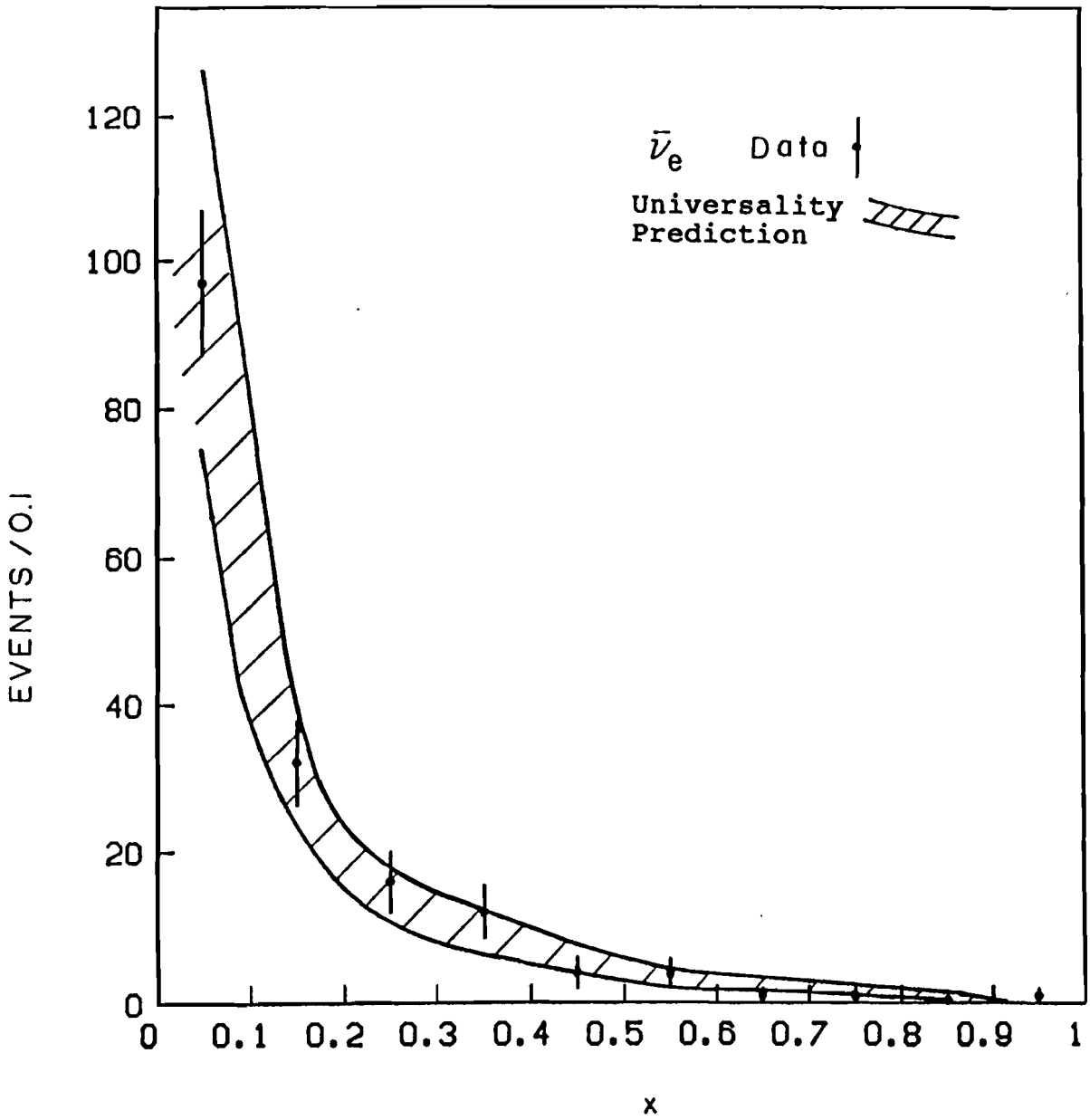
$\bar{\nu}_e$ Data
Universality Prediction
EVENTS / 0.1
120
100
80
60
40
20
0
0
0.1
0.2
0.3
0.4
0.5
0.6
0.7
0.8
0.9
1
x

Figure 33.

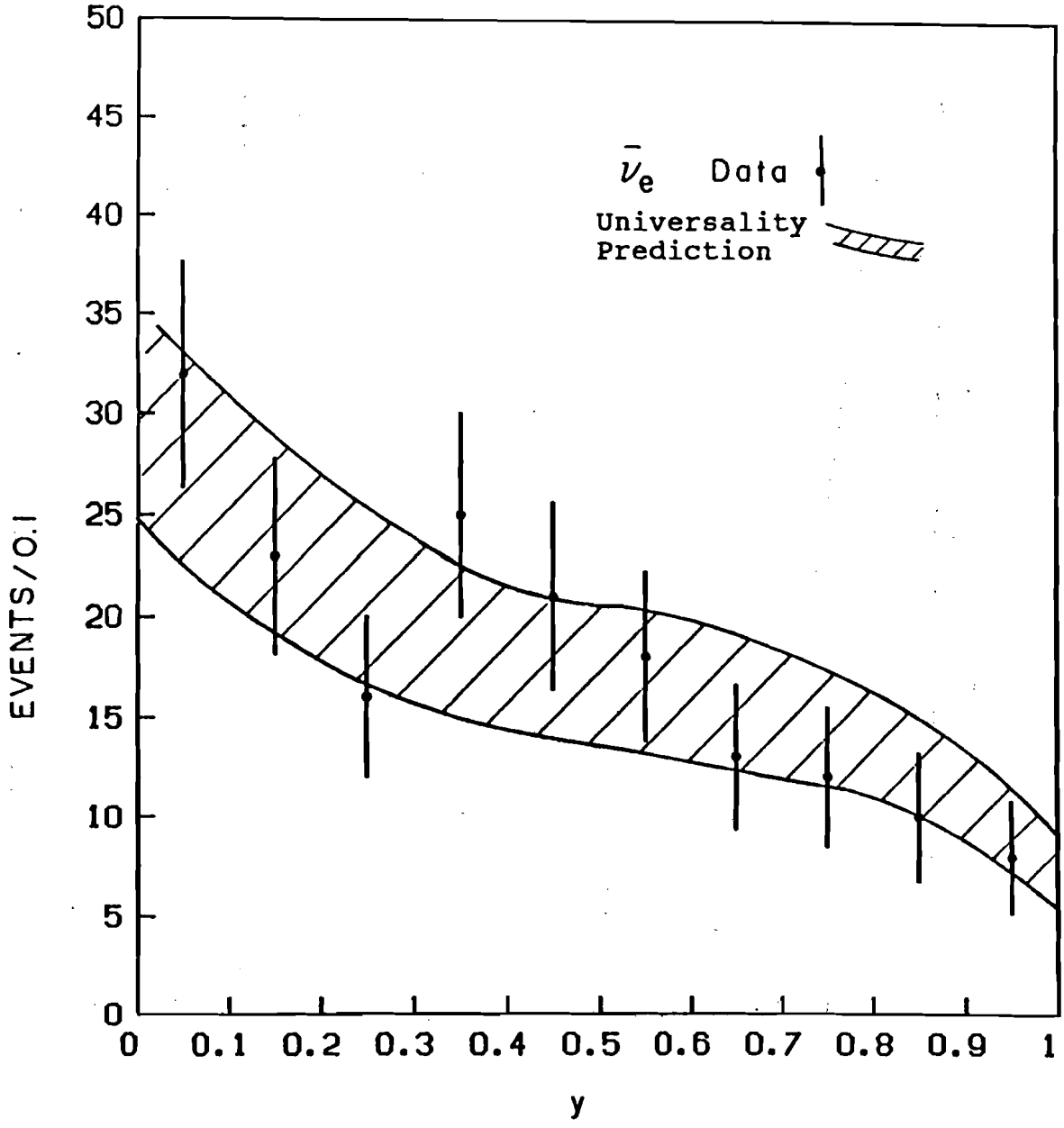
50
45
40
35
30
25
20
15
10
5
0
EVENTS/0.1
$\bar{\nu}_e$ Data
Universality
Prediction
0
0.1
0.2
0.3
0.4
0.5
0.6
0.7
0.8
0.9
1
y

Figure 34.

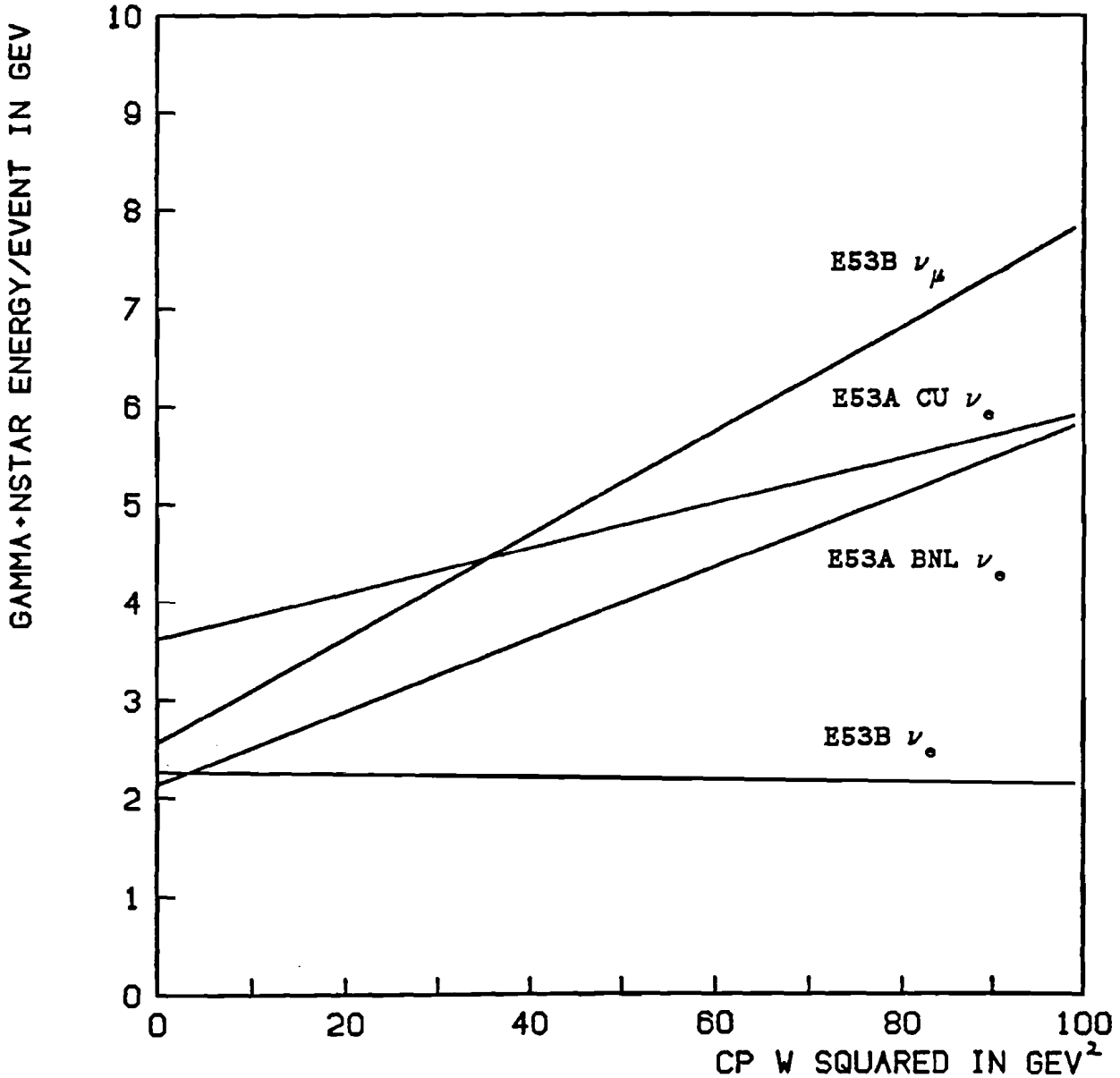
GAMMA*NSTAR ENERGY/EVENT IN GEV
10
9
8
7
6
5
4
3
2
1
0
0
20
40
60
80
100
CP W SQUARED IN GEV^2
E53B ν_μ
E53A CU ν_e
E53A BNL ν_e
E53B ν_e

Figure 35.

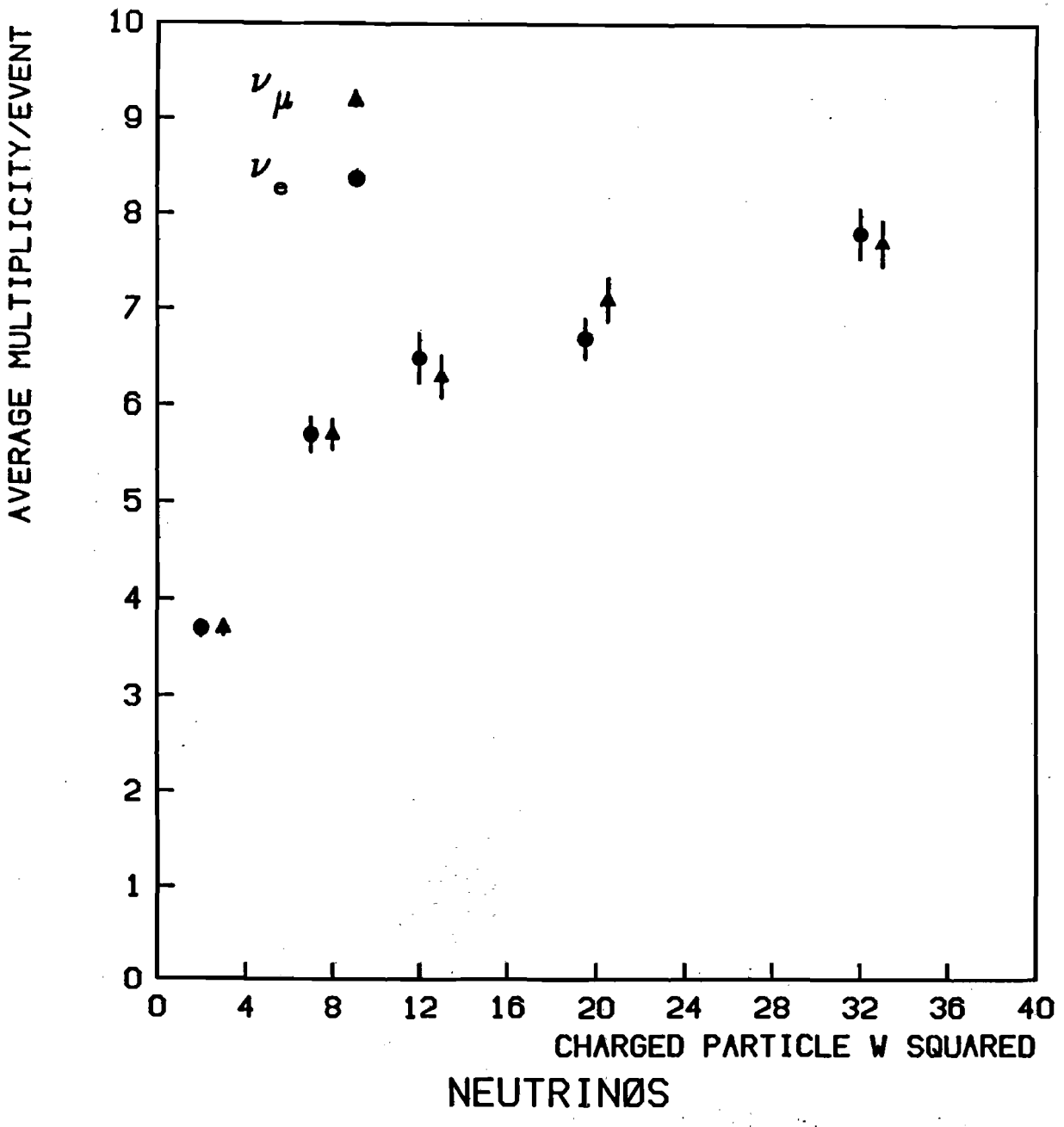
AVERAGE MULTIPLICITY/EVENT
10
9
8
7
6
5
4
3
2
1
0
ν_μ
ν_e
0
4
8
12
16
20
24
28
32
36
40
CHARGED PARTICLE W SQUARED
NEUTRINØS

Figure 36.

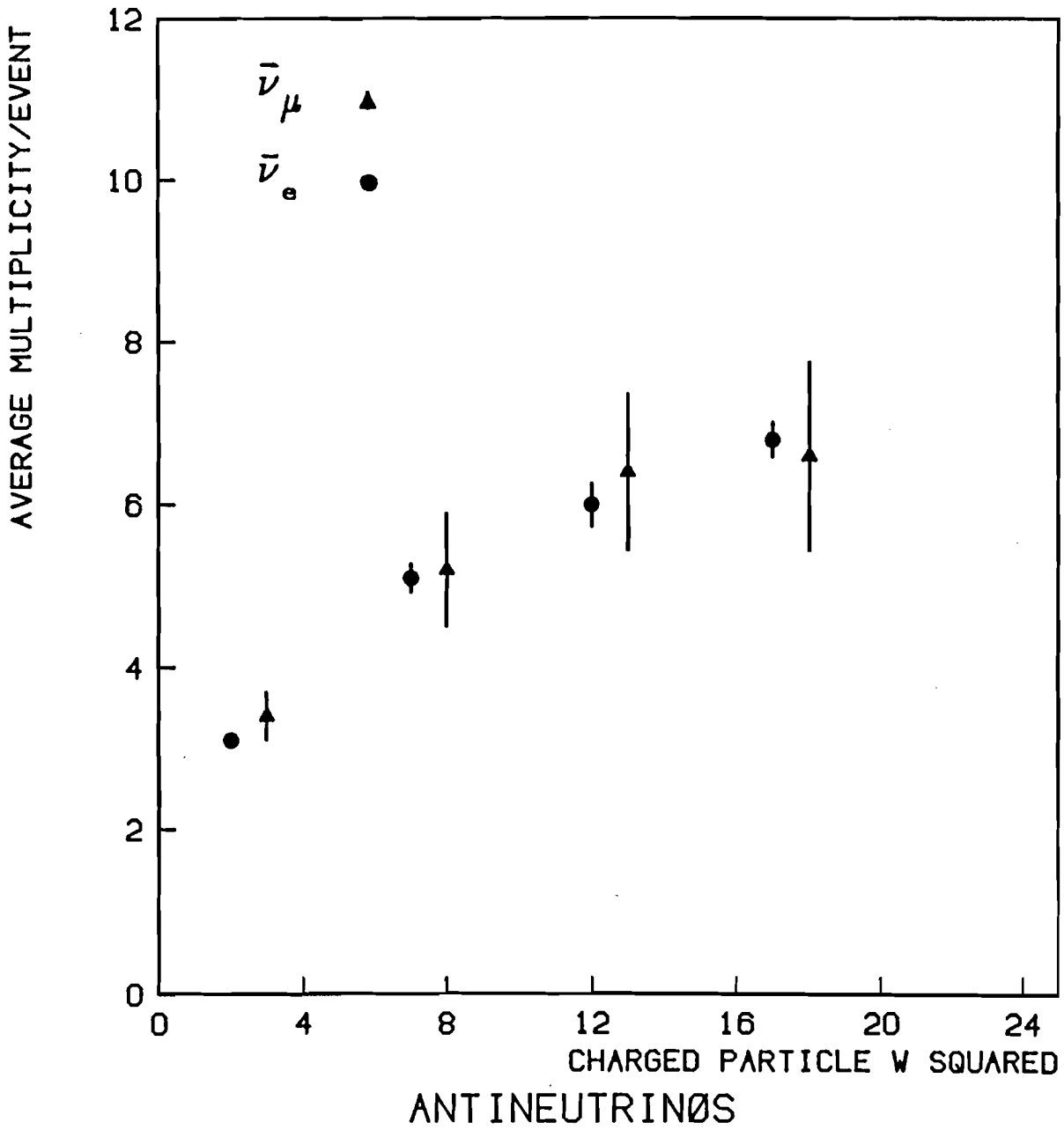
AVERAGE MULTIPLICITY/EVENT
12
10
8
6
4
2
0
$\bar{\nu}_\mu$
$\bar{\nu}_e$
0
4
8
12
16
20
24
CHARGED PARTICLE W SQUARED
ANTINEUTRINØS

Figure 37.

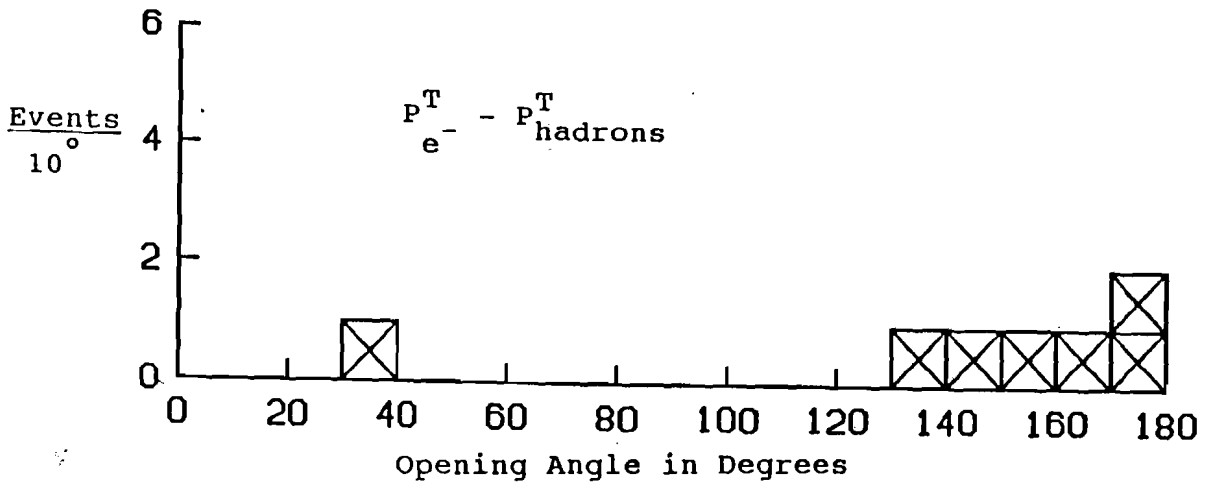

(a)

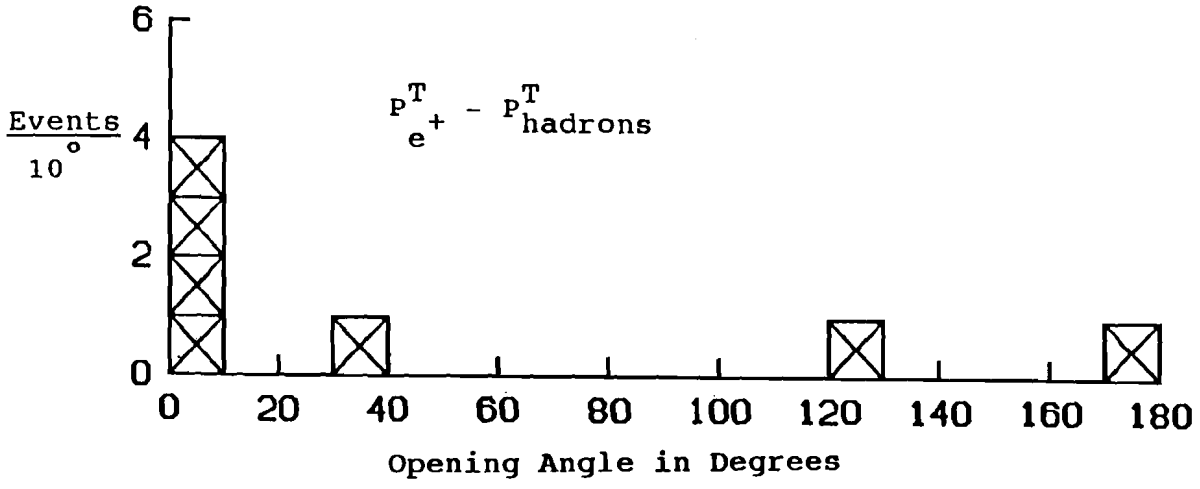

(b)

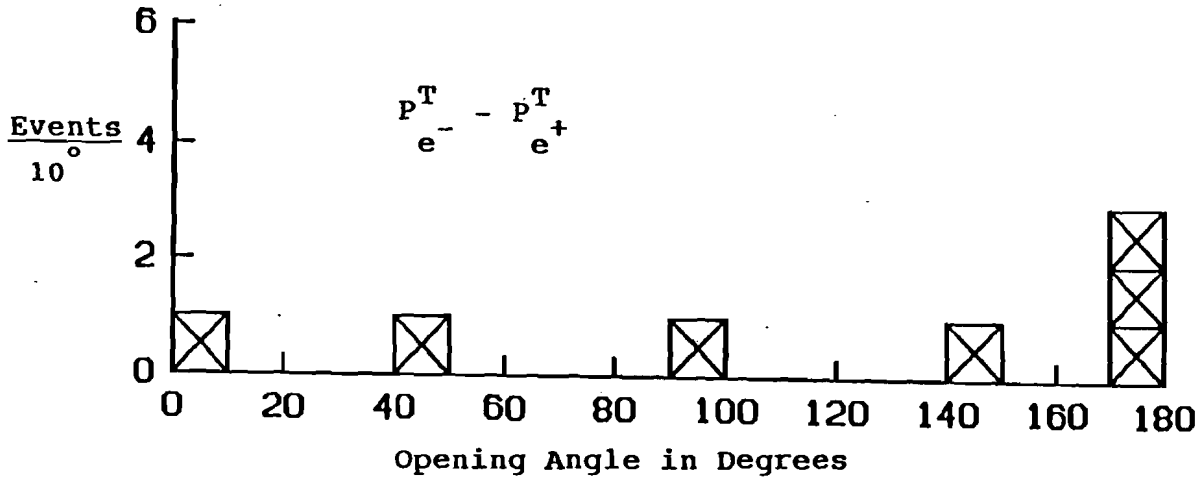

(c)

Figure 38.

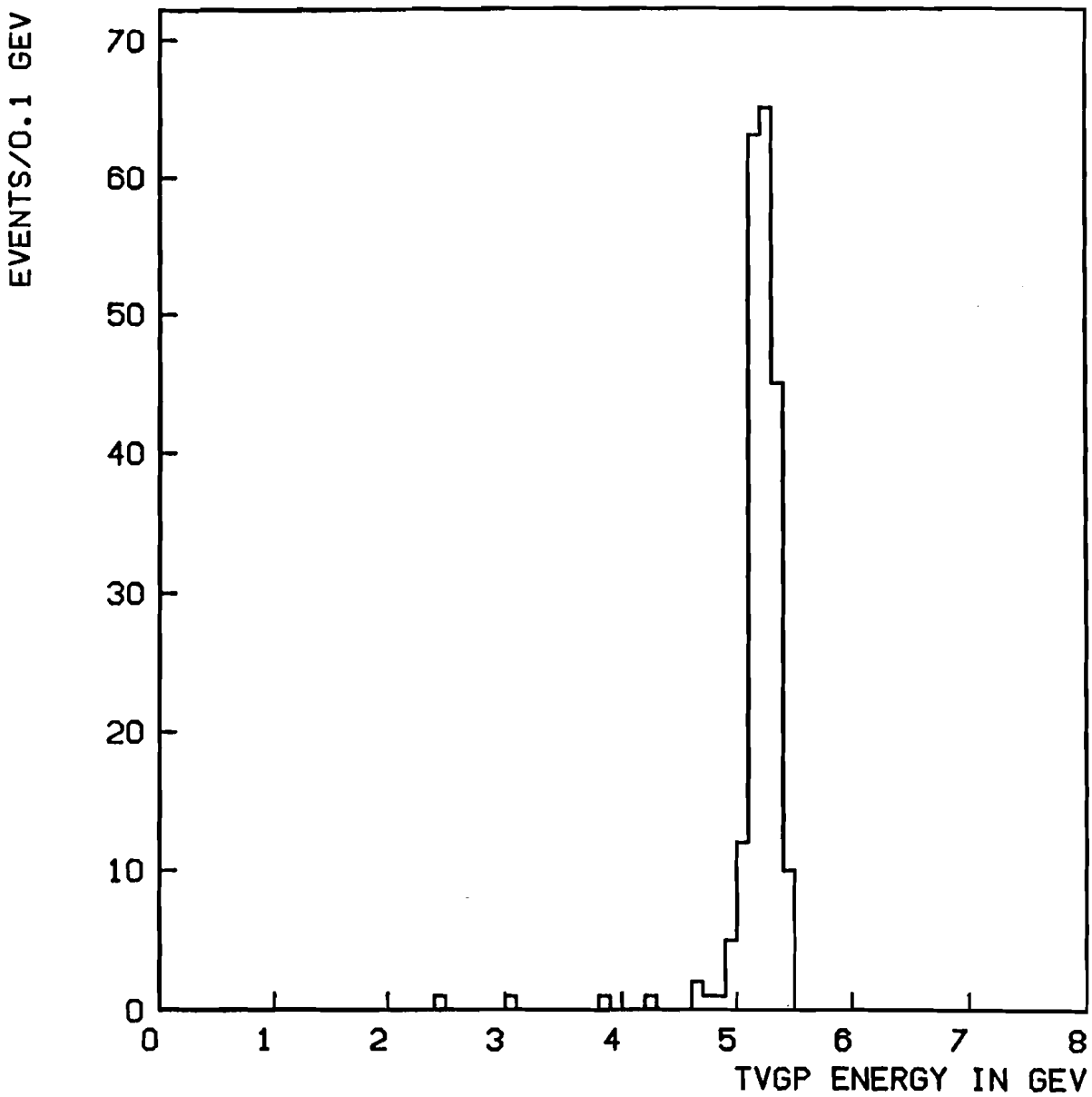
EVENTS/0.1 GEV
70
60
50
40
30
20
10
0
0
1
2
3
4
5
6
7
8
TVGP ENERGY IN GEV

Figure 39.

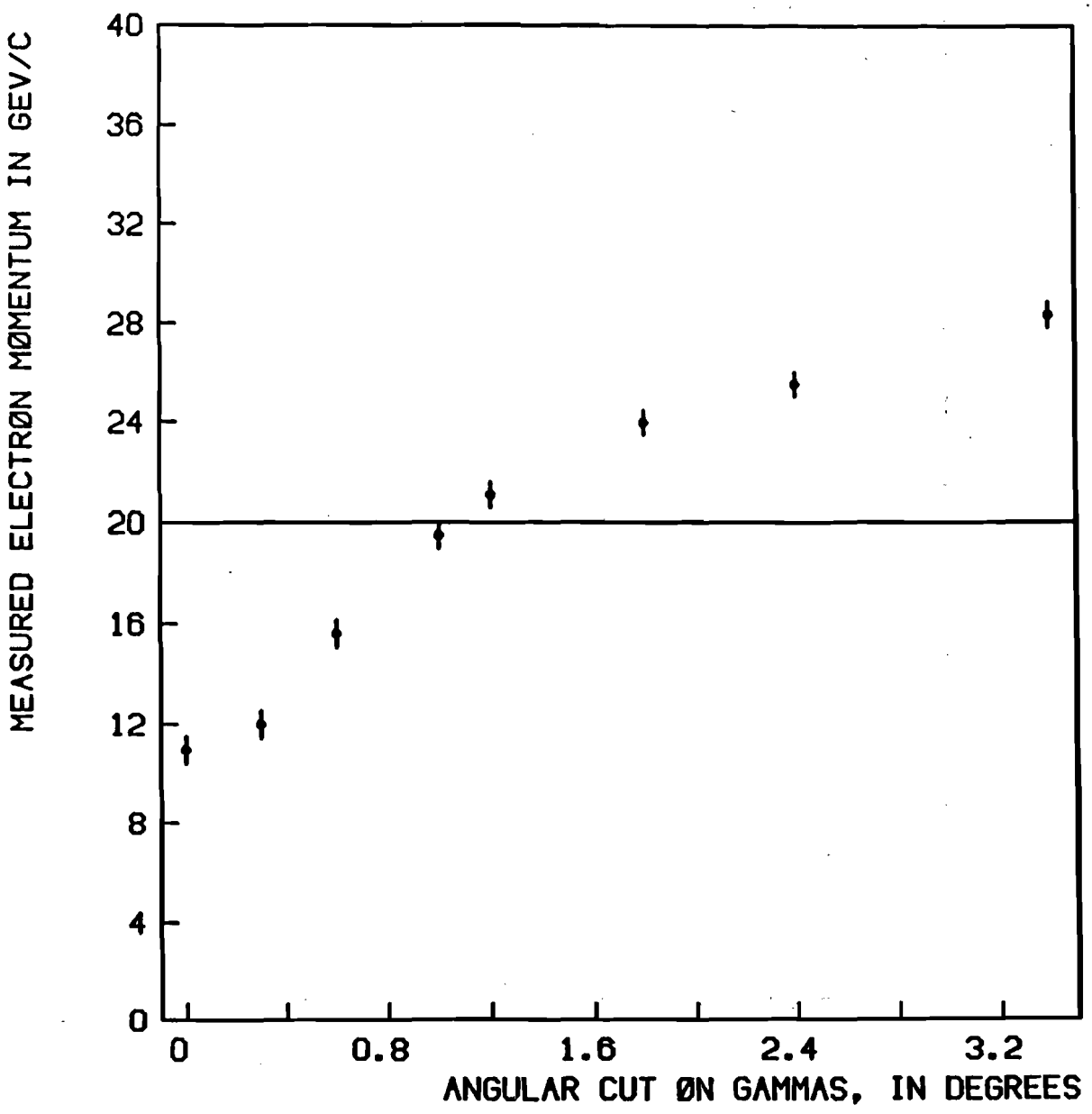
MEASURED ELECTRØN MØMENTUM IN GEV/C
40
36
32
28
24
20
16
12
8
4
0
0
0.8
1.6
2.4
3.2
ANGULAR CUT ØN GAMMAS, IN DEGREES

Figure 40.

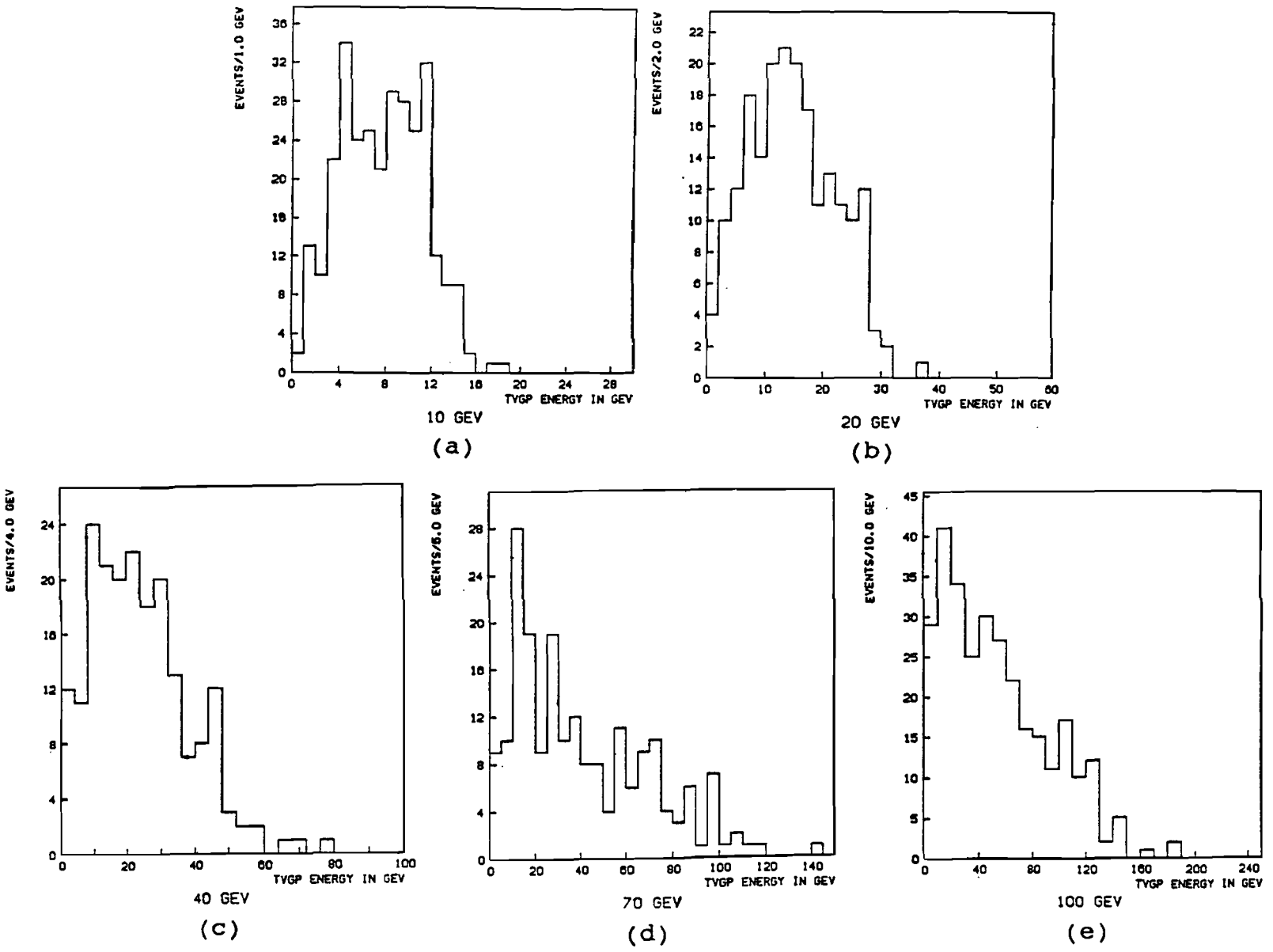
EVENTS/1.0 GEV
TVGP ENERGY IN GEV
10 GEV
(a)
EVENTS/2.0 GEV
TVGP ENERGY IN GEV
20 GEV
(b)
EVENTS/4.0 GEV
TVGP ENERGY IN GEV
40 GEV
(c)
EVENTS/6.0 GEV
TVGP ENERGY IN GEV
70 GEV
(d)
EVENTS/10.0 GEV
TVGP ENERGY IN GEV
100 GEV
(e)

Figure 41.

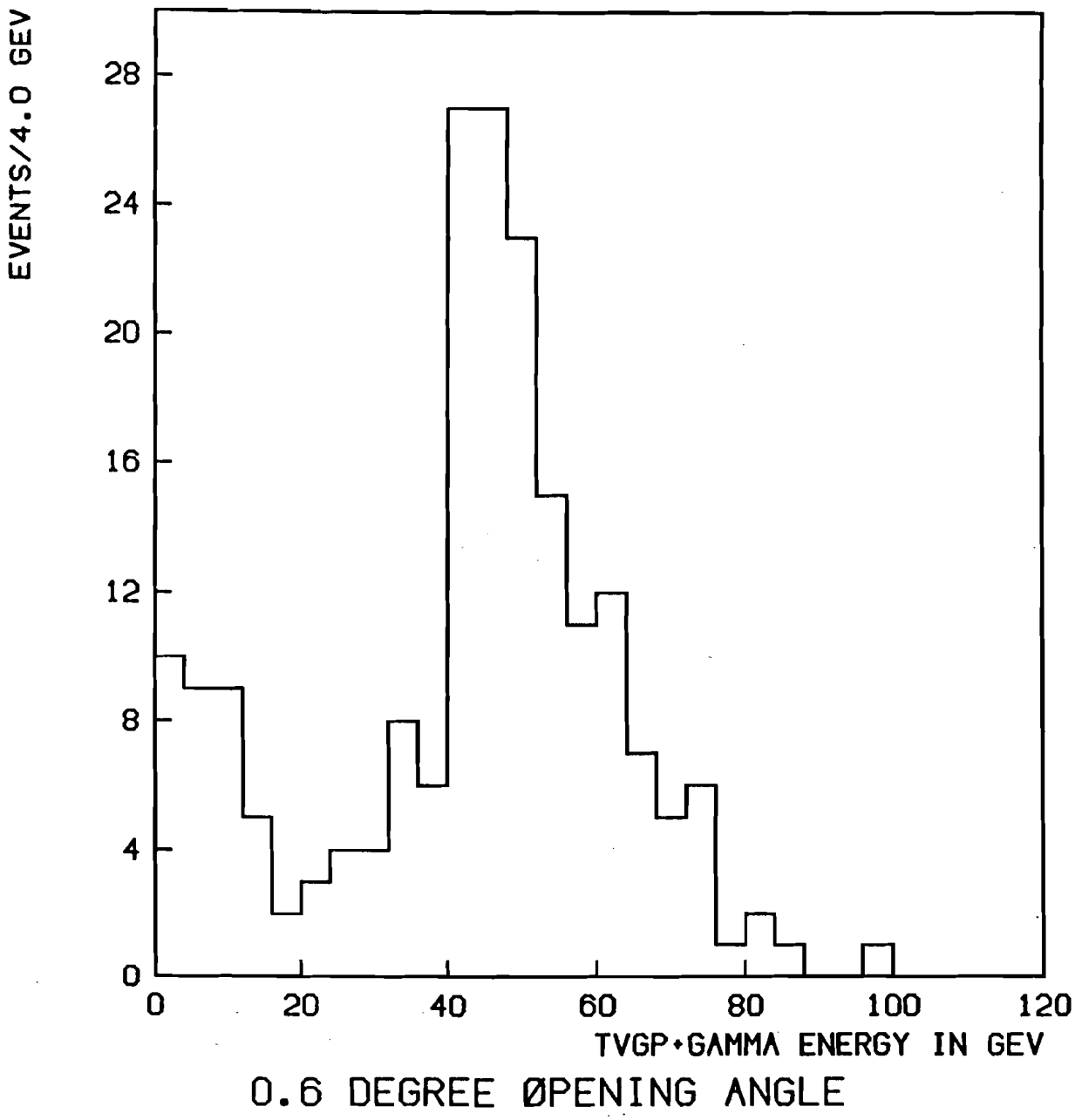
EVENTS/4.0 GEV
28
24
20
16
12
8
4
0
0
20
40
60
80
100
120
TVGP+GAMMA ENERGY IN GEV
0.6 DEGREE ØPENING ANGLE

Figure 42.

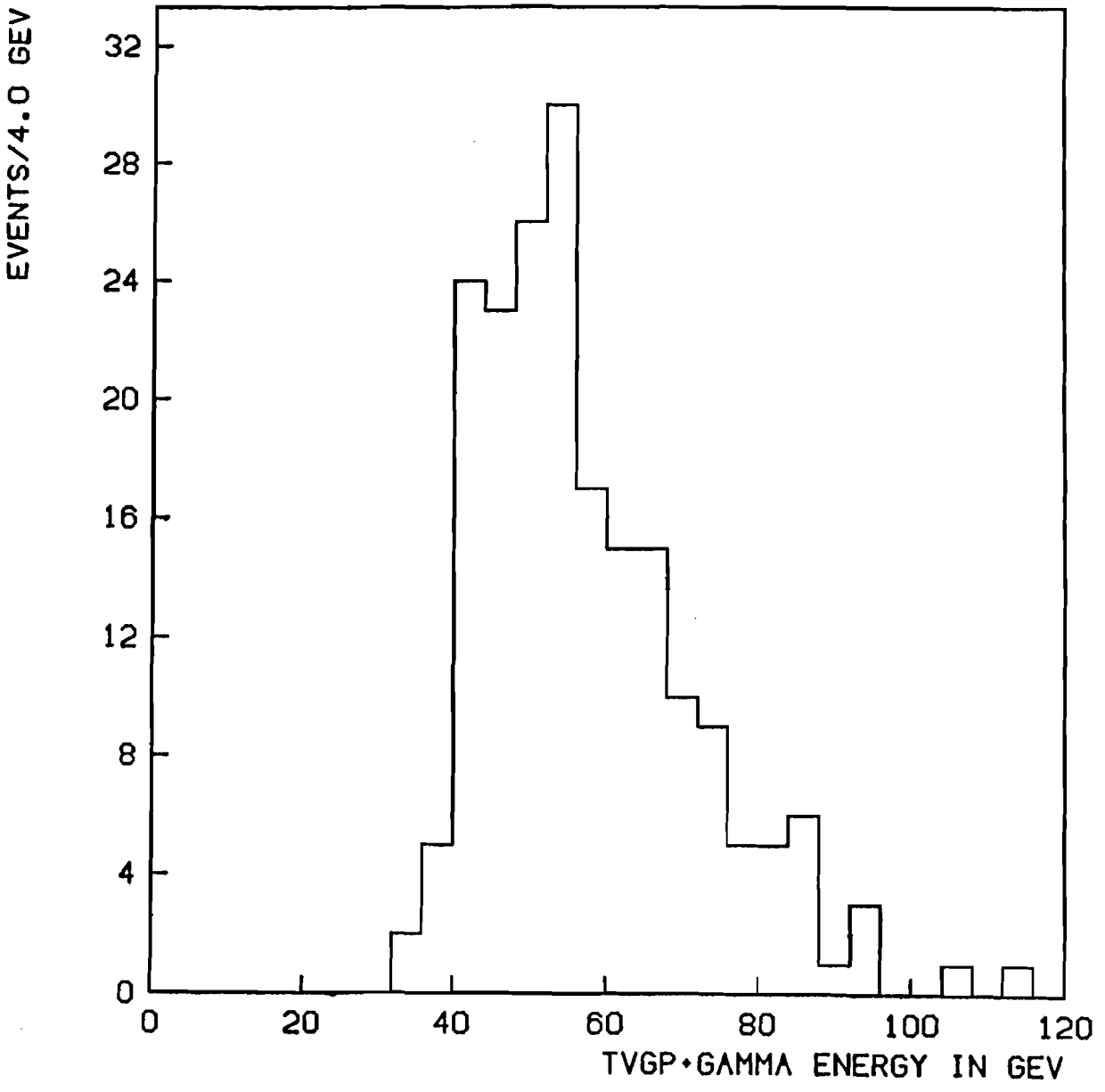

2.4 DEGREE ØPENING ANGLE

Figure 43.

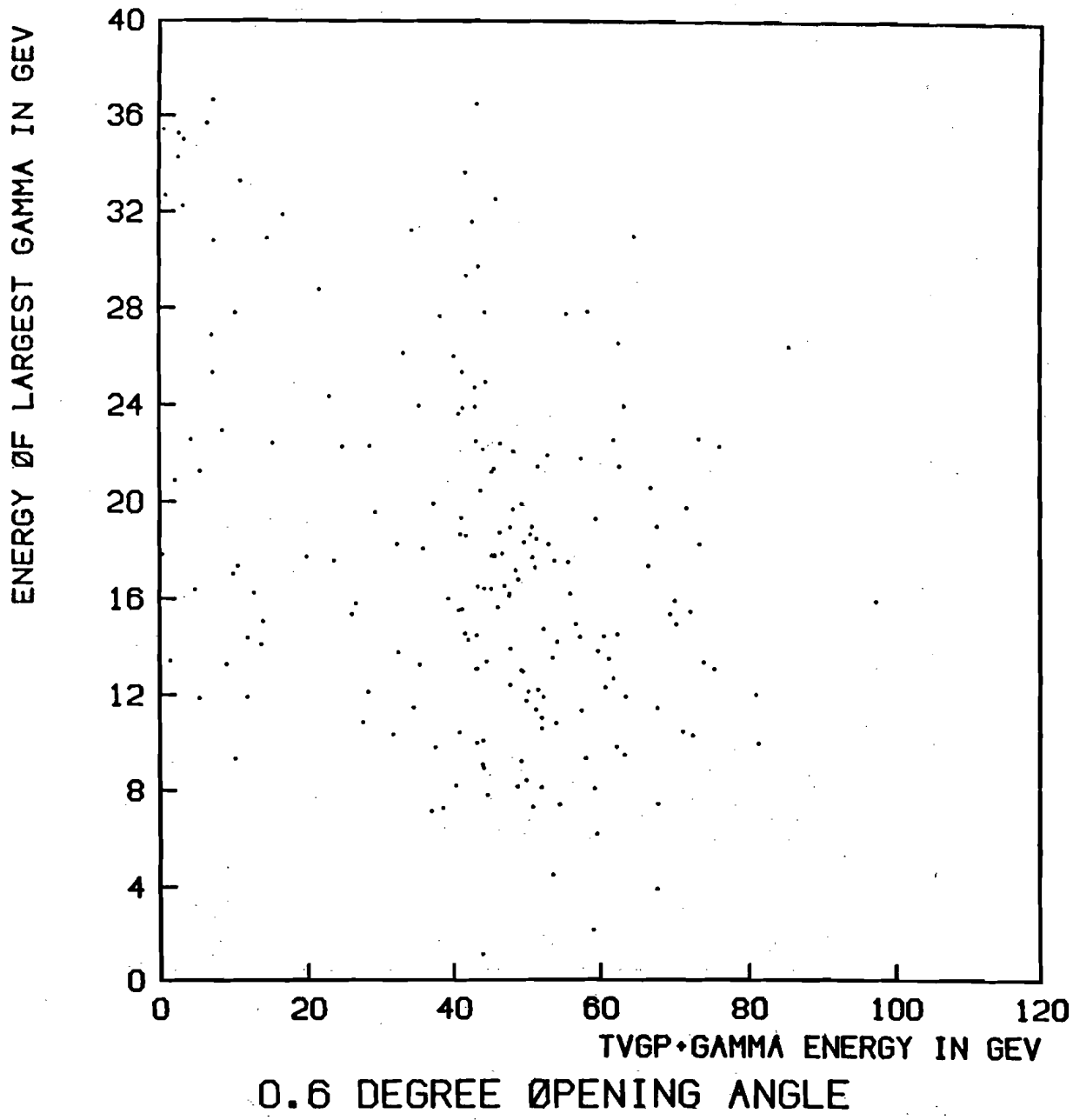
ENERGY ØF LARGEST GAMMA IN GEV
40
36
32
28
24
20
16
12
8
4
0
0
20
40
60
80
100
120
TVGP+GAMMA ENERGY IN GEV
0.6 DEGREE ØPENING ANGLE

Figure 44.

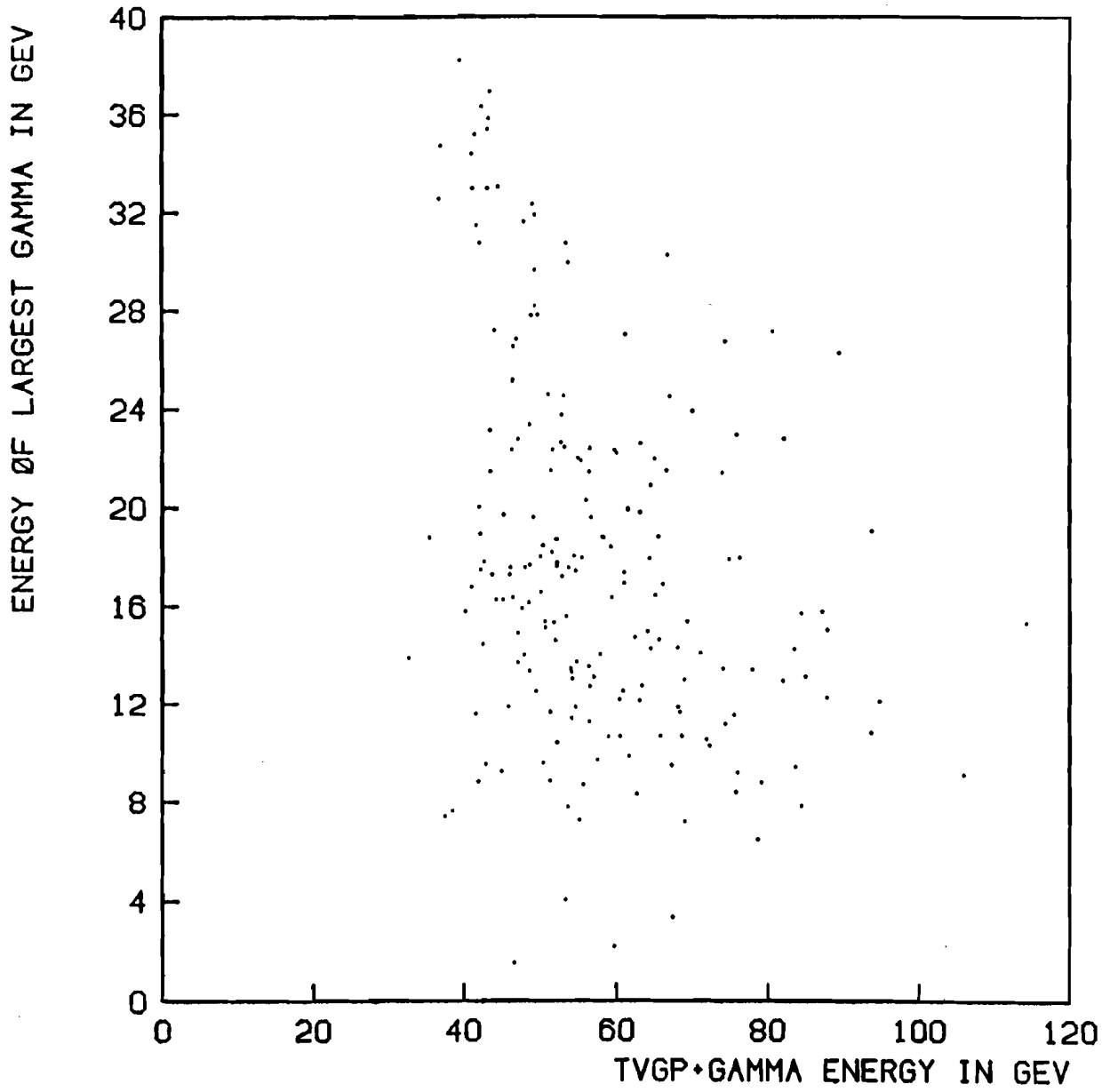

2.4 DEGREE ØPENING ANGLE

Figure 45.

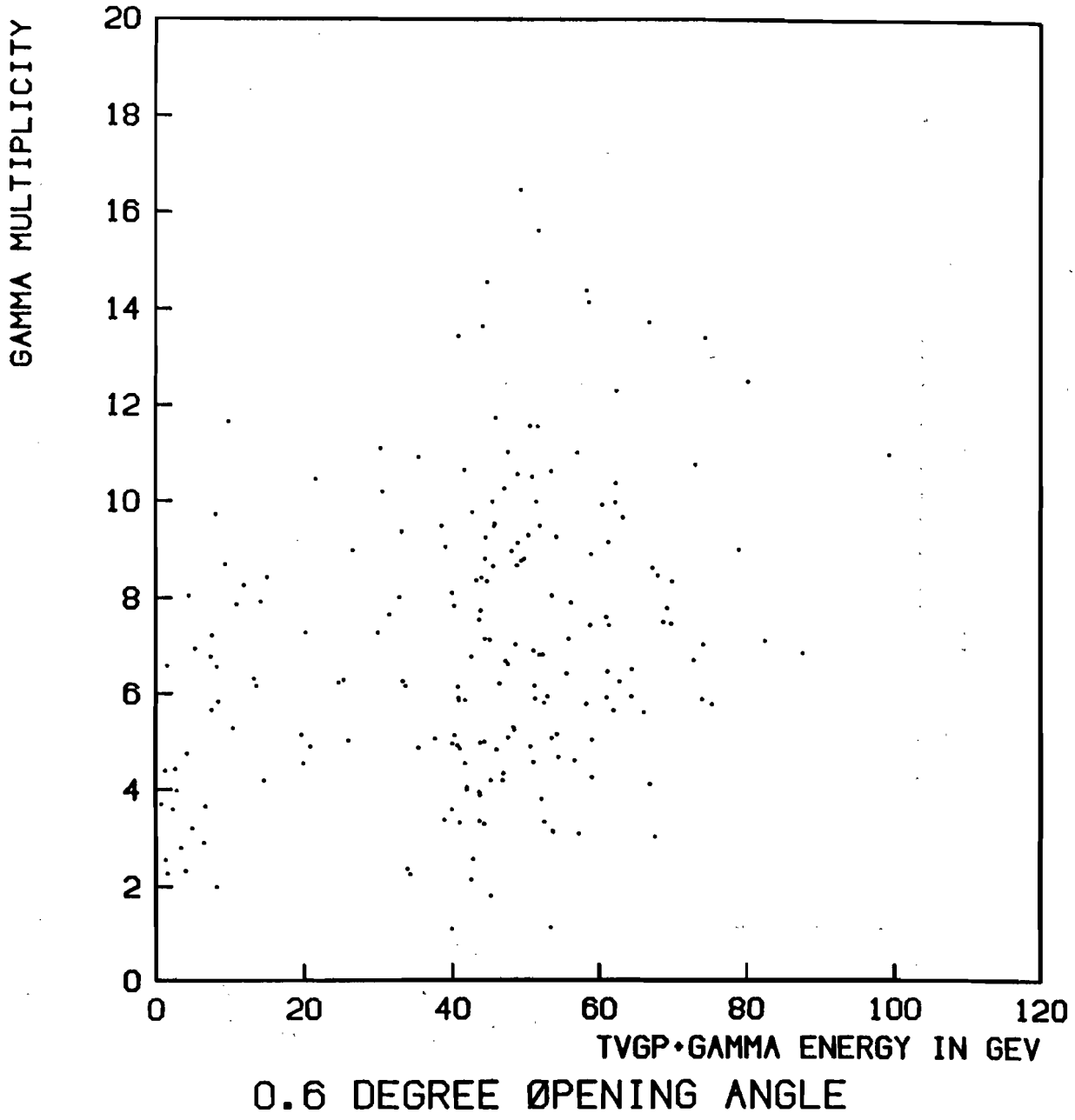
GAMMA MULTIPLICITY
20
18
16
14
12
10
8
6
4
2
0
0
20
40
60
80
100
120
TVGP+GAMMA ENERGY IN GEV
0.6 DEGREE ØPENING ANGLE

Figure 46.

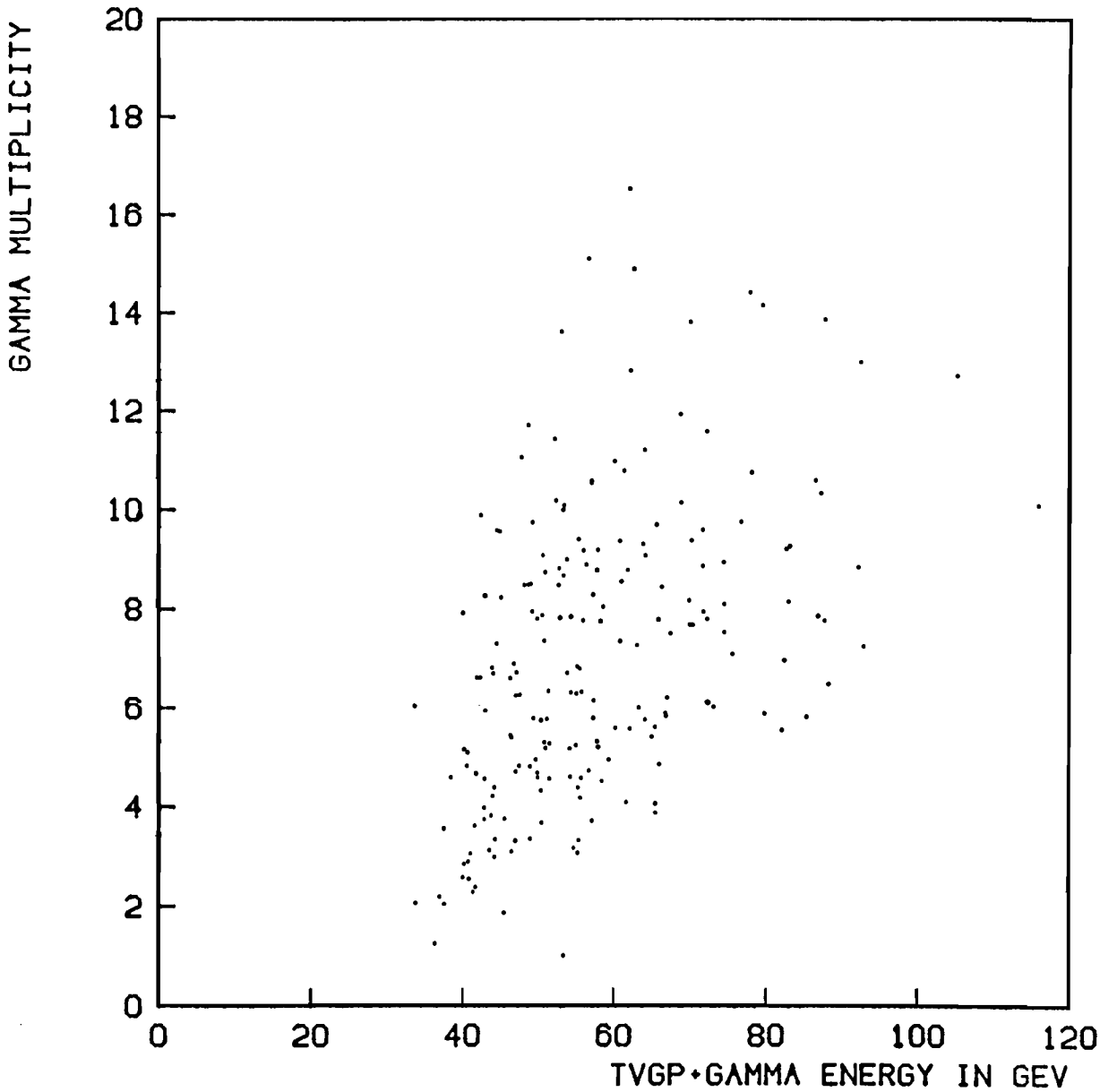

2.4 DEGREE ØPENING ANGLE

Figure 47.

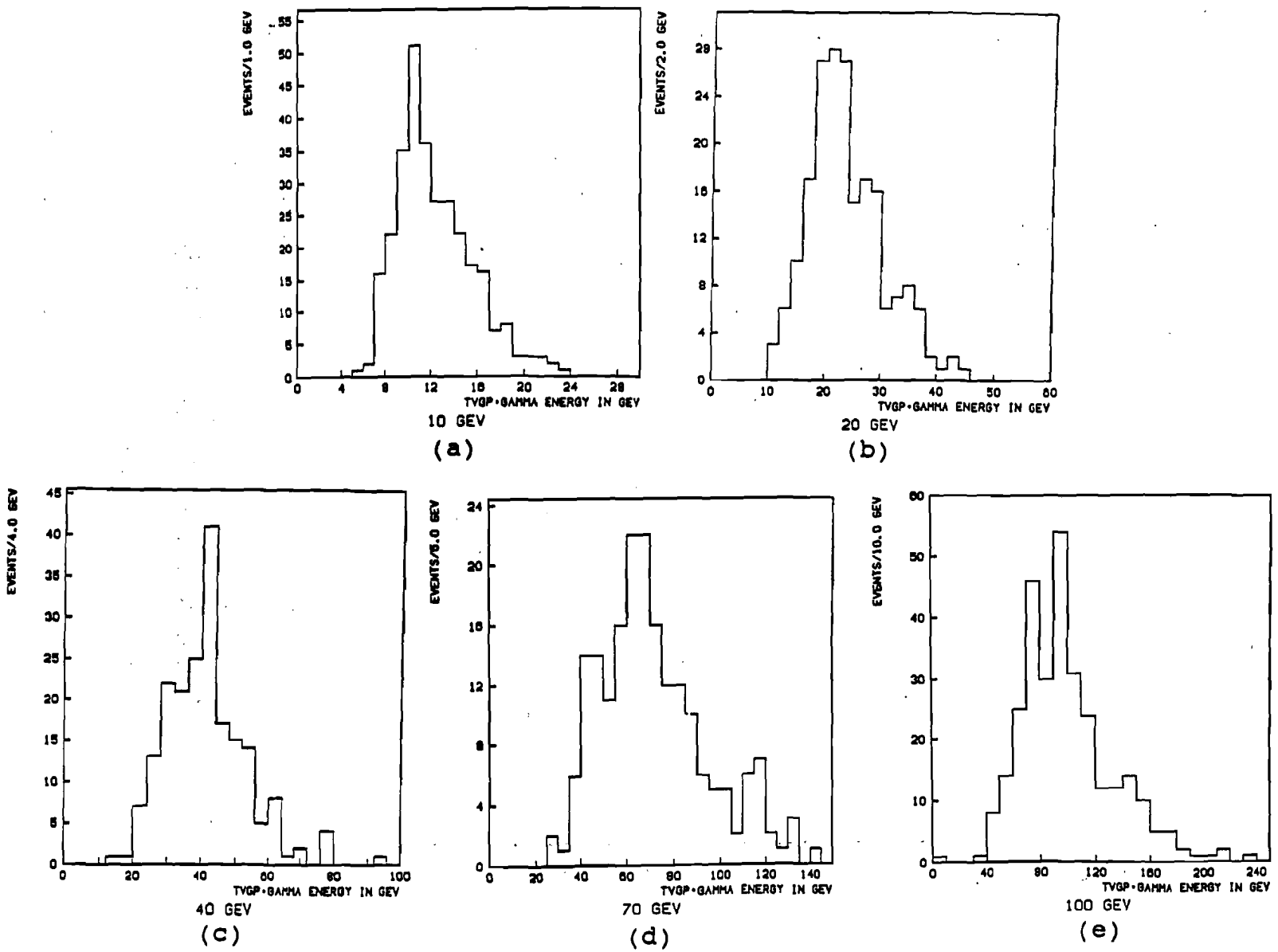
EVENTS/1.0 GEV
TVGP+GAMMA ENERGY IN GEV
10 GEV
(a)
EVENTS/2.0 GEV
TVGP+GAMMA ENERGY IN GEV
20 GEV
(b)
EVENTS/4.0 GEV
TVGP+GAMMA ENERGY IN GEV
40 GEV
(c)
EVENTS/6.0 GEV
TVGP+GAMMA ENERGY IN GEV
70 GEV
(d)
EVENTS/10.0 GEV
TVGP+GAMMA ENERGY IN GEV
100 GEV
(e)

Figure 48.

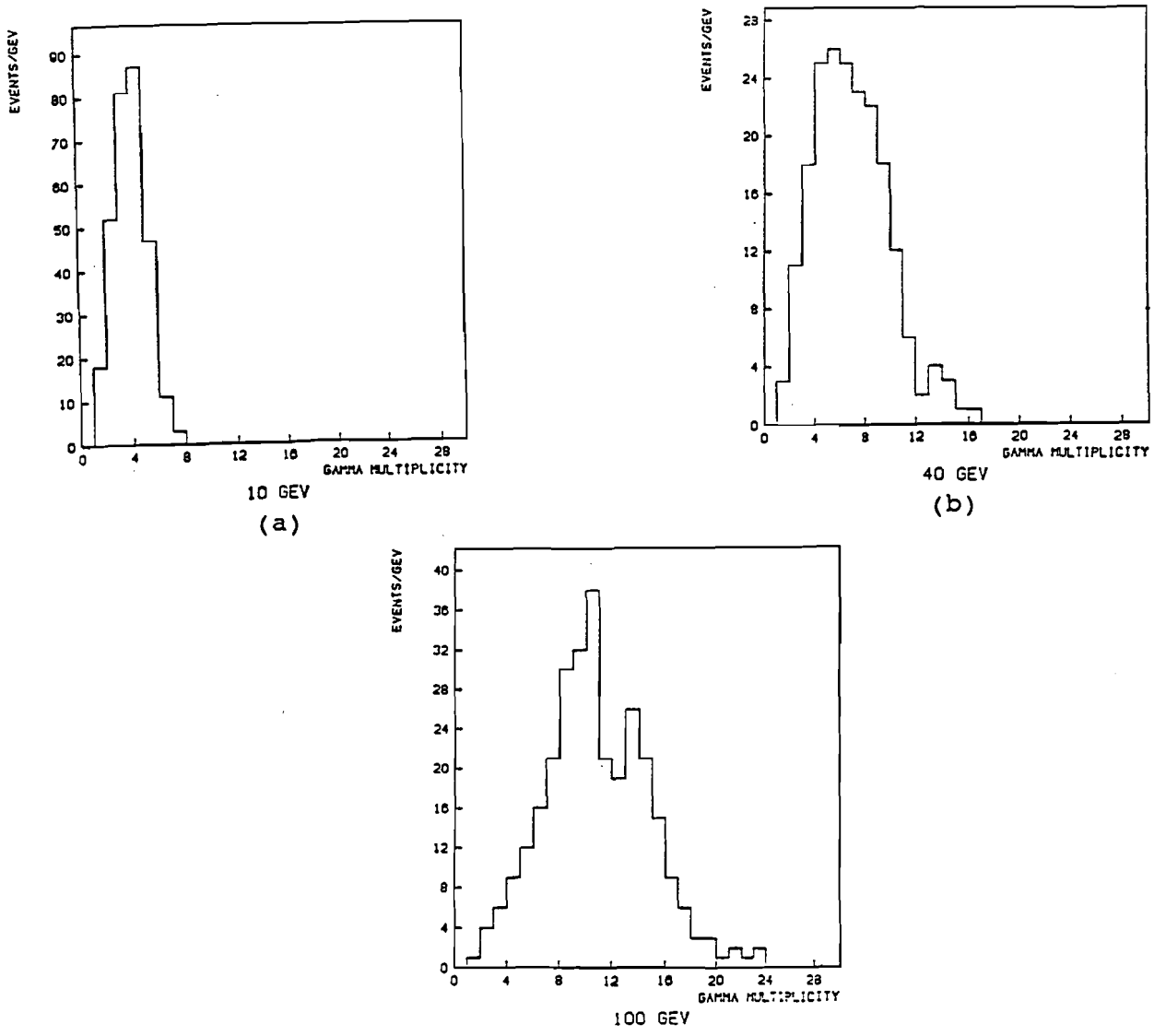
EVENTS/GEV
GAMMA MULTIPLICITY
10 GEV
(a)
EVENTS/GEV
GAMMA MULTIPLICITY
40 GEV
(b)
EVENTS/GEV
GAMMA MULTIPLICITY
100 GEV
(c)

Figure 49.

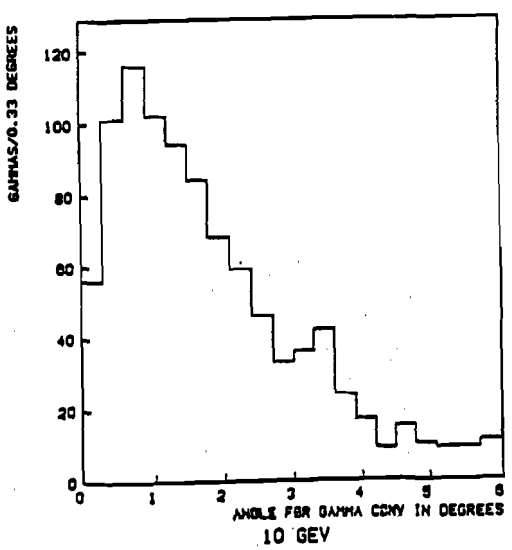

10 GEV

(a)

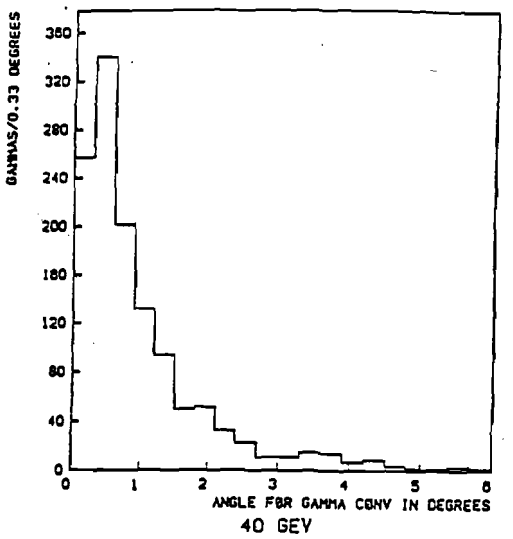

40 GEV

(b)

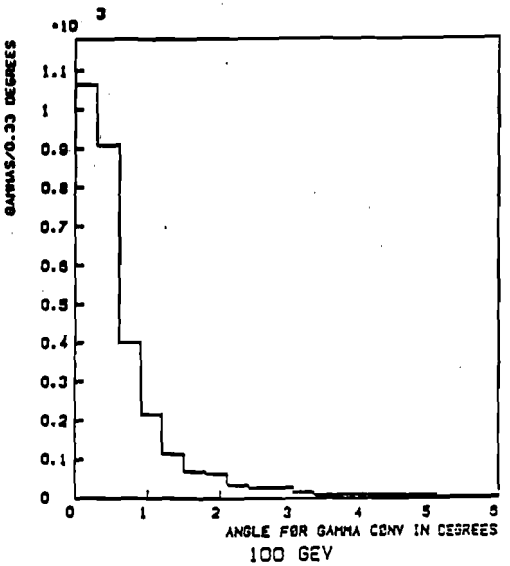

100 GEV

(c)

Figure 50.

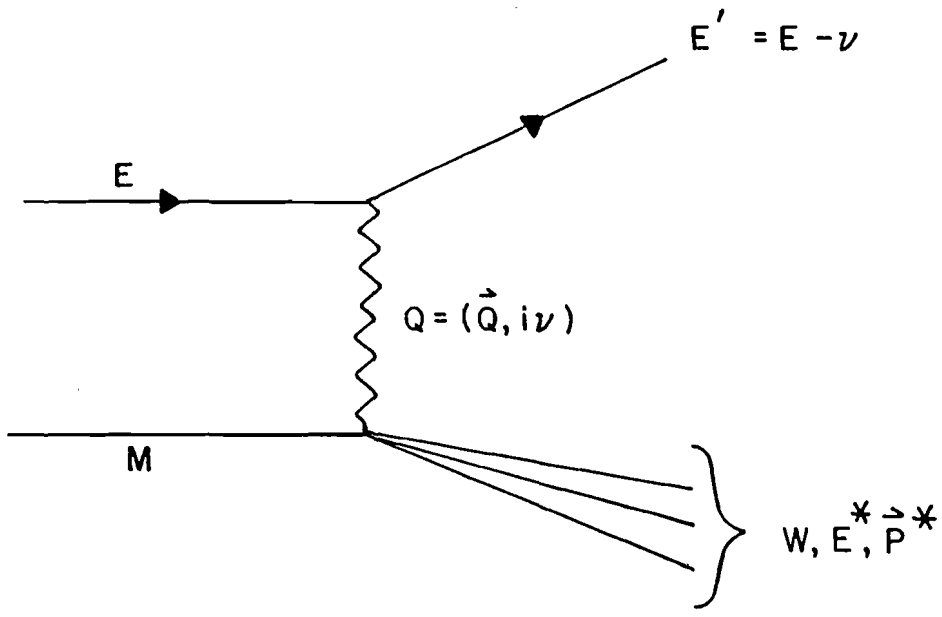

Figure 51.